PROTON AND ION CONDUCTIVITY IN MICROPOROUS MATERIALS

Thesis by

John Charles McKeen

In Partial Fulfillment of the Requirements

For the Degree of

Doctor of Philosophy

California Institute of Technology

Pasadena, CA

2009

(Defended May 13, 2009)

Acknowledgements

There are certainly many people who have been influential in my development as a scientist and engineer and to whom I owe a great deal of thanks. Foremost, I need to thank my parents for all that they have done for me. They have encouraged my many interests, scientific or otherwise, and have instilled in me a great sense of curiosity, a passion for understanding, and a desire to apply those traits to solve meaningful problems. They have taught me the importance of ethics and citizenship, to ask lots of questions, and to never give up. On a more specific note, I am thankfull to them for providing me with a “hands on” environment full of tool, lathes, welders, and the freedom to play. The experience gained from building and fixing things has proven extremely useful in many aspects of my academic endeavors and life in general. They have been steadfast in their commitment as parents, and I could not imagine a happier or more interesting upbringing.

My brother, Michael McKeen, has also shaped my development. From questioning the idea of entropy to the existence of global warming, he has been challenging me to justify and explain my scientific (and nonscientific) beliefs for many years. He is a great friend, and we have had many enlightening discussions. Watching his development as a lawyer has also been encouraging, and I can only hope that people see in me as much maturation as a scientist as I have seen in him.

All of my grandparents have been encouraging and supportive of my pursuits, but Grandpa Louie Nelson deserves a special acknowledgement, as his

desire for understanding is almost childlike. He has taught me many mechanical skills, provided hours of great discussion, and been an example for never being afraid to try.

Leslie Gehlsen, my high school chemistry and AP chemistry teacher and Science Olympiad coach, while crazy, laid the groundwork for my interest in chemistry and chemical engineering. She provided and encouraged opportunities and freedoms to goof off and try chemistry, and I am forever grateful.

Many professors at the University of Minnesota taught me a great deal, and while I can not name them all, Frank Bates, Alon McCormick, David Morse, Ed Cussler, Satish Kumar, Douglas Ernie, Bethany Stadler, Marvin Marshak, and Noland Waylan have encouraged me and strengthened my love for chemical engineering, electrical engineering, and chemistry, and were influential in my decision to pursue graduate studies.

I am forever indebted to C. Daniel Frisbie, my undergraduate advisor and electrical engineering masters coadvisor at the University of Minnesota, for all of his encouragement and direction. He and the graduate students in his lab (Reid Chesterfield, Paul Pesavento, Chris Newman, Jeff Merlo, and Jeremy Beebe) were the first to introduce me to academic research, and I am grateful for their patience, help, and continued friendship. I am also grateful to P. Paul Ruden, my other EE masters coadvisor, for his encouragement and direction.

Many members of the Caltech community have greatly contributed to my experience here. Thanks to Martha Hepworth, Kathy Bubash, Laura King, and Suresh Guptha in chemical engineering, Mike Roy and Steve Olson in the

chemistry machine shop and Rick Gerhart in the glass shop for all of their hard work in helping to build multiple iterations of the equipment used to gather the data in this thesis, and Sonjong Hwang in the solid NMR facility for his help and expertise.

I would like to thank the members of my Doctoral committee who have provided insight and feedback through my tenure at Caltech, but also much more than that. Rachid Yazami for providing the opportunity to spend time working at CNRS in France; Kostas Giapis for use of, and help with, equipment; and Yushan Yan for use of equipment and enlightening and encouraging discussion.

I am extremely grateful to The Fannie and John Hertz Foundation and the National Science Foundation for paying my salary and supporting my graduate studies. And while the money was nice, the Hertz Foundation has provided so many opportunities to meet and converse with other fellows, hear about fascinating research, and “network”, and I am equally indebted to them for those occasions and future collaborations that are sure to arise.

I, further, want to thank the members of the Davis lab for unselfishly helping whenever I asked, for many useful discussions, and for commiserating through challenges. I particularly want to express how privileged I feel to have had the opportunity to get to know and work with Brendan Mack, Chris Alabi, Nicholas Brunelli, and Jason Gamba. They have always been willing to lend a hand, tell me about what they are doing, and provide valuable insight into my own work. Their continued friendship is truly a pleasure.

Finally, none of this work would have been possible without my advisor Mark E. Davis. When I joined the lab, he agreed to let me start a new project, and for that I am forever grateful. He was encouraging as I learned and struggled and patient when I was frustrated. Some of the ideas I pitched to him worked, and many of them failed, sometimes to the tune of more money than I would like to admit. But Mark was always willing to let me try and provided me with, what has to be, the best financial support possible, not to mention many interesting discussions. I am also thankful for his willingness to share stories about past projects, successes, and failures from his many years of experience. I believe that the knowledge gained from them will prove invaluable throughout my career. Mark, thank you.

Abstract

Two separate but related investigations on proton and ion conductivity in microporous materials are presented. In the first study, the effect of hydroxyl group density on the proton conductivity in a family of sulfonic-acid functionalized microporous materials with the *BEA framework topology is investigated. Pure silica, aryl sulfonic acid-functionalized microporous materials are synthesized with high concentration of hydroxyl groups from tetraethylammonium hydroxide and aluminum-containing gels and by post synthetic modification of zinc containing CIT-6, and they exhibit proton conductivities of ~$5*10^{-3}$ S/cm. Pure-silica materials with nearly defect free structures (low hydroxyl group density) are synthesized from tetraethylammonium fluoride containing gels and by post synthetic modification of CIT-6, and exhibit proton conductivities an order of magnitude lower, ~5×10^{-4} S/cm, than the samples with a high –OH density. Propyl sulfonic acid, ethyl phosphoric acid, and carboxylic acid containing pure-silica zeolite beta, MCM-41, and MCM-48 are also prepared and investigated for use as solid proton conductors. Strong acids are necessary for fast proton transport in hydrated systems. The proton conductivities of the functionalized solids decrease accordingly with the strength of the organic acids in solutions, and little difference is observed between microporous and mesoporous solids when functionalized to the same level.

In the second study, the ion conducting properties of the microporous, zincosilicate VPI-9 (Si/Zn = 4.0) containing the alkali cations Li^+, Na^+, K^+, Rb^+, and Cs^+, and the alkaline earth cations Mg^{2+}, Ca^{2+}, and Sr^{2+} are studied using

impedance spectroscopy. Monovalent cation exchanged samples Li- and Na-VPI-9 lose X-ray crystallinity upon vacuum dehydration at 450 °C, while K-, Rb-, and Cs-VPI-9 remain crystalline and exhibit conductivities of 1.7×10^{-4}, 3.5×10^{-4}, and 4.9×10^{4} S/cm, respectively, at 450 °C in vacuum. While K-VPI-9 is less conductive than K-X, Rb- and Cs-VPI-9 are more conductive than corresponding zeolite X samples. Divalent cation exchanged sample Mg-VPI-9 also loses X-ray crystallinity, while Ca-, and Sr-VPI-9 remain crystalline and exhibit conductivities of 2.3×10^{-6} S/cm and 7.7×10^{7} S/cm, respectively, at 450 °C, greatly exceeding the conductivity of correspondingly divalent exchanged zeolite X materials. Dense, crystalline zincosilicate samples with the compositions $K_2ZnSi_xO_{2(x+1)}$ (x = 2 - 5), $Rb_2ZnSi_5O_{12}$, and $Cs_2ZnSi_5O_{12}$ are also prepared and exhibit much lower conductivities than their microporous counterparts.

Table of Contents

List of Figures

1. Introduction

1.1. Motivation

In 2005 global energy consumption was on the order of 16 TW, and this value is predicted to increase with the growing demands of industrializing nations. Nearly 12 TW of this energy was extracted from the combustion of hydrocarbon fuels, 1 TW from each nuclear and hydroelectric, and a very small fraction from renewables such as geothermal, solar, and wind. While increased atmospheric greenhouse gas levels, particularly CO_2 emitted from hydrocarbon combustion, may negatively impact earth's climate, many reasons exist to investigate renewable energy production and clean-energy conversion devices. Worthy directions of investigation include solar production of electricity and solar production of transportable fuels such as hydrogen gas by direct (chemical splitting of water) or indirect (electrolysis of water using solar-generated electricity) methods, and clean-energy conversion devices include solar collectors, direct methanol fuel cells (DMFCs), hydrogen fuel cells (also called proton exchange membrane fuel cells, PEMFCs), and others.

While the combustion of hydrogen produces no greenhouse gases, storage of hydrogen at any appreciable density is a research challenge in itself, and the more mature field of solar production of electricity is receiving industrial attention and government sponsored installation. If solar proves to be the route of choice, advancement in energy storage is needed. If society is to completely move to a solar fed system, energy densities achieved with even the most

advanced lithium chemistries currently available must be improved for large-scale collection and storage of solar generated electricity to provide for energy demand during sunless times.

The research efforts highlighted in this thesis were performed to address some of the aforementioned goals. Beyond these lofty goals, however, are underlying interests in understanding proton and ion motion in microporous materials. This broad goal was whittled down into two main thrusts. First, protonically conducting zeolites were investigated with hope of improving the operating performance of DMFCs and PEMFCs by addressing some of the engineering challenges associated with the separator membrane between the anode and cathode, particularly maintaining high proton conductivity at elevated temperatures that normally cause loss of hydration and decreased proton conductivity, and reducing methanol crossover. This study focused on zeolites with the *BEA framework topology and included pure silica materials, aluminum containing materials, and materials functionalized with organic acids. Secondly, alkali- and alkaline-earth metal, cation-exchanged, microporous zincosilicates were investigated as potential ion conductors with hope of observing fast transport, particularly for the generally slow moving divalent ions, opening a door to new, divalent cation based battery chemistries. (As will be discussed later, framework zinc imparts two negative charges to the surrounding oxygen atoms, potentially facilitating facile transport of divalent ions). While many engineering considerations exist in optimizing a battery, one Holy Grail (that would itself require significant engineering development for use in commercial batteries) is a

non-flammable, solid electrolyte with high ionic conductivity, and the search for such a material provided further motivation for studying the ion conducting properties of (non-flammable) VPI-9.

1.2. A Brief Introduction to Fuel Cells and Batteries

1.2.1. Fuel Cells Overview

Fuel cells embody the hope of ultra high energy density devices, with theoretical energy densities, in excess of 30,000 Wh/kg when the fuel is hydrogen gas, and in excess of 6000 Wh/kg when the fuel is pure methanol. Much like traditional batteries, hydrogen fuel cells, also known as proton exchange membrane fuel cells (PEMFCs), and direct methanol fuel cells (DMFCs) are composed of an anode, a cathode, and a proton conducting membrane. The anode and cathode electrodes are complex, multicomponent structures that include a current collector, catalysts necessary for the oxidation of fuel at the anode and reduction of dioxygen at the cathode, and two percolated networks, one for conducting protons and the other for conducting electrons to or from the catalyst active sites to or from the membrane or current collector, respectively. Additional design considerations include efficient gas diffusion, water management, and start-up and shutdown. A schematic of a PEMFC is shown in Figure 1.1, including the anode, cathode, proton conducting membrane, catalyst layers, and gas diffusion structures.

Potential fuel cell markets include transportation, consumer electronics, portable power supplies, and backup power systems. Encouraging aspects of

fuel cells include their environmental friendliness, long lifetimes, and high energy conversion efficiency, while drawbacks include component cost, catalyst poisoning, hydrogen storage in the case of PEMFCs, water management (cathode flooding), and startup and shutdown.

Zeolites could potentially address some of these challenges, improving device efficiency. Two of the major challenges in operating fuel cells include methanol crossover in the case of DMFCs and decreased proton conductivity caused by separator membrane dehydration when operated at elevated temperatures (particularly in PEMFCs where catalysts are sensitive to CO impurities in the H_2 feed stream when operated at low temperatures). Because of their small pores, zeolites could reject methanol at the anode, reducing the rate of chemical diffusion to the cathode. Further, they are known to hold onto water at elevated temperatures, potentially addressing the problem of dehydration at elevated operating temperatures. Further discussion of proton conduction in zeolites and zeolites in fuel cells is presented later.

1.2.2. Nafion for Fuel Cells

One critical component of a fuel cell is the protonically conducting but electronically insulating membrane that separates the anode from the cathode. While many research efforts have been devoted to inventing and investigating new materials for this application, Nafion, a product of DuPont, remains the industrial standard. Nafion, shown in Figure 1.2, is a perfluorocarbon polymer with fluorinated sulfonic acid containing side chains. When hydrated, the hydrophilic sulfonic acid containing side chains are believed to form water

containing domains ~5 nm in diameter. These large domains are believed to be spaced ~4 nm apart and interconnected by smaller channels of ~1 nm diameter.[1-3]

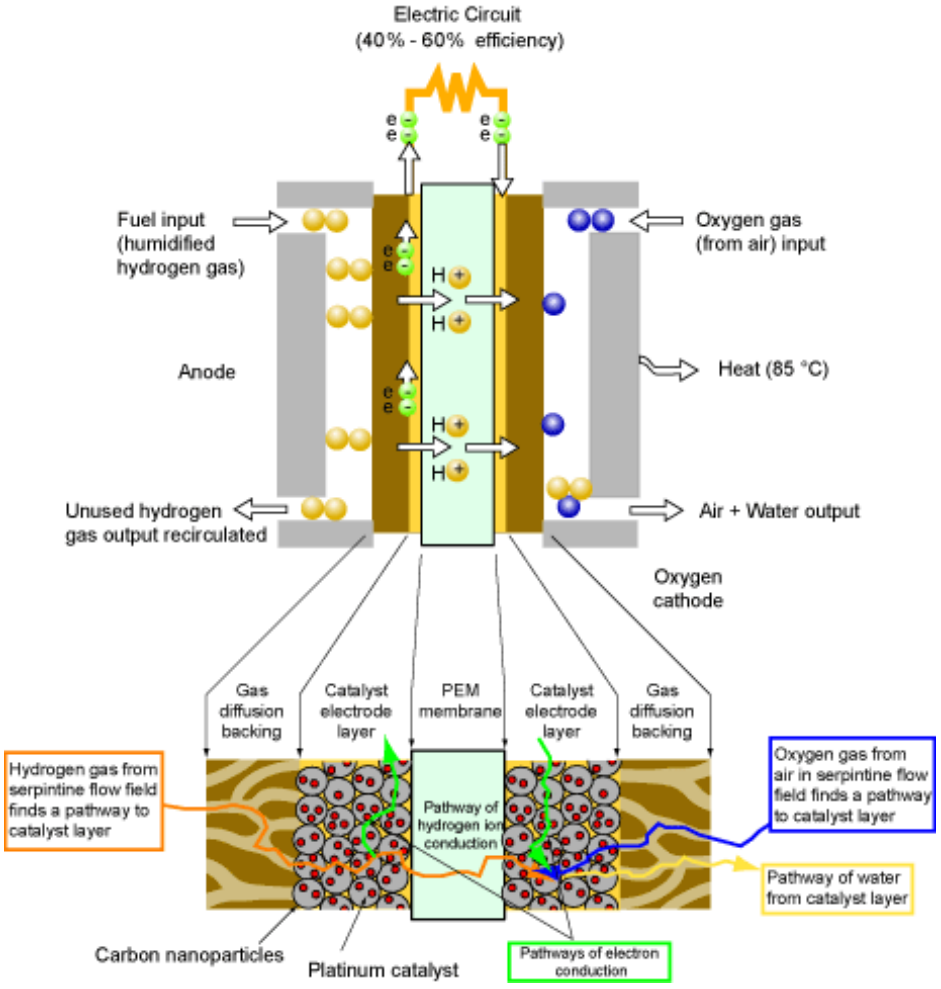

Figure 1.1. Schematic of hydrogen fuel cell.

(http://physics.nist.gov/MajResFac/NIF/Images/FuelCellBasic.gif)

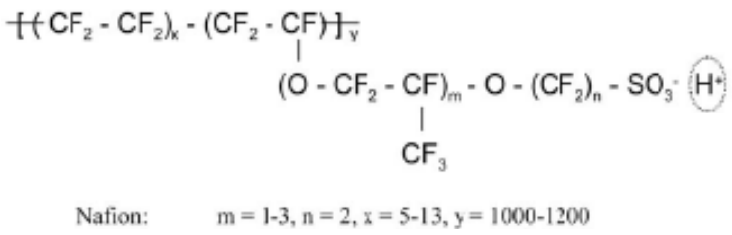

Figure 1.2. Chemical structure of Nafion showing the fluorocarbon backbone and fluorinated, sulfonic acid side chain.

Proton conduction in hydrated Nafion is believed to occur in the hydrophilic domains by the Grotthuss mechanism[4] in which protonic defects, extra protons donated by the sulfonic acid groups, move by hydrogen bond rearrangement. In the Grotthuss mechanism, a supporting, hydrogen-bonded solvent network is mandatory for proton transport, and in the case of Nafion, this network is formed by water molecules. Chemical diffusion of proton vehicles such as hydronium ions also occurs, and is referred to as the vehicular mechanism, but this process transports protons at a much slower rate than the Grotthuss mechanism. Recent computational reports nicely highlight the orders of magnitude difference in proton transport rates between Grotthuss transport and vehicular transport in hydrated Nafion.[5] Reference 5 also address hopping of a proton from a sulfonic acid group to a neighboring sulfonic acid group, and computational results indicated that this mechanism of proton transport is also slow when compared to Grotthuss transport. As temperature is increased and Nafion begins to dehydrate, the hydrogen bonded water network loses hydrogen bond percolation, and transport occurs by the much slower vehicular mechanism. It is, therefore, of paramount importance to maintain a high level of hydration in Nafion membranes to maintain high proton conductivity.

1.2.3. Batteries

To present an appropriate review of all battery literature would require thousands of pages and be appropriately titled the *Handbook of Batteries*.[6] Rather, a brief introduction to modern lithium batteries will be presented to

familiarize the reader with the components and operation of such an electrochemical energy storage device.

A schematic of a secondary (rechargeable) lithium battery is shown in Figure 1.3. The anode consists of graphitic carbon particles with lithium atoms intercalated between the graphitic layers. The cathode consists of lithium cobalt oxide particles coated with a small amount of carbon to impart electrical conductivity to the composite structure and facilitate electron transport from the cathode current collector to the electrochemically active lithium cobalt oxide particles. Both the composite anode structure and composite cathode structure are macroporous and the pores are filled with the supporting electrolyte to facilitate fast lithium ion transport to and away from the electrochemically active particles. An insulating, porous separator membrane electrically isolates the anode from the cathode, but allows lithium ions to pass through the electrolyte filled pores. A typical electrolyte is prepared by dissolving a lithium containing salt, such as $LiPF_6$, in organic solvents, such as ethylene carbonate and dimethyl carbonate. Typical conductivities are on the order of 10^{-2} S/cm at room temperature. When discharged, lithium atoms intercalated into the graphitic carbon are oxidized and deintercalate into the surrounding electrolyte. The electron is conducted to the anode current collector and flows through the external load connected to the battery, arriving at the cathode, reducing cobalt(IV) to cobalt(III). A lithium ion concurrently travels through the supporting electrolyte, across the separator membrane and arrives at the external surface of a Li_xCoO_2 particle, where it must diffuse inward to the location of the cobalt that is

being reduced by the electron. To be electrochemically active, each Li_xCoO_2 particle must, therefore, be part of a percolated, electronically conducting network and a percolated, ionically conducting network, and loss of percolation of either of these networks causes loss of capacity with repeated charge/discharge.

Because of the high reactivity of lithium with moisture and the flammability of the organic solvents used in the supporting electrolyte, consumer lithium batteries have been known to thermally runaway and burn due, primarily, to poor quality control during manufacturing. While safety features have been engineered into modern batteries, it is desirable to remove flammable components from batteries. This is no small task, however, given the complex composite structure of the cathode and anode, and is a topic of research.

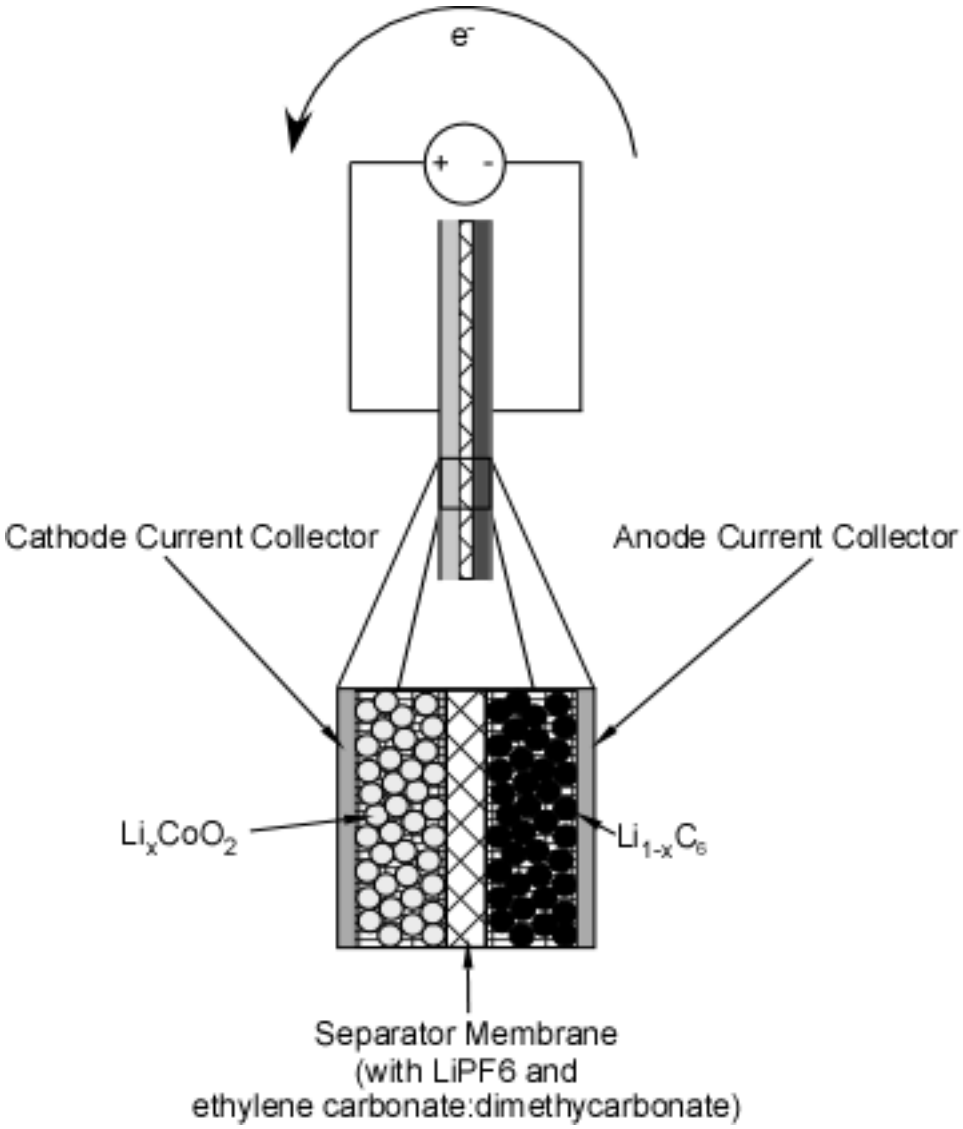

Figure 1.3. Schematic of secondary (rechargeable) lithium battery. The anode is composed of particles of carbon with lithium intercalated between the graphitic layers. The cathode is composed of particles of lithium cobalt oxide. A typical electrolyte is $LiPF_6$ dissolved in a mixture of ethylene carbonate and dimethyl carbonate.

1.3. Zeolites and Zeolite-like Materials

Section 1.3 is meant to serve as a brief introduction to zeolites and zeolite-like materials and to set the stage for the remainder of this thesis.

1.3.1. What are Zeolites and Zeolite-like Materials?

Zeolites and zeolite-like materials are microporous, crystalline materials composed, primarily, of $[SiO_4]^{2-}$ tetrahedra connected to form a framework with 1-, 2-, or 3-dimensional network of pores ranging in diameter from 2 to 10 Å. Because of their small and unique pore sizes, these often naturally occurring materials possess the ability to selectively adsorb and separate molecules based on size and hydrophobicity and are often described using the term “molecular sieve”. Additionally, some of the $[SiO_4]^{2-}$ tetrahedral can be “replaced” with $[AlO_4]^{3-}$ tetrahedra imparting a single anionic charge to the otherwise neutral silicon dioxide framework. As the overall structure must be charge neutral, the anionic framework charge must be balanced by a cation, proton, ammonium, or positively charged organic cation (such as tetraethylammonium). Various aluminosilicate zeolites are employed as acid catalysts in the production of commodity chemicals such as cumene, ethylene oxide, and para-zylene, and faujasite (ultrastable zeolite Y, for example) is used in modern fluidized catalytic crackers. Other applications arising from their microporous structure and charged framework include ion exchange materials for softening water, selective gas adsorption and separation, removal of radioactive waste, and supports for nanoparticle catalysts.

1.3.2. Synthesis Considerations

The topic of zeolite and zeolite-like materials synthesis has received intense academic and industrial interest for decades and the search for new materials and the ability to synthetically tune the properties of known materials continue to receive considerable attention. The synthesis of zeolitic materials is not as straightforward as combining starting materials in the correct proportions and heating to elevated temperatures to produce a thermodynamically favored phase, as these porous materials are kinetically trapped phases, with quartz being the thermodynamically favored dense phase in the case of purely silacious materials. Hydrothermal synthesis methods, have therefore, been developed to synthesize zeolitic materials, often under autogenous pressures at relatively low temperatures (room temperature to ~200 °C).

Typically, a silica source, an alumina source, a source of alkali cations, and a source of hydroxide ions (the mineralizing agent that solubalizes silica) are combined with water in the appropriate proportions, and heated in Teflon lined, stainless steel autoclaves for some time ranging from hours to tens of days. Silica sources include tetraethylorthosilicate (TEOS), fumed silica, dried silica gels, and colloidal silicas such as Ludox, among others. Alumina sources include aluminum metal, aluminum hydroxide gels, sodium aluminate, and others. Cations and hydroxide ions are often introduced in the form of strong bases such as sodium hydroxide. In addition to these reagents, organic cations such as tetraethylammonium hydroxide, tetrapropylammonium hydroxide, and other, often complex, quaternary ammonium containing compounds are used to help

direct the formation of the desired product and are referred to as structure directing agents. Further, many other heteroatoms have been introduced into the framework of zeolite-like materials including germanium, gallium, iron, vanadium, and zinc from various precursors such as nitrates, acetates, and oxides.

A more recently discovered synthetic technique uses fluoride ions as the mineralizing agent rather than hydroxide ions. Gels prepared using the fluoride technique are generally much more viscous than traditional basic gels, and have been used to synthesize pure silica materials in the absence of both alumina and metal cations.[7,8] Fluoride syntheses often produce large crystallites (1-10 μm) with low hydroxyl defect densities. In pure silica beta from an F^- synthesis the absence of connectivity defects is reflected in the ^{29}Si MAS NMR by the presence of well resolved peaks arising from the crystallographically different silicon sites (as no aluminum exists to alter the Si peak positions).

The mechanism of crystallization of zeolites and zeolite-like materials remains a debated topic of research. Studies using the pure silica ZSM-5/silicalite-1 system suggest that hydrated tetrapropylammonium (TPA), the structure directing agent, lose their water hydration sphere and interact with inorganic silica species through van der Waals interactions.[9-13] Five nanometer building units then form and have been observed by small angle X-ray scattering in room temperature syntheses. These 5 nm particles aggregate and grow into silicalite-1 crystallites with sizes on the order of 50-100 nm, growing in size over the crystallization period, suggesting an Ostwald ripening process. Further work has also been carried out in alumina containing systems and results suggest that

nanoparticles may play a similar role in the nucleation and growth of aluminosilicates.[14]

Crystallization of a specific structure is often challenging as nucleation of kinetically trapped phases is extremely sensitive to impurities in starting materials and water, and extreme care must be taken in choice of precursor materials and water sources. Phases are also sensitive to the order of addition of starting materials, how the resulting gel is aged, choice of synthesis temperature, and whether or not the bomb is rotated during crystallization.

After synthesis, many crystallization products contain organic structure directing agents in their pores, and these bulky molecules must be removed to impart porosity to the materials. Traditionally, this is done by calcination, although extraction with various solvents is appropriate in some cases.[15,16]

1.3.3. The Zincosilicates

One family of zeolite-like materials discovered in the past decade is that of the zincosilicates. These crystalline, microporous materials are similar to traditional zeolites in that they are composed of $[SiO_4]^{2-}$ tetrehedra but rather than containing $[AlO_4]^{3-}$ tetrehedra, contain $[ZnO_4]^{4-}$ tetrehedra creating two -1 framework charges per zinc that must be charge balanced by metal cations, protons, or organic cations. The zincosilicates, who's structural properties are shown in Table 1.1, were discovered in the search for low framework density materials and include VPI-7[17], VPI-8[18-22], VPI-9[23], VPI-10, RUB-17[24], CIT-6[20,25-27], Zn-ANA[28], and Zn-SOD.[29] VPI-7, VPI-9, VPI-10, and RUB-17 do not have aluminosilicate or pure silica analogs due to the presence of three-membered

rings in the crystalline structure, arising from the presence of zinc. CIT-6, the zincosilicate analog of aluminosilicate zeolite beta, has received the most attention among the zincosilicates and has been shown to be a convenient starting material for the production of a family of materials with the *BEA topology through post-synthetic chemical modification.[25,27] Using acetic acid, zinc can selectively be extracted from the framework and washed from the pores of CIT-6 leaving either hydroxyl nests, if treated below 100 °C, or producing a hydrophobic *BEA material, if treated above 100 °C, annealing out the hydroxyl nests, presumably with a small amount of dissolved silica from other parts of the structure. Further, if treated with acetic acid in the presence of aluminum, aluminum can be inserted into the former zinc sites producing an aluminosilicate *BEA material.

Table 1.1. Structural properties of known zincosilicates.

Zincosilicate	Cation	Largest Pore	3 MR	Framework Density	Si/Zn
CIT-6	Li	12 MR	No	15.1	15-30
VPI-10	Rb and K	9 MR	Yes	15.3	3.7
VPI-9	Rb and K	8 MR	Yes	16.7	4
RUB-17	Na and K	9 MR	Yes	16.8	3.5
VPI-7	Na and K	9 MR	Yes	17.1	3.5
Zn-SOD	Na and TMA	6 MR	No	17.2	6.2-12.8
Zn-ANA	Cs	8 MR	No	18.5	
VPI-8	Li	12 MR	No	19.8	8-∞

1.3.4. Organically Functionalized Molecular Sieves (OFMSs)

While many research efforts have been devoted to the preparation and study of organically functionalized mesoporous materials, such as MCM-41, MCM-48, and SBA-15 in which organic silanes are either grafted onto surface hydroxyls or synthesized by "one-pot" techniques, synthesis of organically functionalized microporous materials was not realized until the late 1990s.[30-34] Jones and Davis first prepared sulfonic acid containing pure silica zeolite beta to study the acid catalyzed reaction of cyclohexanone with ethylene glycol to synthesize 2,2-pentamethylene-1,3-dioxolane, by adding phenethyltrimethoxy silane to a fluoride containing gel to produce pure silica beta with a internal phenethyl moieties attached to framework silicon atoms. Acidity was created by sulfonation of the para position of the phenyl group by post synthetic reaction with fuming sulfonic acid (oleum). Further reports showed the incorporation of amines[34], thiols[31], and various other organic moieties[31,33].

OFMSs are synthesized in the presence of tetraethylammonium fluoride and the resulting crystallites contain tetraethylammonium cations (TEA^+) (and fluoride anions) within their pores. Whether used for catalysis, proton conduction, or some other purpose, access to the organic groups through the interconnected pores in necessary and occluded TEA must be removed from the pores to impart porosity. Calcination, however, is not acceptable as heating would not only combust the occluded TEA^+ molecules but would also destroy the attached organic group. To overcome this problem, a new extraction technique was developed using acetic acid to extract TEA from the pores of pure silica *BEA.

Extraction of the TEA cation with acetic acid is uniquely suited to pure silica materials, or materials such as CIT-6 in which acetic acid extracts framework zinc) where TEA^+ cations do not electrostatically interact with framework charges (as is the case in aluminosilicate *BEA).

Holmberg performed the first synthesis of organically functionalized nanocrystalline zeolite beta modifying a synthesis procedure developed by Corma.[35-37] Tetraethylammonium hydroxide is used as the mineralizing agent and structure directing agent in the presence of aluminum to produce crystallites ranging in size from 10 to 250 nm and composition from SiO_2/Al_2O_3 = 13-150. In this case, acetic acid does not remove all TEA from the crystallite pores and stronger treatment is necessary.

1.4. Ion and Proton Conduction in Zeolites and Zeolite-like Materials

What follows in section 1.4 is a literature review on proton and ion conduction in these materials, and is meant to familiarize the reader with what has previously been studied, in hopes of presenting a unified view of protonic and ionic motion within microporous materials.

1.4.1. Proton Conduction in Acid Functionalized Micro- and Mesoporous Materials

Many reports exist on the synthesis of organically functionalized mesoporous materials, including acid functionalized materials for catalysis, but only a few reports exist on the proton conducting properties of acid functionalized

mesoporous materials[38-40] and even fewer on the proton conducting properties of acid functionalized microporous materials[41]. Mikhailenko *et al.* were first to investigate sulfonic acid functionalized mesoporous materials. Mercaptopropyl functionalized mesostructured silica was synthesized in a one-pot method and the thiol groups were post synthetically converted to sulfonic acids by oxidation with 33% hydrogen peroxide. Samples containing 0, 0.5, and 1.1 meq SO_3H/g material were prepared and characterized at 100% relative humidity with impedance spectroscopy by clamping powdered samples between stainless steel electrodes in a glass tube. Measurements were made as a function of temperature to extract activation energies for proton transport. At room temperature, non acid functionalized samples exhibited conductivity of ~10^{-5} S/cm while 0.5 meq/g samples showed conductivity of $2*10^{-3}$ S/cm and 1.1 meq/g samples $4*10^{-3}$ S/cm. Activation energies for all samples were on the order of 6-7 kJ/mol.[38]

Marschall and co-workers also studied sulfonic acid functionalized mesoporous materials by grafting mercaptopropyltrimethoxy silane (MPTMS) onto MCI-41, SBA-15, and SBA-16 and post synthetically oxidizing the thiol groups to sulfonic acids by treatment with 30 wt% hydrogen peroxide. Impedance spectroscopic characterization was performed on pressed pellets held between two graphite sheets and two porous stainless steel electrodes. The relativity humidity of the sample was adjusted between 50% and 100% using a tank of heated water. Proton conductivity was shown to increase as a function of acid loading in each of the three framework types and as a function of temperature for

fixed loading at 100% RH, and as a function of relative humidity for fixed temperature and acid loading. No clear trend was observed in conductivity with pore size or shape from MCM-41 to SBA-15 to SBA-16.[39]

Marschall later prepared acid functionalized MCM-41 from MPTMS in a one-pot synthesis. When 20 % or 30 % atomic silicon was supplied by the MPTMS, crystallized samples remained porous upon removal of the cetyltrimethylammonium bromide (CTAB) structure directing agent while samples prepared with 40 % atomic silicon supplied from MPTMS were not found to be porous. Conductivity for pure silica samples was found to be very low (~10^{-7} S/cm at 80 °C) while samples from synthesis batches containing 20 % MPTMS and 30 % MPTMS exhibited conductivities of ~10^{-4} S/cm and ~10^{-3} S/cm, respectively. In both porous samples, conductivity was observed to increase with increasing temperature.[40]

Alabi prepared a carboxylic acid containing mesoporous material from an alkene containing surfactant. After silica condensation, ozone was used to cleave the alkene and oxidize the resulting alkyl chain to a carboxylic acid. The hope was to prepare a material in which the carboxylic acid groups were in close enough proximity to one another to facilitate fast proton transport down the mesopore. While conductivities in between $1*10^{-3}$ and $6*10^{-3}$ S/cm were observed over the temperature range 20-100 °C, the material lost porosity upon ozonation.[42]

Finally, Holmberg was first to report on the proton conducting properties of acid functionalized zeolite beta.[35] Phenethyl containing nanocrystalline zeolite

beta samples were synthesized by the addition of phenethyltrimethoxy silane to a known recipe[37] and the para position of the phenyl ring was sulfonated by treating crystallites with 96 wt% sulfuric acid at 80 °C. Samples were crystallized from gels containing varying amounts of alumina (SiO_2/Al_2O_3 = 25-400). Proton conductivity was observed to be highest in samples crystallized from gels with lowest SiO_2/Al_2O_3, decreasing from $1.2*10^{-2}$ S/cm in samples with SiO_2/Al_2O_3 = 25 to $3*10^{-3}$ S/cm in samples with SiO_2/Al_2O_3 = 50, and $1*10^{-3}$ S/cm in samples with SiO_2/Al_2O_3 = 100. To rationalize this observation it was suggested that Bronsted acid sites from framework alumina cooperated with the aromatic sulfonic acid groups to increase the proton conductivity.

1.4.2. Proton Conduction in Non Fcid-functionalized Zeotypes

While a mature body of literature exists for cationic conduction in zeolites and zeolite-like materials, which will be addressed later, relatively few reports exist on proton conduction in these materials. This section discusses published experimental and computation results related to proton conduction in zeolitic microporous materials, concluding with their use as gas sensors.

The first report on hydrated proton conduction in zeolites measured by electrical methods dates back to 1981, where Lal prepared the proton exchanged forms of natrolite and mordenite and used AC impedance spectroscopy to study their proton conducting abilities.[43] Natrolite and mordenite powders were exchanged into the ammonium form and heated to desorb ammonia, resulting in the proton exchanged form. In the case of natrolite, 88 % exchange from the

sodium form was achieved while complete exchange was achieved in mordenite. Powdered materials were thoroughly washed and pressed between stainless steel dies in a plastic sleeve with 2 tons force. Measurements were made on 'wet' samples, pressed from powders, without drying after washing, and on samples dried in air at 20 °C and 30 °C. Ammonium exchanged samples of 'wet' mordenite exhibited the highest measured conductivities, ~ $7*10^{-4}$ S/cm, followed by 'wet' NH_4^+-natrolite, ~ $5*10^{-4}$ S/cm, and all samples were sensitive to level of hydration. Dried samples of $NH4^+$-natrolite exhibited conductivities in the range 10^{-7}-10^{-6} S/cm, depending on the drying temperature. After ammonia desorption, conductivity dropped to ~$5*10^{-5}$ S/cm for 'wet' samples of natrolite and mordenite, with dried samples of natrolite exhibiting even lower conductivities, ~$5*10^{-8}$ S/cm.[43]

Kreuer later studied the proton conducting properties of hydrated ammonium and proton forms of zeolite A, analcime, sodalite, and gismondine by impedance spectroscopy.[44] Powdered samples were pressed into freestanding pellets and silver paste was used to paint electrodes onto the pellets faces to make electrical contact with the samples. Fully hydrated NH_4^+-zeolite A (Si/Al = 1.4, $2*10^{-3}$ S/cm) had the highest measured conductivity among all the investigated samples followed by NH_4^+-analcime, NH_4^+-sodalite (Si/Al = 2, Si/Al =1, respectively, $\sigma = 2*10^{-3}$ S/cm for both materials), and NH_4^+-gismondine (Si/Al = 1.67, $8*10^{-5}$ S/cm). Conductivity was observed to decrease with decreasing level of hydration and activation energy was observed to increase with decreasing level of hydration in NH_4^+-zeolite A over the temperature range 0-60

°C. After thermal desorption of ammonia, the conductivity of fully hydrated H-A decreased to $6*10^{-7}$ S/cm. Kreuer concluded that water was not a strong enough base to deprotonate Al-OH Bronsted acid groups, but ammonia, a much strong base, was able to perform this function, facilitating conduction by the vehicular mechanism.[44,45]

Andersen *et al.* extended the study of ammonium exchanged zeolites, using direct current (DC) techniques to investigate electric field induced deamination under flowing hydrogen gas. Samples of zeolites X, Y, and A were exchanged into the ammonium form, pressed into freestanding pellets, and thin, platinum contacts were sputtered onto both pellet faces to act as electrodes and catalytic sites for dissociation of hydrogen gas. A DC signal was applied across the sample and the resulting current was measured. The amount of evolved gas was also measured by reaction with (and subsequent titration of) aqueous sulfuric acid. In an effort to study proton and ammonia transport mechanisms, various gasses and gas combinations were introduced into the sample cell. In the presence of dry argon, electrode reactions ceased and the flow of electrical current stopped. In the presence of ammonia and hydrogen, a steady state current flowed. When pure hydrogen gas was introduced, ammonia was evolved and depleted, and current decreased to a lower level but did not cease. When a mixture of hydrogen and ammonia were reintroduced, the initial current was reestablished. When wet hydrogen was introduced, current initially rose, but decreased as the ammonia vehicle was depleted. Proton conduction by a water vehicular mechanism was thus proposed as the current did not fall to the lower

level observed with a flow of dry hydrogen.[46] Further evidence for vehicular transport in NH_3 containing zeolites is presented in an NMR study of ammonium exchanged chabazite and clinoptilolite, where it is suggested that hopping of protons from one Bronsted acid site to another contributes no more than 1-2% to the total conductivity.[47]

Higazy was the first to investigate the electrical properties of H-ZSM-5 by impedance spectroscopy leading to further study by other groups. H-ZSM-5 was prepared by thermal desorption of ammonium exchanged samples. The resulting powdered material was pressed into freestanding pellets and silver contacts were sputtered onto the pellet faces. Samples were characterized in air over the temperature range 300-700 K.[48] Samples were not dehydrated prior to the first measurement and conductivity was observed to initially decrease with increasing temperature, due to dehydration, and then increase with further increasing temperature, indicating activated behavior.

Franke also studied proton hopping and conduction in H-ZSM-5, investigating the electrical properties of samples with Si/Al = 30, 50, 80, 150, 280, and 1000, leading to a variation of distances between framework aluminum sites. Impedance spectroscopy was used to extract values of proton conductivity arising from site-to-site proton hopping in dehydrated, pelletized H-ZSM-5 materials over the temperature range 423-723 K. Proton conduction in H-ZSM-5 materials decreased with decreasing framework aluminum due to fewer charger carriers and greater distance between equilibrium hopping sites. Activation energy for proton conduction was shown to increase from 90 kJ/mol for H-ZSM-5

with Si/Al = 30 to 126 kJ/mol in H-ZSM-5 with Si/Al = 1000 and classical hopping theory, which suggests $E_A \sim a_0^2$, provided an adequate fit to experimental data where E_A is the activation energy and a_0 is the average distance between aluminum sites. Debye-Hückel Theory was also used to strengthen the claim of proton hopping between charge centers created by framework aluminum. Aluminum sites were modeled as potential wells with various amounts of overlap corresponding to the distance between them, but not accounting for the actual structure of ZSM-5. Experimental data exhibited a trend similar to computationally predicted activation energy values, but fell considerably below the predicted curve.[49-51]

A further study investigated solvent supported transport in H-ZSM-5 by introducing NH_3 or H_2O into the pore network. In samples with a low Si/Al, conductivity as a function of temperature was broken into four regions. At high temperature, activated behavior was observed in accordance with previous discussion on dehydrated H-ZSM-5. At the lowest temperatures, before the onset of any dehydration, transport was only slightly activated, and thus attributed to the Grotthuss mechanism where ammonia or water form the supporting hydrogen bonded network. Increasing the temperature beyond this low temperature region led to the onset of dehydration, breaking up the hydrogen bonded water or ammonia network and activated transport was observed. Transport in this regime was attributed to the vehicular mechanism, H_3O^+ or NH_4^+ dominating proton conduction. In the regime between vehicular transport and dehydrated hopping, near constant conductivity was reported due to the

decreasing contribution from vehicular transport resulting from desorption of strongly associated vehicles (H_2O or NH_3) and the increasing contribution arising from thermally activated proton hopping. In all regimes, materials containing water exhibited higher conductivities and lower activation energies than samples containing ammonia. This was attributed to a higher concentration of water molecules than ammonia molecules in the pores of ZSM-5, as conductivity was observed to increase with increasing concentration of NH_3 in a flowing N_2 stream.[52] Conductivity as a function of water concentration in a flowing stream N_2 stream was not investigated, but would be of interest.

Simon studied the effect of NH_3 on conductivity of H-beta using interdigitated electrode (IDE) structures. Zeolite layers were solution deposited onto IDE structures and resulting samples were dehydrated at 673 K in 80:20 N_2:O_2 by *in situ* resistive heaters fabricated on the back of the IDE chips. Impedance spectroscopy was used to measure the resistance of each sample as geometric scaling was difficult. When plotted in the complex plane, impedance data traced out a high frequency semicircular arc with a low frequency tail. H-beta samples exhibited much greater resistances (x1000) than Na-beta samples. Upon exposure to NH_3 the resistance of H-beta samples decreased, but the resistance of Na-beta remained unchanged, although the slope of the low frequency tail with the real axis decreased, potentially attributed to adsorption of NH_3 onto the contact surface. The activation energy for conduction was also observed to decrease upon exposure to NH_3.[53]

Building upon these results, a number of reports exist regarding the use of various zeolites on IDE structures for gas sensing.[54-57] Sensors based on Na-Y were shown to be sensitive to NH_3, NO, and C_4H_{10}.

1.4.3. Micro- and Mesoporous Materials in Proton Conducting Membranes

In addition to studying proton conductivity in powdered materials, a few reports exist in which micro- and mesoporous materials have been incorporated into membranes and the proton conductivity and methanol permeability of the resulting membranes has been measured. Beginning with microporous materials, initial work was performed by Libby and Cussler, who prepared composite membranes from polyvinyl alcohol (PVA) and mordenite.[58,59] It was hypothesized that the addition of zeolites could decrease the methanol permeability of the composite membrane when compared to Nafion, without reducing the proton conductivity. To improve the proton conducting properties of dealuminated mordenite (Si/Al = 40) (which intrinsically has low proton conductivity, particularly in the dealuminated state) powders were soaked in 1 M sulfuric acid to dope the pores with a proton conducting medium. Composite membranes were cast using various volume fractions of mordenite in PVA and proton conductivity and methanol diffusivity were measured. All samples exhibited lower proton conductivity than Nafion but also lower methanol crossover, leading to higher selectivity for all membranes. Proton conductivity decreased slightly with increasing volume fraction of mordenite, while a more drastic decrease in

methanol permeability with increasing volume fraction of mordenite was observed.

Chen[60] and Holmberg[41,60] were the first to produce composite membranes from Nafion and acid-functionalized zeolite beta. Chen[60] prepared membranes by immersing swollen Nafion membranes in the synthesis gel for phenethyl functionalized nanocrystalline zeolite beta during hydrothermal crystallization. After 7 days at 140 °C, composite membranes were treated with 96 wt% sulfuric acid to sulfonate the phenyl groups attached to the zeolite beta framework, and impart acid functionality, as with the nanocrystalline samples discussed above. Characterization results suggest that nanoparticles of zeolite beta crystallize inside the 4 nm hydrophyllic domains of Nafion and constitute ~5 wt% of the composite membranes. The conductivity of these membranes was nearly unchanged from that of pure Nafion, while methanol permeability was reduced by a factor of ~2. Composite membranes were also used in operating methanol fuel cells and a higher power density was observed in fuel cells containing composite membranes, when compared to fuel cells with pure nafion, particularly when operated with a 5 M methanol feed.

Holmberg also prepared composite membranes by slurrying Nafion with acid functionalized zeolite beta nanocrystalls[35] and casting from dimethylformamide. Membranes were prepared with 2.5 and 5 wt% zeolite content and proton conductivity was measured using a four probe structure under 100 % RH conditions at 25 and 70 °C. *In situ* results for composite membranes (membranes in an operating fuel cell stack) showed proton conductivity values

near that for Nafion and reduced methanol crossover, and hence improved selectivity, when compared to Nafion. *Ex situ* results for composite membranes show similar results to those for Nafion.

Moving to composite membranes containing mesoporous materials, Munkata reported on preparation of a freestanding, macroporous membrane prepared by sintering colloidal silica particles (70-100 nm) that had been mixed with polystyrene beads (~500 nm). The colloidal silica particles were sintered around the polystyrene beads, which were combusted out of the matrix to impart porosity. Acid functionality was imparted to the pore walls (surface of the beads) by either grafting MPTMS followed by oxidation with hydrogen peroxide, or by direct reaction with 1,3-propanesultone. Proton conductivity was measured at 90 % RH as a function of temperature, achieving $6*10^{-3}$ S/cm at 60 °C, and an activation energy of 0.18 eV.[61]

Tezuka prepared inorganic-organic hybrid membranes from 3-aminpropyltriethoxysilane (APTES) and sulfuric acid by adding concentrated sulfuric acid to a mixture of APTES in water and allowing the mixture to gel at 50 °C for one day. X-ray diffraction results suggest a 1-dimensional pore structure, and infrared spectroscopy (IR) shows protonation of the $–NH_2$ groups by the sulfuric acid, leading to ion complexes. Proton conductivity was measured at 200 °C after dehydrating the membranes under dry nitrogen at 200 °C for 2 hours, and values as high as $2*10^{-3}$ S/cm are reported. Membranes prepared purely from APTES exhibited conductivities of 10^{-9} S/cm.[62]

Zhang also prepared porous organic-inorganic membranes from tetraethylorthosilicate (TEOS) by first hydrolyzing the TEOS in water and casting in a mold, followed by heating in air to 400-850 °C to generate porosity. Either 1,3-propanesultone or [3-(2-bromoisobutyryl)propyl]dimethylethoxy followed by reaction with CuBr, 2,2'—dipyridyl, and styrenesulfonic acid sodium salt (to impart aromatic sulfonic acid functionality) were then grafted onto the surface silanols of the membranes and proton conductivity was measured as a function of temperature and relative humidity. For non functionalized membranes, conductivity at a given temperature was observed to increase with relative humidity, but decrease with initial heating temperature (400, 500, 650, 850 °C). This decrease in conductivity was attributed to loss of surface silanols. For membranes acid functionalized through 1,3-propanesultone, conductivity increased with temperature over the range 25-95 °C but decreased with further heating for all values of relative humidity. Conductivities were, however, improved by an order of magnitude when compared to non-functionalized membranes. Membranes functionalized with aromatic sulfonic acids also exhibited increasing proton conductivity with temperature at 40 %RH, but now over the entire temperature range 25-150 °C reaching a maximum conductivity of 0.05 S/cm at 150 °C. This is attributed to a high water holding ability (22 wt %) of these membranes, even when held at 130 °C for 2 days. Fuel cells containing aromatic functionalized silica membranes also showed a marked improvement over Nafion containing fuel cells at 130 °C, while exhibiting nearly identical performance at 65 °C.[63]

Park and coworkers prepared various pure-silica and acid functionalized MCM-41s by one-pot and grafting methods and fabricated composite membranes by sonicating MCM-41 powders in solubalized Nafion and spreading on a glass substrate. Different MCM-41 wt% loadings in Nafion were examined. Membranes prepared from pure silica MCM-41 all showed decreased conductivity and most showed increased methanol permeability when compared to pure Nafion membranes. Similar results were obtained for acid functionalized materials.[64]

Finally, Lin *et.al.,* prepared an organic-inorganic mesoporous silica membrane using the Pluronic L64 block copolymer template, which was calcined out after condensation, resulting in a mesoporous material with 4.8 nm pores. 1,2,2-trifluoro-2-hydroxyl-1-trifluoromethyl-ethane sulfonic acid beta-sultone was then reacted with surface silanols to acid functionalize the pore wall, and composite membranes were created by sonication of 1-6 wt% powdered material (based on Nafion) in 5 wt% Nafion solutions followed by casting in a glass dish. Proton conductivity was measured at 60 °C while submerged in water. Composite membrane results show little improvement (or detriment, for that matter) in proton conductivity when compared to pure Nafion membranes. When compared to composite membranes formed from Nafion non-acid functionalized mesoporous material, a significant improvement in proton conductivity is observed at all inorganic loading levels. Methanol permeability decreased with increasing weight fraction of mesoporous materials, slightly faster for non-acid functionalized materials than for acid functionalized materials. Fuel cell

performance was improved when using composite membranes prepared from Nafion and acid-functionalized mesoporous materials, the greatest improvement over pure Nafion arising from a 5 wt% inorganic loading.[65]

1.4.4. Ion Conduction in Microporous Materials

The following section is meant to introduce the reader to the current state of the literature regarding ionic conduction in zeolites and zeolite-like materials. The interested reader is further directed to three comprehensive review articles on the subject.[66-68]

1.4.4.1. *Zeolites X and Y*

Zeolite X and Y have received the greatest attention in literature on the ion conducting properties of zeolites, perhaps due to early reports revealing a high frequency relaxation in these materials, or because of the wealth of crystallographic knowledge pertaining to the FAU structure, i.e., aluminum framework sites, cation positions, etc.[69-89] This section is broken into three subsections. A review of ionic conduction in dehydrated zeolites X and Y will first be presented, followed, by results in partially hydrated samples. The third subsection will conclude with a discussion of the effects of adsorbed phases on the ionic conducting properties in zeolites X and Y.

1.4.4.1.1. Dehydrated Zeolites X and Y

In the first report on the electrical properties of zeolites X and Y, Freeman synthesized faujasite materials over a range of compositions from Si/Al = 1.2 to Si/Al = 2.6 and prepared samples containing Li, Na, K, Rb, Cs, Tl, Mg, Ca, Sr, and Ba by ion exchange (which was incomplete in some instances). Conductivity

was measured by AC techniques at set frequencies, rather than by the modern technique of measuring the impedance as a function of frequency. None-the-less, conductivity was shown to be activated as a function of temperature for all samples, and decreased as framework aluminum content decreased (Si/Al increased). In zeolite Y, activation energy for cation transport was observed to monotonically decrease with increasing cation radius for monovalent cations and this was attributed to decreased electrostatic interaction between the charge balancing cation and the anionic framework site. The opposite trend was observed for divalent cations and activation energy increased with increasing cation radius. To explain this, it was suggested that the larger of the divalent ions (say Ba and Sr) are more easily charge balanced by spatially separated sites in comparison to the smaller divalent ion (Mg and Ca) because their increased size decreases the distance between the divalent cation and each of the two necessary anionic sites, leading to a deeper potential energy well.[69] Full results were not reported by Freeman for zeolite X samples, but did suggest that conduction arose from at least two different types of cations.

Schoonheydt performed further studies on monovalent exchanged zeolite X and Y samples and, similarly, observed that zeolite X exhibited higher ionic conductivity than zeolite Y. In zeolite X with a Si/Al = 1.25, the order of cation conductivity was Na > K > Li > Rb ~ Cs. The trend in activation energies in zeolite Y samples agrees with Freeman's results, but zeolite X exhibits a different trend. Activation energy decreases from Li to Na and then increases from Na to K to Rb. To explain the increase in activation energy beyond sodium in zeolite X,

it was suggested that cation-cation interaction significantly contributes to the conductivity activation energy. Because of the increased aluminum content in zeolite X when compared to zeolite Y, cations are, on average, closer together.

Further, at low temperatures a peak was observed in a plot of the imaginary part of the permittivity, ε", and in the tan δ spectra suggesting the presence of a relaxation process. Peak intensity decreased with decreasing aluminum content (and was almost nonexistent in low alumina content zeolite Y), and, in combination with crystallographic data and the knowledge that zeolite Y has no occupied III sites, the low temperature (high frequency) relaxation was ascribed to the local motion of an ion (Na or K, in this case) from one II site to another II site, across two III sites; that is II → III → III → II within the α cage.[71,73]

Schoonheydt also investigated ionic conduction and relaxation in calcium and copper partially exchanged faujasites.[75,76] In calcium exchanged samples, conductivity was a strong function of both framework aluminum content and extent of exchange. Synthesis of samples with various Si/Al allowed for the preparation of samples with constant number of sodium ions per unit cell (11) but with different numbers of empty II sites arising from different numbers of Ca^{2+} ions per unit cell. Conductivity increased with an increasing number of vacant II sites in partially exchanged samples even though the Si/Al decreased in creation of additional vacant sites and conduction was therefore ascribed to motion of sodium ions by a vacancy mechanism from an occupied II site to an unoccupied II site. Activation energy for supercage sodium ion transport also decreased for partially exchanged samples due to the presence of the calcium ions. A dielectric

absorption process was also observed and attributed to local relaxation of calcium ions in the small cages, although the author of this thesis is not completely convinced.[75]

Copper exchanged samples exhibited activated transport, although two different slopes were observed in the Arrhenius plots of conductivity versus temperature. At low levels of copper exchange, a single slope was observed while at higher levels of exchange two slopes appeared, one at higher temperatures and a second at lower temperatures. Thus, conduction at higher temperatures was attributed to hopping of both copper and sodium ions, while conduction at lower temperatures, and in samples with a low level of exchange, was attributed to hopping of sodium ions.[76]

Jones investigated the electrical properties of dehydrated samples of partially exchanged iron containing zeolite Y samples and silver exchanged zeolite X samples.[78,79] Iron was shown to have replaced 60% of the initial sodium ion content. Both partially iron exchanged zeolite Y and Ag-Y exhibited a single relaxation peak in the ε" spectra that shifted to higher frequencies with increasing temperature. The relaxation peak was absent at room temperature in partially iron exchanged zeolite Y and only appeared at elevated temperatures. This is in accordance with other reported results on zeolite Y. Conductivity in the silver exchanged material was reported to be $5*10^{-8}$ S/m at 97 °C. Further discussion of these materials follows in Section 1.4.4.1.3.

Tabourier prepared zeolite X samples with various rubidium exchange levels and observed a decrease in the peak frequency in the ε" spectra with

increasing rubidium exchange and suggested that motion of sodium and rubidium ions could not be separated as in the cases of the divalent calcium and copper ions previously discussed.[80,81] Further investigation, however, is necessary in the opinion of the author of this thesis.

Andersen and co-workers exchanged Na-X to various levels of lithium cations and observed a monotonic decrease in conductivity and increase in activation energy with increasing lithium content. This is in accordance with previous work and further illustrates the tighter binding of lithium ions to anionic framework sites. Partially exchanged cesium samples were also characterized and had low conductivity at 150 °C ($5*10^{-10}$ S/cm).[83]

Abdoulaye used impedance spectroscopy to measure the ionic conductivity of dehydrated Na-Y and H-Y, and observed that Na-Y possessed much great conductivity and lower activation energy than H-Y. Little explanation was offered.[86]

Simon approached the study of ionic motion in zeolites X and Y through the use of modulus spectroscopy.[89] Sodium exchanged samples were characterized using ac impedance spectroscopy over the frequency range 10 Hz-10 MHz and the temperature range 293 to 673 K. When impedance data was presented in modulus representation (see Chapter 2 for further discussion) two peaks were observed in the plot of imaginary party of the modulus versus frequency for both zeolite X and zeolite Y, one peak at higher frequencies and one at lower frequencies. Peaks shifted to lower frequencies with decreasing temperature. Activation energies were extracted from the change in peak

frequency with temperature and zeolite X had lower values than zeolite Y for both high and low frequency peaks (X, LF = 68 KJ/mol HF = 41 kJ/mol; Y, LF = 80 kJ/mol, HF = 72 kJ/mol). The low frequency peak was attributed to long range ionic conduction (hopping from one II site to another II site on an adjacent cage) while the high frequency peak was attributed to the local relaxation of a sodium ion in the large α cage (II → III → III → II) as was previously suggested by Schoonheydt and discussed above.

Finally, Nicolas used dielectric spectroscopy to study cation dynamics in Na-Y. Zeolite powder was compacted into pellets that were sandwiched between two thin (10 μm) sheets of PTFE. The sandwich structure was then placed between platinum electrodes and the frequency response of the sample was measured from 10^{-2} to 10^{6} Hz. The distribution of trapping energies ($\Delta G(E)$) was fit to the ε" spectra measured from 0 to 170 °C, and three peaks were observed. Each peak was attributed to a unique cation position, SI, SI', and SII, and this distribution was observed to change upon the adsorption of various amounts of methanol.[90]

1.4.4.1.2. Hydrated Zeolite X and Y

Jansen studied the electrical properties of four faujasite zeolites with varying Si/Al ratios in the sodium and potassium exchanged forms. As Schoonheydt[72] reported in dehydrated samples (and attributed to local motion of a sodium ion in the α supercages of the FAU structure), a relaxation peak is observed in the ε" spectra for zeolite X and the peak position shifts to lower frequencies with increasing water content in partially hydrated samples. In zeolite

Y, however, this peak is initially absent, and only appears with the addition of water to the sample, suggesting promotion of a sodium (or potassium) cation to a III site. Activation energy for fully hydrated samples is decreased compared to dehydrated samples, as may be expected from the weakening of the interaction of the cation with the anionic framework upon the addition of water to the zeolite pores.[74]

Results from Abdoulaye also confirm that residual water in the pores of zeolites X and Y can lead to increased conductivity.[87] Stamires further observed this effect.[70] Dehydration was shown to have less of an effect on the conductivity of zeolite X than zeolite Y due to the increased number of sodium ions residing at III sites in hydrated zeolite Y in which, upon dehydration, cations occupy the more energetically favorable II sites.[88] In zeolite X, however, II sites are completely occupied in both the hydrated and dehydrated states, and the number of cations located at III sites does not significantly change upon hydration. Recall that sodium ions occupy III sites in dehydrated zeolite X, while they do not occupy III sites in dehydrated zeolite Y as they are less energetically favorable than other available sites. Contrary to the results of Jansen, however, activation energy in zeolite X samples is observed to decrease with decreasing hydration. In agreement with Janson, activation energy for zeolite Y samples decreased with increasing hydration. This is perhaps due to two competing factors; the population of III sites, which is facilitated by water in zeolite Y but not X, and the likelihood of a successful jump, which could be hindered by water or the increased cation density in zeolite X.[87] Stamires' data may support this

hypothesis as samples characterized at 335 °C showed a decrease in conductivity with increasing water content (over a very small range of water content because of the elevated temperature) while samples characterized at lower temperatures exhibited the opposite trend of increasing conductivity with increasing water content.[70]

Haidar and Jonscher also examined the electrical properties of partially hydrated zeolite X and zeolite Y and, while data was presented in terms of complex capacitance (C*), observed similar relaxation features at elevated water content.[82]

One further report exists on the conductivity of hydrated lanthanum exchanged zeolites X and Y, but the author of this thesis does not think the results add to this work. The reference is simply added for completeness.[85]

1.4.4.1.3. Effect of Adsorbed Phases on Conductivity

Other adsorbate phases have also been shown to affect the conductivity and activation energy of zeolites. Stamires showed that the adsorption of ammonia had a similar affect as the adsorption of water, reducing the activation energy even more drastically than water adsorption in Na-X. The adsorption of triethylamine and 2,2-dimethylbutane both decreased the conductivity in Na-X, while acetonitrile led to an increase in conductivity. Sterics must play a role. Furthermore, the adsorption of both molecular oxygen and nitrogen also increased the conductivity at -76 °C.[70] This was attributed to weakening of the interaction of the sodium ions with the lattice due to interactions with the adsorbed gas molecules.

Jones investigated how polar and non-polar adsorbates influenced the electrical properties of the aforementioned Ag-X and partially iron exchanged zeolite Y. Results from partially iron exchanged samples were presented in terms of dielectric relaxations (peaks in the ε" spectra) and conductivity values are not reported. Adsorbates, however, did give rise to additional relaxation peaks in the ε" spectra. A rationalization of these peaks is attempted and the reader is referred to the appropriate reference.[78] Ammonia and acetonitrile adsorption in Ag-X led to the appearance of addition peaks in the ε" spectra and increased the conductivity of the materials. Again, a rationalization is presented and the reader is referred to the original reference.[79]

1.4.4.2. *Zeolite A*

The ionic conducting abilities of zeolite A, due to its high framework aluminum content, have also attracted attention dating back to an early report by Freeman.[69] Monovalent cation containing zeolite A materials were ion exchanged into Li^+, Na^+, Ag^+, and K^+ forms and activation energy was observed to decrease from lithium to a minimum in the sodium exchanged form and then increase to silver and further to potassium. With the exception of lithium, activation energies in zeolite A samples had higher activation energies than correspondingly exchanged zeolite X samples, possibly due to the smaller channel system of zeolite A.[69] This trend was also observed by other authors.[84,91] Kelemen further reported ion conductivities in zeolite A containing lithium, sodium, potassium, and rubidium cations and conductivity followed a similar trend as activation energy reaching a maximum in the sodium exchanged sample.[91]

Morris published a series of articles focusing on dielectric relaxation in 3-A, 4-A, 5-A, and Ag-A, and two relaxation peaks were observed in the ε" spectra. Zeolite 4-A and Ag-A were the only single-cation containing materials and thus no further discussion is presented. The reader is referred to the original references for a complete discussion including the effects of adsorbed phases on the observed relaxation peaks.[92-94]

Finally, Ohgushi investigated the dielectric properties of dehydrated Na-A (4-A) and observed two relaxation peaks in the ε" spectra as was reported by Morris[92-94] and Simon.[95] The high frequency relaxation peak (relaxation II) had an activation energy of 49 kJ/mol while the low frequency relaxation (relaxation I) exhibited an activation energy of 64 kJ/mol. Simon,[95] Stamires,[69] and Cvjeticanin[84] reported similar values. The high frequency peak shifted to lower frequencies with decreasing temperature and the DC conductivity was observed to increase with increasing temperature to a maximum measured value of ~1 x 10^{-8} S/cm at 500 K. In a subsequent study Ohgushi prepared Na_{11}-H_1-A, that is, zeolite A in which one of the charge balancing sodium ions was replaced by a proton and observed two relaxation peaks as in the case of purely sodium exchanged zeolite A. Upon adsorption of a small number of water molecules per unit cell, both relaxation peaks were affected, indicating that both relaxations arise from the same cation (or more specifically equivalent cations which can jump to non-equivalent neighboring positions). By comparison with related materials (Na_{10}-Ca_1-A and Na_{11}-ZK-4) that do not contain cations in the S3 site (a

site near a 4-ring) one relaxation peak was attributed to a sodium ion in the S3 position.[96]

1.4.4.3. *ZSM-5*

ZSM-5 is one of the most important industrial microporous catalysts, and was characterized by impedance spectroscopy by a number of groups in the late 1980s and 1990s.[97-102] Buckley used modulus spectroscopy to study lithium, sodium, and cesium forms of ZSM-5 and observed two peaks in the M" spectra of Na-ZSM-5 (Si/Al = 40), both shifting to higher frequency with increasing temperature. The low frequency peak was attributed to an interparticle relaxation, but, as the sample did not have deposited contacts and was rather sandwiched between platinum plates, this low frequency peak arises from the overall macroscopic resistance of the sample. For further discussion of this, see Section 2.6. A high frequency peak was also observed and did not change intensity with framework aluminum content. In combination with IR results, Buckley suggested that the high frequency relaxation arose from internal silanols, although the author of this thesis is skeptical and suggests that the high frequency relaxation could also arise from the most stable cation site, as a pure silica sample was not investigated. Further results showed that the conductivity activation energy, lowest for cesium exchanged ZSM-5 and greatest for lithium exchanged ZSM-5, increased with decreasing framework aluminum content and that a maximum in conductivity was observed for sodium exchanged forms followed by cesium and lithium.[97]

Ohgushi performed dielectric measurements on Na-ZSM-5 material with Si/Al = 13 and observed two high frequency relaxation. Upon adsorption of a small amount of water, the peak at higher frequency was affected while the peak at lower frequency did not change position or height. It was suggested, in accordance with NMR results, that two types of sodium cations exist in Na-ZSM-5 and one is preferentially hydrated before the other.[98] When Na-ZSM-5 with a higher Si/Al ratio was studied (Si/Al = 685) one relaxation peak was observed, in accordance with Buckley.[97,99] The peak was not affected by low levels of hydration.

Nischwitz investigated ionic conductivity in Li, Na, K, and Rb containing samples of ZSM-5 with Si/Al = 6.5, 8.2, 24, 27, 55, 83, and 150. Conductivity decreased in the order Na > K > Rb > Li, and was maximum for each respective cation in samples with Si/Al = 6.5. Conductivity decreased with increasing Si//Al, with the exception of Si/Al = 150, in which conductivity increased slightly in Na, K, and Rb containing samples when compared to the respectively exchanged sample with Si/Al = 83. For all Si/Al, conductivity activation energy decreased with increasing cation radius, Li>Na>K>Rb, linearly for samples with Si/Al = 150, but non-linearly for the other materials.[100]

1.4.4.4. *Analcime*

Data on the conductivity of various cation exchanged forms of analcime date back to the 1950s in reports by Beattie.[103-105] Analcime was cation exchanged into lithium, sodium, potassium, silver, rubidium, thallium, and cesium forms, and dehydrated, pressed pellets were investigated over the temperature

range 25-400 °C. Conductivity increased in the order Na > Ag > Li > K > Tl > Rb > Cs, although activation energy followed a different trend, initially decreasing from lithium to sodium, then increasing Na < K < Ag < K < Rb < Cs. Conductivity data agrees with data presented by Barrer and Rees on self-diffusion of alkali metal ions in analcite.[106] The activation energy of thallium exchanged materials fell below those of rubidium and potassium, but above that of silver.[104] Kelemen also studied ionic conductivity in alkali cation containing analcime, and trends in conductivity and activation energy agree with those reported by Beattie.[91,107] Further, when sodium exchanged samples were hydrated, conductivity increased.[105]

1.4.4.5. *Sodalite*

A number of reports exist in which the electrical properties of sodalite have been examined.[107-111] Kelemen prepared two sodalite materials (Si/Al = 1 and Si/Al = 5) and exchanged in lithium, sodium, potassium, and rubidium. In exchanged samples of both materials conductivity increased in the order Rb < Na ~ Li < K while activation energy exhibited a minimum for the sodium exchanged sample in the material with Si/Al = 1 (Li > Na < K ~ Rb) and a minimum for the potassium exchanged sample in the material with Si/Al = 5 (Li > Na > K < Rb). For specific conductivity values the reader is referred to the original references (~10^{-5} S/cm at 400 °C for Si/Al = 1 and 10^{-6} S/cm at 400 °C for Si/Al = 5).

Promotion of cation motion by other ions (halides, chromate, etc.) in sodalite has also been studied.[109-111] It was shown that the presence of anions in

the sodalite cages modified the potential energy landscape and influenced the motion of the sodium cation.

1.4.4.6. *Offretite*

Kelemen has studied the ionic conductivity of alkali metal exchanged offretite with Si/Al = 2.4, 3, and 5 in the lithium, sodium, potassium, and rubidium exchanged forms. Conductivity of sodium and lithium exchanged materials increased monotonically with increasing aluminum content, but exhibited a maximum in the material with Si/Al = 3 for K and Rb exchanged samples. This was potentially due to the higher cation-cation repulsion between the larger cations (K, Rb) in materials with a Si/Al = 2.4 while the smaller ions (Li, Na) do not “feel” this repulsion to the same extent as K and Rb. For all Si/Al, conductivity followed the order Na>Li>K>Rb and activation energy exhibited a minimum for sodium exchanged samples, lithium exchanged samples having the highest activation energy in samples with Si/Al = 3.5.

1.4.4.7. *Chabazite*

Beattie studied the ionic conducting properties of natural chabazite ion exchanged into Li, Na, Ag, K, Rb, Tl, and Cs forms and conductivity of dehydrated samples increased in the order Li > Tl > Na > K > Ag > Rb > Cs.[104] Activation energy exhibited a minimum in the sodium form and followed the order Na < Li ~ K < Rb ~ Ag < Cs.

1.4.4.8. *Mordenite*

Ohgushi examined the dielectric properties of three mordenite samples with different aluminum contents (Si/Al = 4.9, 9.9 exchanged with sodium, and

Si/Al = 9.9 exchanged with sodium and protons) and observed two relaxation peaks in the ε" spectrum. All three materials have sodium ions in a "side pocket" while only materials with Si/Al = 4.9 have additional sodium ions in the straight channels. Thus, dielectric loss peaks were attributed to relaxation of the sodium ion in the "side pockets". Further confirmation of this was claimed through the characterization of hydrated samples. Both loss peaks were affected by the addition of a few water molecules per unit cell, indicating that the relaxation peaks arise from equivalent sodium ions. Hydration did, however, influence the ε" spectra of samples partially exchanged with protons less than samples in the pure sodium form.[112]

Douillard used the same technique that Nicolas used to study cation dynamics in Na-Y to investigate ionic relaxations as functions of water uptake in mordenite. In the case of mordenite, the energy distribution function ($\Delta G(E)$) was not calculated to investigate unique framework sites, but the relaxation peak in the ε" spectra was thermally activated and the activation energy decreases with increasing water content.[113]

1.4.4.9. *Ferrierite*

Yamamoto grew single crystal samples of ferrierite and measured sodium ion conductivity and activation energy along the 10 membered ring channels of the [001] direction and the 8 membered ring channels of the [010] direction. Silicon to aluminum ratio was reported to be >60, low compared to zeolite X and many of the other zeolites discussed above. Conductivity in both crystallographic directions was thermally activated, conductivity in the [010] direction significantly

greater than conductivity in the [001] direction, while activation energy in the [010] direction (1.2 eV) was greater than the activation energy measured for transport in the [001] direction (0.84 eV). Sterics in the 8 MR pores was suggested to explain the increased activation energy. It was further suggested that the increased conductivity in the direction of the 8 MR pores was observed because of the increased number of parallel conduction pathways in the [010] direction from the higher density of 8 MR pores when compared to the number density of 10 MR pores in the [001] direction. That is, conduction along an 8 MR pore was not necessarily faster than conduction along a 10 MR pore, but that there are fewer parallel "ionic resistors" in the [001] direction.[114]

1.4.4.10. *Zeolite L*

Relaxation of potassium ions in zeolite L with Si/Al = 3 was examined by Ohgushi over the temperature range 392-633 K and one peak in the ε" spectra was observed, although, it was suggested that this peak was the combination of two relaxations. This suggestion arose from a decrease in intensity in the ε" spectra at lower frequencies without a significant change at higher frequencies upon partial exchange of the potassium ions by protons. This main relaxation that decreased in intensity with increasing proton exchange was attributed to potassium ions located at D sites, as the tetraethylammonium ions used to generate the partially exchanged proton forms are too large to penetrate the 4-membered rings in zeolite L and thus only exchange with the D sites that face the 8 MR channels. Further, the activation energy extracted from the peak frequency

versus temperature data decreased with increasing exchange, and this was attributed to less cation-cation repulsion (or cation-proton repulsion).[115]

1.4.4.11. *Tin Containing Zeolites*

Four reports exist regarding tin containing mordenite and zeolite Y, but the prepared systems were two-phase composite materials containing tin-exchanged zeolites and tin-oxide, and further discussion is, therefore, not presented in this review of ion conductivity in microporous materials. The reader is referred to the original references for a complete description.[116-119]

1.4.4.12. *ETS-10*

The only known report on divalent ion conductivity in a microporous material was presented by Wei and Hillhouse for the octahedral titanium containing ETS-10. Copper(II) was exchanged into the pores of ETS-10 which exhibited greater conductivity and an activation energy 15 kJ/mol lower than that for copper(II) exchanged zeolite X. [120] Modulus spectroscopy was also used to examine sodium ion conductivity in ETS-10, and a high frequency relaxation and low frequency relaxation were observed. The low frequency peak had an activation energy of 54.6 kJ/mol, lower than that measured for Na-X by the same authors (62.9 kJ/mol) and the high frequency peak had an activation energy of 45.3 kJ/mol.[120]

1.5. References

(1) Gierke, T. D.; Munn, G. E.; Wilson, F. C. *Journal of Polymer Science Part B-Polymer Physics* **1981**, *19*, 1687.

(2) Hsu, W. Y.; Gierke, T. D. *J. Electrochem. Soc.* **1982**, *129*, C121.

(3) Hsu, W. Y.; Gierke, T. D. *J. Membr. Sci.* **1983**, *13*, 307.

(4) de Grotthuss, C. J. T. *Ann. Chim. (Paris)* **1806**, *58*, 54.

(5) Choi, P.; Jalani, N. H.; Datta, R. *J. Electrochem. Soc.* **2005**, *152*, E123.

(6) *Handbook of Batteries*; McGraw-Hill, 2001.

(7) Camblor, M. A.; Corma, A.; Valencia, S. *Chem. Commun.* **1996**, 2365.

(8) Camblor, M. A.; Corma, A.; Valencia, S. *J. Mater. Chem.* **1998**, *8*, 2137.

(9) Davis, M. E. *Zeolites: A Refined Tool for Designing Catalytic Sites* **1995**, *97*, 35.

(10) Davis, T. M.; Drews, T. O.; Ramanan, H.; He, C.; Dong, J.; Schnablegger, H.; Katsoulakis, M. A.; Kokkoli, E.; McCormick, A. V.; Penn, R. L.; Tsapatsis, M. *Nature Materials* **2006**, *5*, 400.

(11) Burkett, S. L.; Davis, M. E. *J. Phys. Chem.* **1994**, *98*, 4647.

(12) Burkett, S. L.; Davis, M. E. *Chem. Mater.* **1995**, *7*, 1453.

(13) Burkett, S. L.; Davis, M. E. *Chem. Mater.* **1995**, *7*, 920.

(14) Fedeyko, J. M.; Egolf-Fox, H.; Fickel, D. W.; Vlachos, D. G.; Lobo, R. F. *Langmuir* **2007**, *23*, 4532.

(15) Jones, C. W.; Tsuji, K.; Takewaki, T.; Beck, L. W.; Davis, M. E. *Microporous Mesoporous Mater.* **2001**, *48*, 57.

(16) Lee, H.; Zones, S. I.; Davis, M. E. *Nature* **2003**, *425*, 385.

(17) Annen, M. J.; Davis, M. E.; Higgins, J. B.; Schlenker, J. L. *J. Chem. Soc., Chem. Commun.* **1991**, 1175.

(18) Camblor, M. A.; Yoshikawa, M.; Zones, S. I.; Davis, M. E. *Chemical Industries* **1997**, *69*, 243.

(19) Freyhardt, C. C.; Lobo, R. F.; Khodabandeh, S.; Lewis, John E.; Tsapatsis, M.; Yoshikawa, M.; Camblor, M. A.; Pan, M.; Helmkamp, M. M.; Zones, S. I.; Davis, M. E. *J. Am. Chem. Soc.* **1996**, *118*, 7299.

(20) Serrano, D. P.; Grieken, R. v.; Davis, M. E.; Melero, J. A.; Garcia, A.; Morales, G. *Chemistry: A European Journal* **2002**, *22*, 5153.

(21) Yoshikawa, M.; Zones, S. I.; Davis, M. E. *Microporous Materials* **1997**, *11*, 137.

(22) Yoshikawa, M.; Zones, S. I.; Davis, M. E. *Microporous Materials* **1997**, *11*, 127.

(23) McCusker, L. B.; Grosse-Kunstleve, R. W.; Baerlocher, C.; Yoshikawa, M.; Davis, M. E. *Microporous Materials* **1996**, *6*, 295.

(24) Rohrig, C.; Gies, H. *Angew. Chem., Int. Ed. Engl.* **1995**, *34*, 63.

(25) Andy, P.; Davis, M. E. *Industrial & Engineering Chemistry Research* **2004**, *43*, 2922.

(26) Takewaki, T.; Beck, L. W.; Davis, M. E. *Top. Catal.* **1999**, *9*, 35.

(27) Takewaki, T.; Beck, L. W.; Davis, M. E. *J. Phys. Chem. B* **1999**, *103*, 2674.

(28) Annen, M., Virginia Polytechnic University.

(29) Camblor, M. A.; Lobo, R. F.; Koller, H.; Davis, M. E. *Chem. Mater.* **1994**, *6*, 2193.

(30) Jones, C. W. *Science* **2003**, *300*, 439.

(31) Jones, C. W.; Tsapatsis, M.; Okubo, T.; Davis, M. E. *Microporous Mesoporous Mater.* **2001**, *42*, 21.

(32) Jones, C. W.; Tsuji, K.; Davis, M. E. *Nature* **1998**, *393*, 52.

(33) Jones, C. W.; Tsuji, K.; Davis, M. E. *Microporous Mesoporous Mater.* **1999**, *33*, 223.

(34) Tsuji, K.; Jones, C. W.; Davis, M. E. *Microporous Mesoporous Mater.* **1999**, *29*, 339.

(35) Holmberg, B. A.; Hwang, S.-J.; Davis, M. E.; Yan, Y. *Microporous Mesoporous Mater.* **2005**, *80*, 347.

(36) Camblor, M. A.; Corma, A.; Mifsud, A.; Perez-Pariente, J.; Valencia, S. *Stud. Surf. Sci. Catal.* **1997**, *105*, 341.

(37) Camblor, M. A.; Corma, A.; Valencia, S. *Microporous Mesoporous Mater.* **1998**, *25*, 59.

(38) Mikhailenko, S.; Desplantier-Goscard, D.; Danumah, C.; Kaliaguine, S. *Microporous Mesoporous Mater.* **2002**, *52*, 29.

(39) Marschall, R.; Bannat, I.; Caro, J.; Wark, M. *Microporous Mesoporous Mater.* **2007**, *99*, 190.

(40) Marschall, R.; Rathousky, J.; Wark, M. *Chem. Mater.* **2007**, *19*, 6401.

(41) Holmberg, B. A.; Wang, Z.; Yan, Y. *J. Membr. Sci.* **2008**, *320*, 86.

(42) Alabi, C. A.; Davis, M. E. *Chem. Mater.* **2006**, *18*, 5634.

(43) Lal, M.; Johnson, C. M.; Howe, A. T. *Solid State Ionics* **1981**, *5*, 451.

(44) Kreuer, K. D.; Weppner, W.; Rabenau, A. *Mater. Res. Bull.* **1982**, *17*, 501.

(45) Kreuer, K.-D.; Rabenau, A.; Weppner, W. *Angew. Chem., Int. Ed. Engl.* **1982**, *21*, 208.

(46) Andersen, E. K.; Andersen, I. G. K.; Skou, E.; Yde-Andersen, S. *Solid State Ionics* **1986**, *18-19*, 1170.

(47) Afanassyev, I. S.; Moroz, N. K. *Solid State Ionics* **2003**, *160*, 125.

(48) Higazy, A. A.; Kassem, M. E.; Sayed, M. B. *J. Phys. Chem. Solids* **1992**, *53*, 549.

(49) Franke, M. E.; Sierka, M.; Simon, U.; Sauer, J. *Physical Chemistry Chemical Physics* **2002**, *4*, 5207.

(50) Franke, M. E.; Simon, U. *Solid State Ionics* **1999**, *118*, 311.

(51) Franke, M. E.; Simon, U. *Phys. Status Solidi B* **2000**, *218*, 287.

(52) Franke, M. E.; Simon, U. *ChemPhysChem* **2004**, *5*, 465.

(53) Simon, U.; Flesch, U.; Maunz, W.; Muller, R.; Plog, C. *Microporous Mesoporous Mater.* **1998**, *21*, 111.

(54) Franke, M. E.; Simon, U.; Moos, R.; Knezevic, A.; Muller, R.; Plog, C. *Physical Chemistry Chemical Physics* **2003**, *5*, 5195.

(55) Kurzweil, P.; Maunz, W.; Plog, C. *Sensors and Actuators B* **1995**, *24-25*, 653.

(56) Plog, C.; Maunz, W.; Kurzweil, P.; Obermeier, E.; Scheibe, C. *Sensors and Actuators B* **1995**, *24-25*, 403.

(57) Scheibe, C.; Obermeier, E.; Maunz, W.; Plog, C. *Sensors and Actuators B* **1995**, *24-25*, 584.

(58) Libby, B.; Smyrl, W. H.; Cussler, E. L. *Electrochem. Solid-State Lett.* **2001**, *4*, A197.

(59) Libby, B.; Smyrl, W. H.; Cussler, E. L. *AIChE J.* **2003**, *49*, 991.

(60) Chen, Z. W.; Holmberg, B.; Li, W. Z.; Wang, X.; Deng, W. Q.; Munoz, R.; Yan, Y. S. *Chem. Mater.* **2006**, *18*, 5669.

(61) Munakata, H.; Chiba, H.; Kanamura, K. *Solid State Ionics* **2005**, *176*, 2445.

(62) Tezuka, T.; Tadanaga, K.; Hayashi, A.; Tatsumisago, M. *J. Am. Chem. Soc.* **2006**, *128*, 16470.

(63) Zhang, X. *J. Electrochem. Soc.* **2007**, *154*, B322.

(64) Park, J. W.; Kim, Y. C.; Jeong, Y. J.; Kim, S. D.; Ha, H. Y.; Kim, W. J. *Microporous Mesoporous Mater.* **2008**, *114*, 238.

(65) Lin, Y.-F.; Yen, C.-Y.; Ma, C.-C. M.; Liao, S.-H.; Lee, C.-H.; Hsiao, Y.-H.; Lin, H.-P. *J. Power Sources* **2007**, *171*, 388.

(66) Simon, U.; Franke, M. E. *Microporous Mesoporous Mater.* **2000**, *41*, 1.

(67) Kalogeras, I. M.; Vassilikou-Dova, A. *Defect and Diffusion Forum* **1998**, *164*, 1.

(68) Kalogeras, J. M.; Vassilikou-Dova, A. *Cryst. Res. Technol.* **1996**, *31*, 693.

(69) Freeman, D. C.; Stamires, D. N. *J. Chem. Phys.* **1961**, *35*, 799.

(70) Stamires, D. N. *J. Chem. Phys.* **1962**, *36*, 3174.

(71) Schoonheydt, R. A.; Uytterhoeven, J. B. *Clay Minerals* **1969**, *8*, 71.

(72) Schoonheydt, R. A.; Uytterhoeven, J. B. *Advances in Chemistry Series* **1971**, *101*, 456.

(73) Jansen, F. J.; Schoonheydt, R. A. *J. Chem. Soc., Faraday Trans. I* **1973**, *69*, 1338.

(74) Jansen, F. J.; Schoonheydt, R. A. *Advances in Chemistry Series* **1973**, 96.

(75) Schoonheydt, R. A.; Wilde, W. d. *J. Chem. Soc., Faraday Trans. I* **1974**, *70*, 2132.

(76) Schoonheydt, R. A.; Velghe, F. *J. Chem. Soc., Faraday Trans. I* **1976**, *72*, 172.

(77) Schoonheydt, R. A. *Proc. Int. Conf. Zeolites* **1980**, *5*, 242.

(78) Jones, G.; Davies, M. *J. Chem. Soc., Faraday Trans. I* **1974**, *71*, 1791.

(79) Jones, G. *J. Chem. Soc., Faraday Trans. I* **1975**, *71*, 2085.

(80) Tabourier, P.; Carru, J.-C.; Wacrenier, J.-M. *J. Chem. Soc., Faraday Trans. I* **1983**, *79*, 779.

(81) Tabourier, P.; Carru, J. C.; Wacrenier, J. M. *Zeolites* **1983**, *3*, 50.

(82) Haidar, A. R.; jonscher, A. K. *J. Chem. Soc., Faraday Trans. I* **1986**, *82*, 3535.

(83) Andersen, E. K.; Andersen, I. G. K.; Metcalf-Johansen, J.; Simonsen, K. E.; Skou, E. *Solid State Ionics* **1988**, *28-30*, 249.

(84) Cvjeticanin, N.; Mentus, S.; Petranovic, N. *Solid State Ionics* **1991**, *47*, 111.

(85) Slade, R. C. T.; Jinku, H.; Hix, G. B. *Solid State Ionics* **1992**, *57*, 177.

(86) Adboulaye, A.; Soulayman, S. S.; Chabanis, G.; Giuntini, J. C.; Zanchetta, J. V. *Microporous Materials* **1997**, *8*, 63.

(87) Abdoulaye, A.; Chabnis, G.; Giuntini, J. C.; Vanderschueren, J.; Zanchetta, J. V.; Renzo, F. D. *J. Phys. Chem. B* **1997**, *101*, 1831.

(88) Adboulaye, A.; Zanchetta, J. V.; Renzo, F. D.; Giuntini, J. C.; Vanderschueren, J.; Chabanis, G. *Microporous Mesoporous Mater.* **2000**, *34*, 317.

(89) Simon, U.; Flesch, U. *J. Porous Mater.* **1999**, *6*, 33.

(90) Nicolas, A.; Devautour-Vinot, S.; Maurin, G.; Giuntini, J. C.; Henn, F. *J. Phys. Chem. C* **2007**, *111*, 4722.

(91) Kelemen, G.; Schon, G. *J. Mater. Sci.* **1992**, *27*, 6036.

(92) Morris, B. *J. Phys. Chem. Solids* **1969**, *30*, 73.

(93) Morris, B. *J. Phys. Chem. Solids* **1969**, *30*, 89.

(94) Morris, B. *J. Phys. Chem. Solids* **1969**, *30*, 103.

(95) Simon, U.; Mohrke, C.; Schon, G. *Chem. Ing. Tech.* **1995**, *67*, 583.

(96) Ohgushi, T.; Sakai, Y. *J. Phys. Chem. C* **2007**, *111*, 2116.

(97) Buckley, R. G.; Tallon, J. L.; Clare, J. F. *Solid State Ionics* **1988**, *28*, 245.

(98) Ohgushi, T.; Kataoka, S. *Journal of Colloidal and Interface Science* **1991**, *148*, 148.

(99) Ohgushi, T.; Kawanabe, Y. *Zeolites* **1994**, *14*, 356.

(100) Nischwitz, P.; Amels, P.; Fetting, F. *Solid State Ionics* **1994**, *73*, 105.

(101) Mikhailenko, S. D.; Kaliaguine, S.; Ghali, E. *Microporous Materials* **1997**, *11*, 37.

(102) Dubbe, A.; Hagen, G.; Moos, R. *Solid State Ionics* **2006**, *177*, 2321.

(103) Beattie, I. R. *Transactions of the Faraday Society* **1954**, *51*, 712.

(104) Beattie, I. R. *Transactions of the Faraday Society* **1954**, *50*, 581.

(105) Beattie, I. R.; Dyer, A. *Transactions of the Faraday Society* **1956**, *53*, 61.

(106) Barrer, R. M.; Rees, L. V. C. *Transactions of the Faraday Society* **1960**, *56*, 709.

(107) Kelemen, G.; Lortz, W.; Schon, G. *J. Mater. Sci.* **1989**, *24*, 333.

(108) Barrer, R. M.; Saxon-Napier, E. A. *Transactions of the Faraday Society* **1962**, *58*, 145.

(109) Jaing, M. R. M.; Weller, M. T. *J. Chem. Soc., Faraday Trans.* **1991**, *87*, 3787.

(110) Jordan, E. *Angew. Chem., Int. Ed. Engl.* **2007**, *46*, 3359.

(111) Jordan, E.; Bell, R. G.; Wilmer, D.; Koller, H. *J. Am. Chem. Soc.* **2006**, *128*, 558.

(112) Ohgushi, T.; Kubo, K. *J. Chem. Soc., Faraday Trans.* **1998**, *94*, 3769.

(113) Douillard, J. M.; Maurin, G.; Henn, F.; Devautour-Vinot, S.; Giuntini, J. C. *J. Colloid Interface Sci.* **2007**, *306*, 440.

(114) Yamamoto, N.; Okubo, T. *Microporous Mesoporous Mater.* **2000**, *40*, 283.

(115) Ohgushi, T.; Numata, T. *Physical Chemistry Chemical Physics* **2006**, *8*, 3774.

(116) Andersen, I. G. K.; Andersen, E. K.; Knudsen, N.; Skou, E. *Solid State Ionics* **1991**, *46*, 89.

(117) Knudsen, N.; Andersen, E. K.; Andersen, I. G. K.; Norby, P.; Skou, E. *Solid State Ionics* **1993**, *61*, 153.

(118) Knudsen, N.; Andersen, E. K.; Andersen, I. G. K.; Skou, E. *Solid State Ionics* **1989**, *35*, 51.

(119) Knudsen, N.; Krogh, E.; Andersen, I. G. K.; Skou, E. *Solid State Ionics* **1988**, *28-30*, 627.

(120) Wei, T.-C.; Hillhouse, H. W. *J. Phys. Chem. B* **2006**, *110*, 13728.

2. Instrumentation

2.1. Introduction to Impedance Spectroscopy

Impedance spectroscopy (IS) is a powerful tool for studying the electrical properties of solid and liquid systems and continues to find increasing use in electrochemistry, materials science, and other fields. Use of the phrase “electrical properties” should not simply be interpreted as relating to “electronic conduction” arising from the transport of electrons or holes, and encompasses not only electronic conduction but also ionic conduction, electrochemical reactions, polarization in bulk and at interfaces, and any other process arising from motion of a charged species, be that motion long range or short range. IS has been used to study many materials properties including ionic conductivity, relaxation in polymers, reactions at electrode surfaces, charge and discharge processes in batteries, fuel cells, etc., and the interested reader is referred to *Impedance Spectroscopy: Theory, Experiment, and Applications*[1] for an in-depth presentation of the technique.

IS is the technique by which the impedance of a sample (Z^*) is measured as a function of frequency, most commonly accomplished by applying a sinusoidal signal (voltage or current) to a sample and measuring the sample’s response to that signal over a range of applied frequencies. Impedance is a complex quantity composed of both a magnitude and a phase and only decomposes to the more commonly used term “resistance” when the phase is identically zero; that is, the impedance is purely real. Modern instruments for

measuring impedance are commercially available, including the Solartron 1260 and the Novocontrol Alpha and Beta, and various Agilent boxes. These off-the-shelf systems operate over a wide bandwidth of frequencies from a few millihertz to tens of megahertz with high accuracy and standardized terminals for electrical connection.

Spectroscopic data is often presented using one of four related functions; impedance, admittance, permittivity, and modulus. It is important to understand that all representations contain the same materials data and are simply different ways of viewing how a material responds to an applied electrical stimulus. These four related functions, and the transforms among them, are presented in Table 2.1. When data is presented in terms of modulus, authors often refer to the data collection technique as modulus spectroscopy. Similarly, when data is presented in terms of complex dielectric constant, dielectric spectroscopy is often used, but all three names refer to the same technique of measuring the response of a sample to an applied AC signal.

Historically, data from the characterization of insulating materials has been presented in terms of the complex dielectric constant, ε^*, and loss tangent δ ($\tan \delta = \varepsilon''/\varepsilon'$), and modulus form ($M^*$) is often used to overemphasize features occurring at higher frequencies.

In the next two subsections, mathematical models are presented to familiarize the reader with dielectric relaxation and conduction in solid state materials.

Table 2.1. Impedance functions and their transforms.

	M	Z	Y	ε
M	-	$j\omega C_c Z$	$j\omega C_c Z$	$1/\varepsilon$
Z	$M/j\omega C_c$	-	$1/Y$	$1/j\omega C_c \varepsilon$
Y	$j\omega C_c Z$	$1/Z$	-	$j\omega C_c Z$
ε	$1/M$	$1/j\omega C_c Z$	$Y/j\omega C_c$	-

ω is the angular frequency ($2\pi f$), C_c is the open cell capacitance, defined as $\varepsilon_0 A/d$, where ε_0 is the permittivity of free space, A is the cross-sectional area of the sample, and d is the thickness of the sample.

2.1.1. Dielectric Relaxation

Relaxation process in materials (solids, liquids, gases) arise from the local polarization, **P**, of electrical dipoles within the material of interest. Polarization of dipoles is accomplished by the application of an electric field and can be broken into contributions arising from the fast responding electron cloud, $\mathbf{P}_\infty$, (displaced in relation to the positively charged nucleus) and a much slower responding, and thus time dependant, polarization due to the orientation of dipoles in the applied electric field, **P'**(t). After equilibration with the applied electric field, a total, static polarization is achieved, $\mathbf{P}_s$. Defining dielectric constants as in Equation (2.1) and Equation (2.2) and,

$$\varepsilon_\infty - 1 = \boldsymbol{P}_\infty / \boldsymbol{E}\epsilon_0 \tag{2.1}$$

$$\varepsilon_s - 1 = \boldsymbol{P}_s / \boldsymbol{E}\epsilon_0 \tag{2.2}$$

the total polarization as

$$\boldsymbol{P}_s = \boldsymbol{P}_\infty + \boldsymbol{P}'(t=0) \tag{2.3}$$

and assuming a single relaxation time, τ, and first order kinetics, the governing differential equation is

$$\tau \frac{d\boldsymbol{P}'(t)}{dt} = \boldsymbol{P}_s - \boldsymbol{P}_\infty. \tag{2.4}$$

When **E**, the electric field, is a sinusoidal signal, Equation (2.4) can be solved with Equations (2.1) and (2.2) for the complex dielectric constant as a function of sinusoid frequency, ω,

$$\varepsilon^* - \varepsilon_\infty = \frac{\varepsilon_s - \varepsilon_\infty}{1 + \omega^2\tau^2} - j\frac{\omega\tau(\varepsilon_s - \varepsilon_\infty)}{1 + \omega^2\tau^2}. \tag{2.5}$$

This is the same equation arrived at from the circuit model in Figure 2.1 when $\tau = RC_2$, $C_2 = (\varepsilon_s - \varepsilon_\infty)\varepsilon_0$, and $C_1 = \varepsilon_\infty\varepsilon_0$, and hence, this circuit model is known

as the Debye equivalent circuit. When the real, ε', and imaginary, ε", parts of the dielectric constant are plotted as functions of frequency, plots similar to that shown in Figure 2.2 are observed.

A single relaxation is the simplest possible case and, in general, a distribution of relaxation times exists in solids and the governing equations become more complicated. Distributed relaxation times lead to a broadening of the ε" peak, and a depression of the semicircular arc, if plotted in the complex plane, that is ε" versus ε'.

When the Debye circuit equations are plotted in the complex Z* plane, a vertical line is observed, as shown in Figure 2.3.

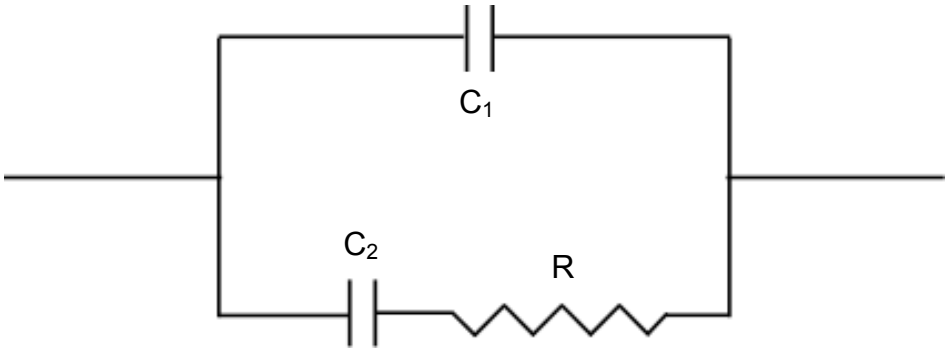

Figure 2.1. Debye equivalent circuit.

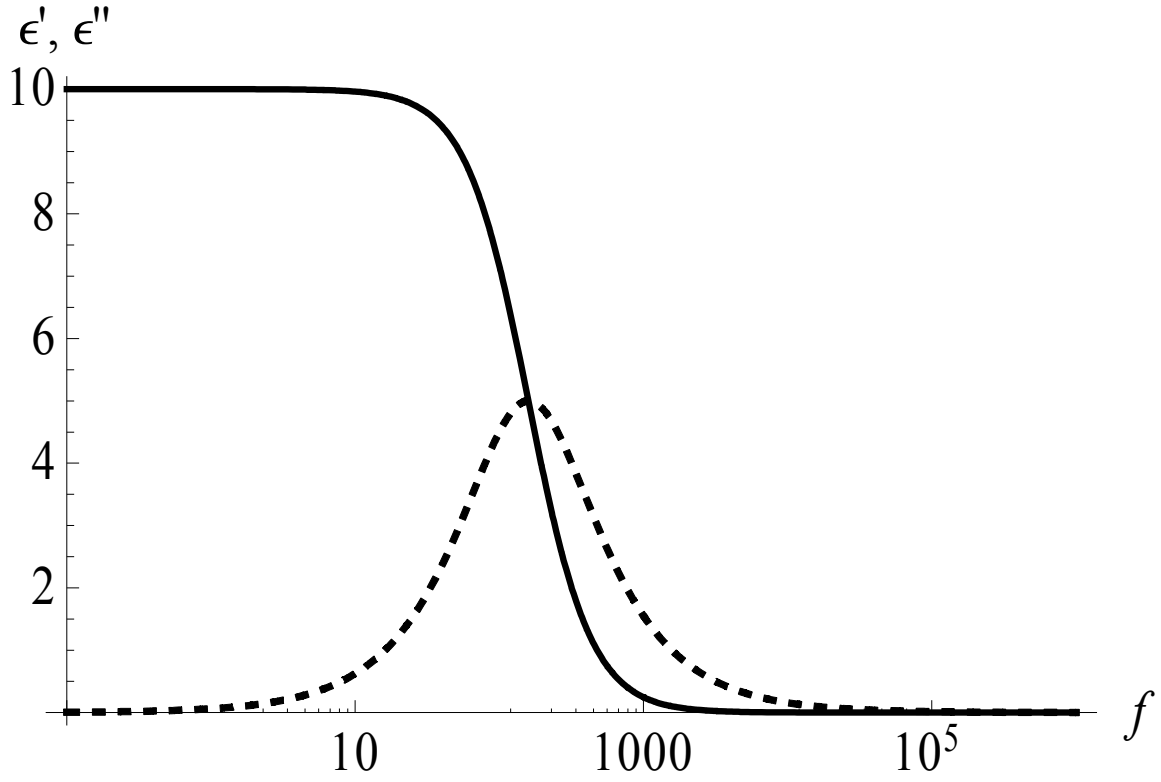

Figure 2.2. ε’ (solid) and ε” (dashed) as functions of frequency for Debye relaxation.

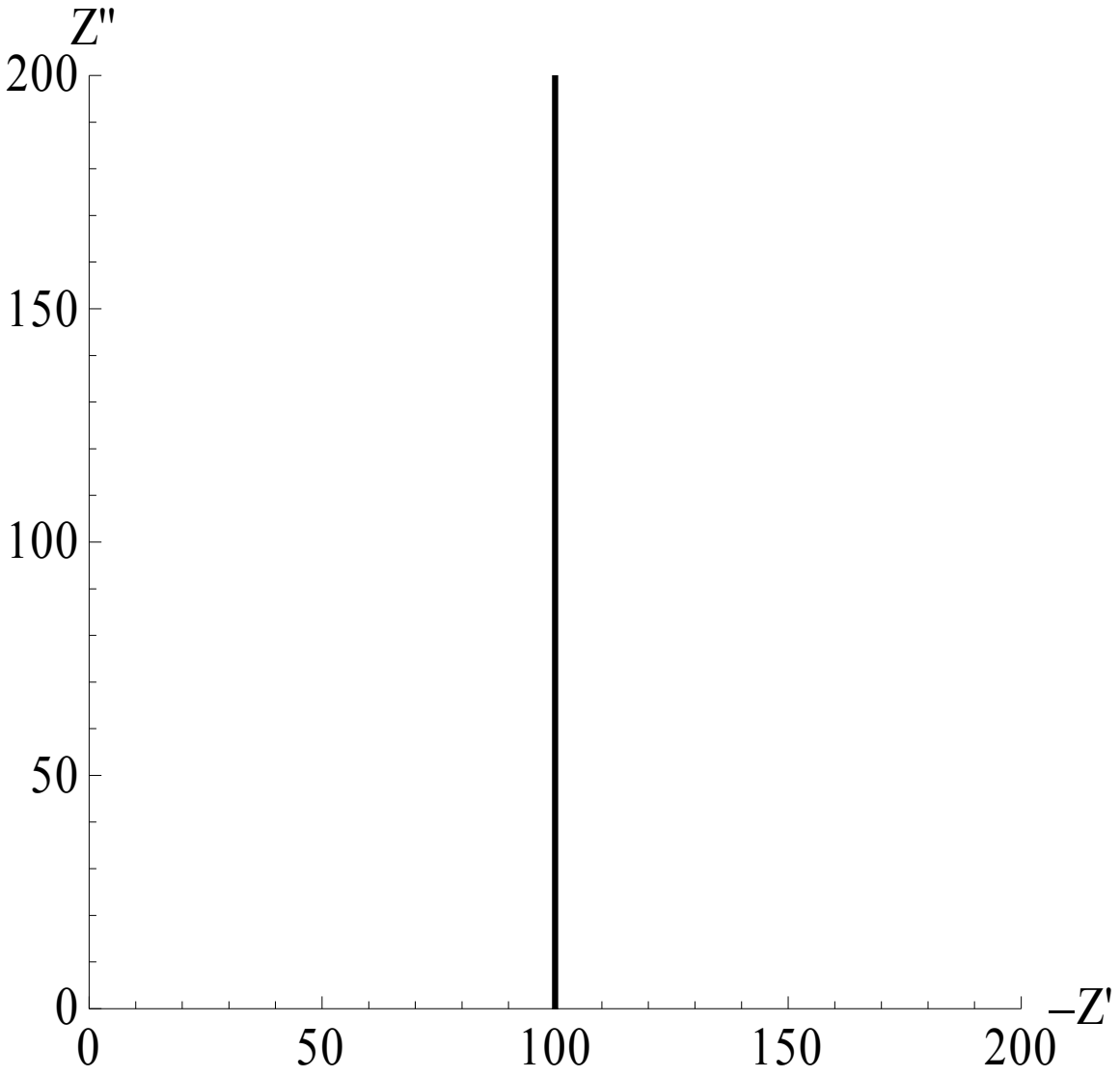

Figure 2.3. Debye circuit plotted in complex Z* plane.

2.1.2. Conduction

Conductivity in the absence of a concentration gradient, that is, motion of charge carriers driven purely by an applied electric field, can be described as

$$\sigma_{DC} = Cz\mu_D, \tag{2.6}$$

where μ_D is the drift mobility, C the concentration of mobile ions, z the charge of the carrier. For cation hopping, this can further be described by

$$\sigma_{DC} = \frac{Nc(1-c)z^2l^2\gamma}{kT}\omega_p, \tag{2.7}$$

where N is the number of cation sites per unit volume, c is the cation site occupancy, *l* is the jump distance, γ is a geometrical factor, *k* is Boltzman's constant, T is the temperature, and ω_p is the characteristic hopping frequency. ω_p can further be described as

$$\omega_p = \omega_0 \exp\left(-\frac{\Delta G_h}{kT}\right) = \omega_0 \exp\left(\frac{\Delta S_h}{k}\right)\exp\left(-\frac{\Delta H_h}{kT}\right), \tag{2.8}$$

where ΔG_h is the Gibbs free energy for hopping, ΔS_h the hopping entropy, and ΔH_h the hopping activation energy. The concentration of mobile ions may be thermally activated as well and is described as

$$c = c_0 \exp\left(-\frac{\Delta G_c}{kT}\right) = \omega_0 \exp\left(\frac{\Delta S_c}{k}\right)\exp\left(-\frac{\Delta H_c}{kT}\right), \tag{2.9}$$

where terms are as described above but now refer to the concentration of mobile ions. Inserting Equations (2.8) and (2.9) into Equation (2.7), the dc conductivity can be written

$$\sigma_{DC} = \frac{\sigma_0}{T} exp\left(-\frac{E_A}{kT}\right), \tag{2.10}$$

and

$$\sigma_0 = \frac{C_0(1-c)\omega_0 z^2 l^2 \gamma}{k} exp\left(\frac{\Delta S_h + \Delta S_c}{k}\right), \quad (2.11)$$

and the transport activation energy is given by

$$E_A = \Delta H_h + \Delta H_c. \quad (2.12)$$

For a full derivation, see Almond, Duncan, and West.[2]

The simplest circuit model of ionic conduction in solid state materials is a resistor in parallel with a capacitor, shown in Figure 2.4. In dielectric constant representation

$$\varepsilon = \varepsilon_s - \frac{j\varepsilon_s}{\omega\tau_0}, \quad (2.13)$$

where $\tau_0 = \varepsilon_0\varepsilon_s/\sigma_0$ and σ_0 is the direct current conductivity of the sample. The frequency dependant conductivity of the sample is given by

$$\sigma(\omega) = \sigma_0 + j\omega\varepsilon_s\varepsilon_0. \quad (2.14)$$

The dielectric constant as a function of frequency is shown in Figure 2.5. The imaginary part of the dielectric constant continually increases as frequency decreases, while the real part remains constant as a function of frequency. In the complex Z* plane, however, a semicircle is traced out as a decreasing function of frequency, as shown in Figure 2.6.

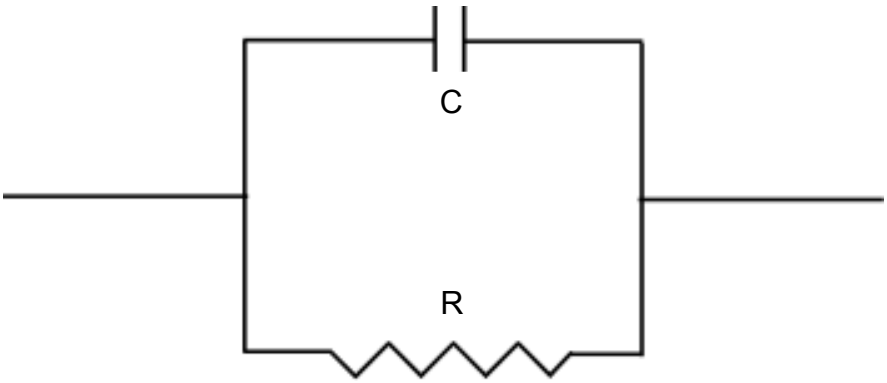

Figure 2.4. Circuit model used to describe ionic conduction in solid state materials.

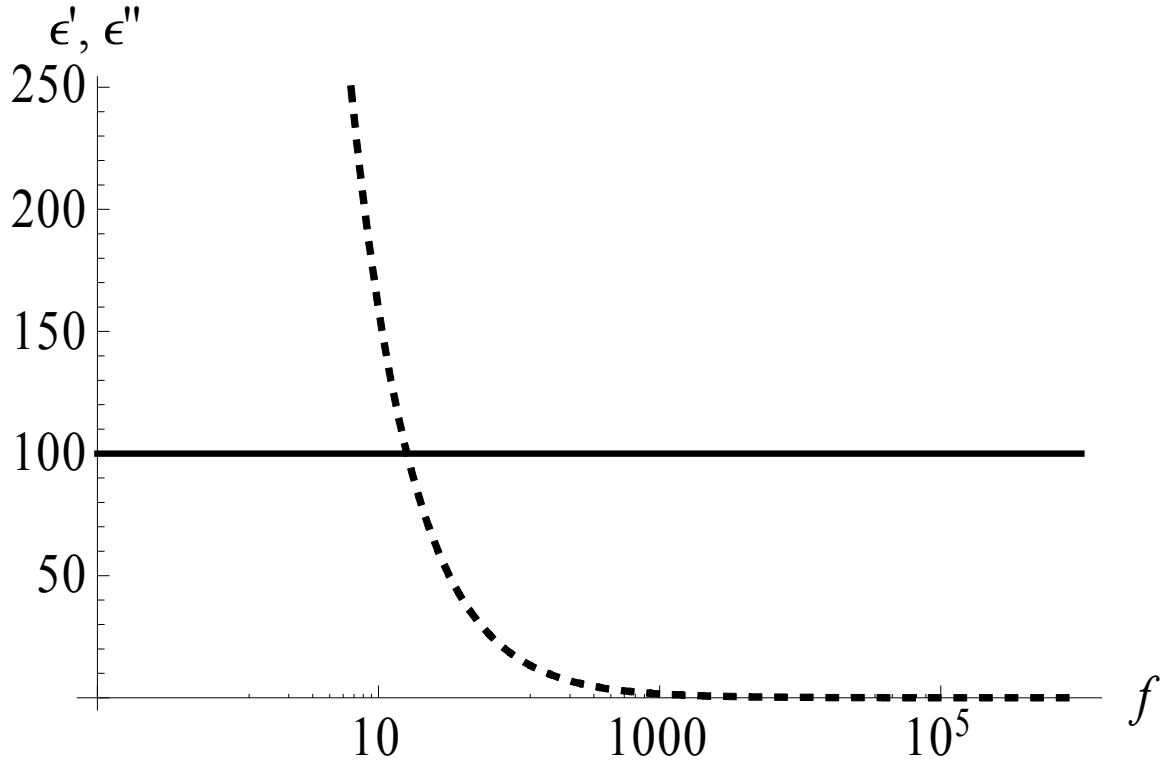

Figure 2.5. ε’ (solid) and ε” (dashed) as functions of frequency for circuit in Figure 2.4.

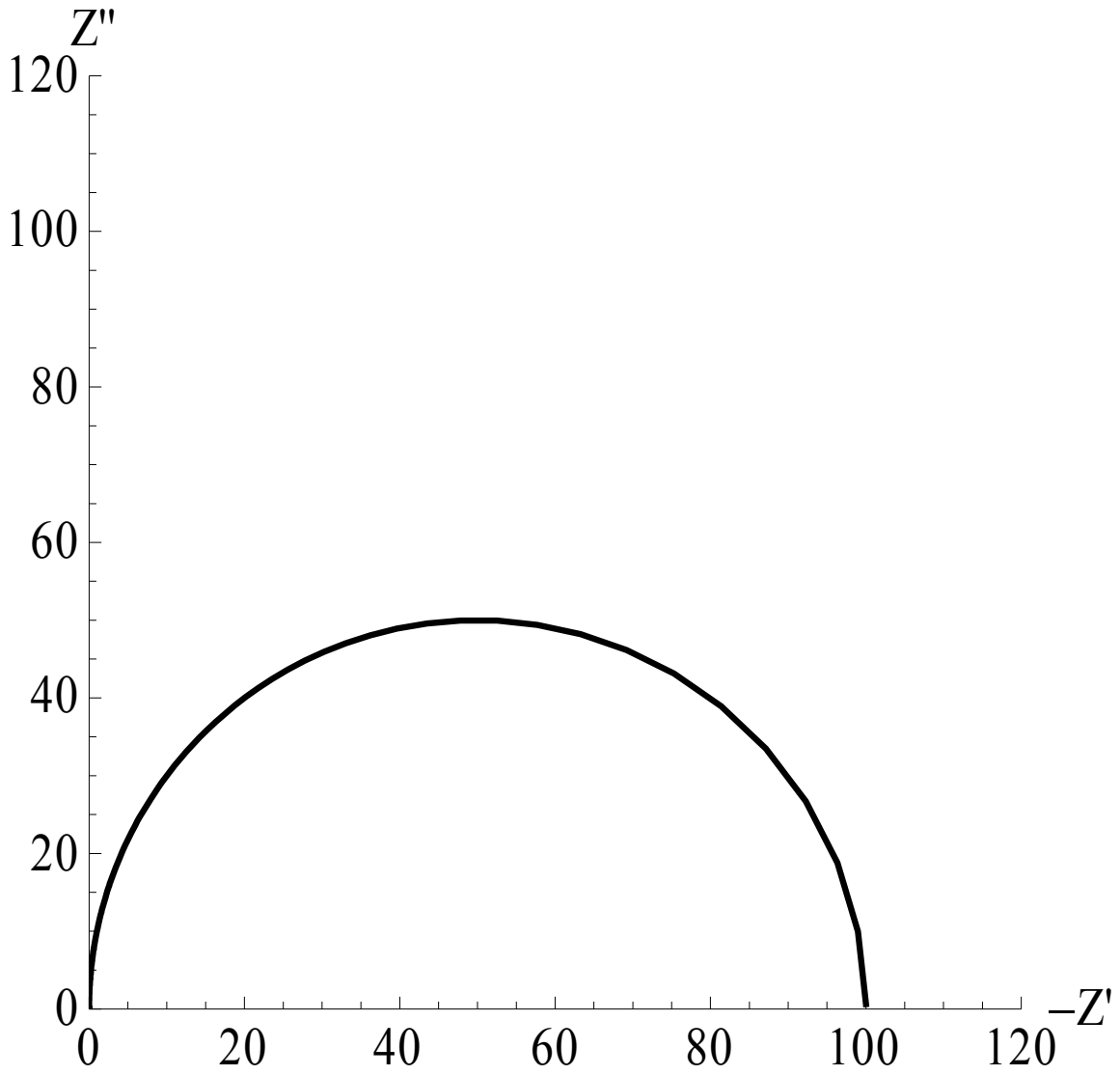

Figure 2.6. Impedance spectra of circuit shown in Figure 2.4.

2.2. Apparatus for Measuring Proton Conductivity

Two devices for measuring the proton conductivity of fully hydrated powder materials were sequentially constructed. Both devices were inspired by Holmberg's design with various modifications.[3] The first apparatus, shown in Figure 2.7, was designed for in situ measurement of sample thickness using a digital micrometer. Powder samples were loaded into an insulating plastic sample holder that was fitted with a platinum bottom contact. The plastic sample holder snuggly fit into the center of the brass block. Kapton thin film heaters, sandwiched between the internal brass block and the four attached cooling radiators, were used to heat the sample. Each attached cooling radiator had an inlet and outlet port for a cooling flow, if desired. The top contact was formed by a platinum plate connected to a hollow plastic rod. Electrical contact to the bottom contact was achieved through a BNC connector attached to a spring loaded tip that touched the platinum plate through a small hole in the bottom of the plastic sample holder. Electrical contact to the top contact was made by soldering a wire, running through the hollow plastic rod, to the platinum contact. The white block on the bottom of the apparatus was made from Teflon and electrically and thermally insulates the sample from the holder and external environment.

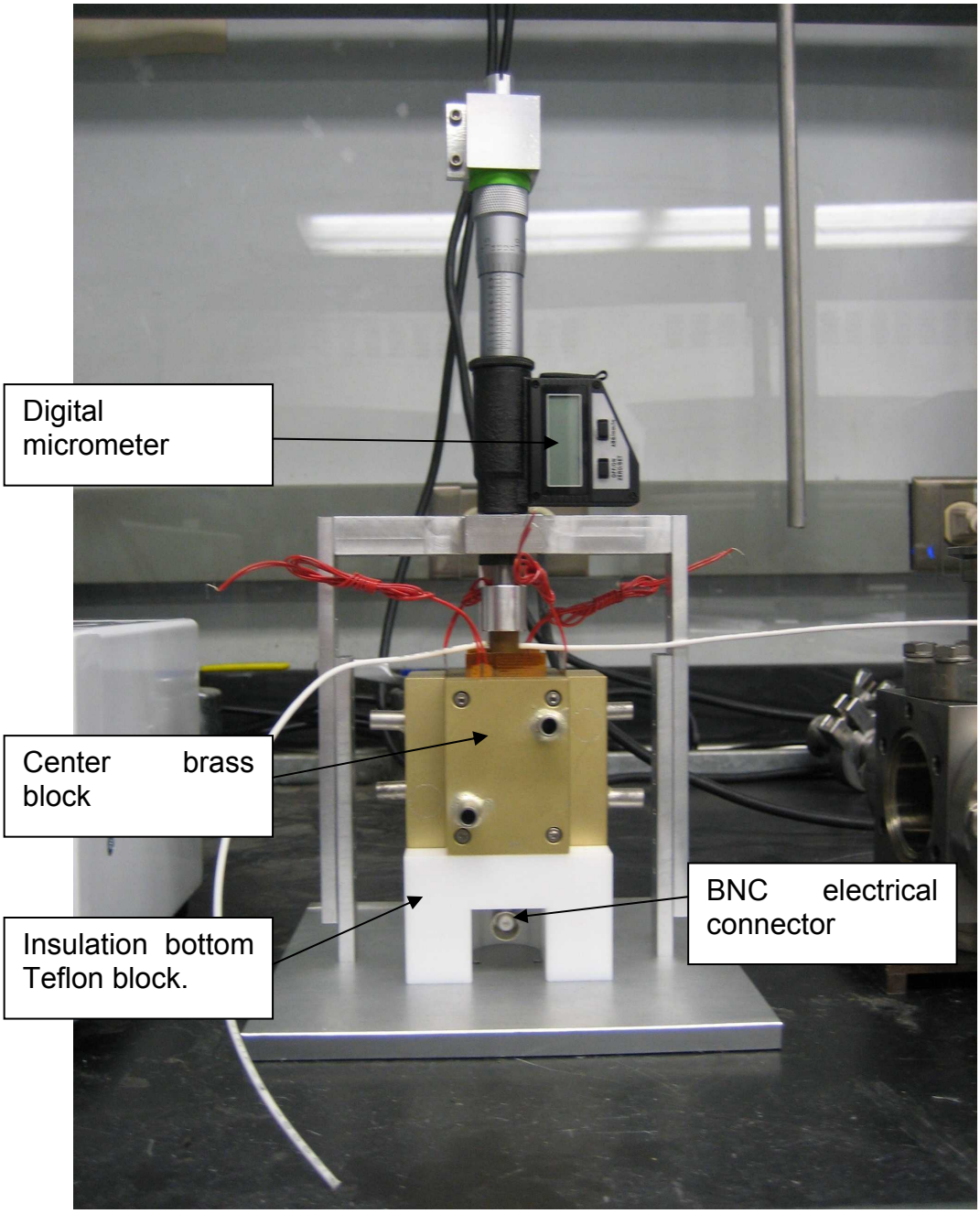

Figure 2.7. Apparatus constructed for variable temperature measurement of proton conductivity of fully hydrated powder samples, with in situ sample thickness measurement.

A Watlow temperature controller, connected to a k-type thermocouple inserted into a hold in the center brass block, was used to drive and control the Kapton thin film heaters. Pressure was applied to the powdered sample using a torque screwdriver to lower the micrometer piston onto the plastic probe through an aluminum adapter.

While this apparatus was designed to meet the current and future needs of the research effort, contact between the bottom platinum plate and small, spring-loaded probe was not reliable, and the top platinum plate did not stay attached to the plastic rod used to apply pressure to the sample. Further, upon heating above room temperature, complete hydration of the sample was lost, and the level of hydration was unknown. For these reasons, a simpler design was used in which the sample was not heated, and only measured at room temperature.

This second apparatus used the same aluminum frame and digital micrometer to apply force to and compress the sample and measure the sample thickness *in situ*. The sample holder was fabricated from Delrin plastic, and, like Holmberg's apparatus, had three chambers for simultaneous sample preparation. In this case, 4 mm x 5 mm platinum cylinders were used as top and bottom contacts. External contact with the bottom platinum cylinder was achieved with a piece of copper foil sandwiched between the platinum cylinder and plastic bottom of the apparatus, while electrical contact with the top platinum cylinder was achieved by coupling the platinum cylinder to a stainless steel rod of the same diameter with an axial set screw. A Teflon coupler was used between the

stainless steel rod and the piston of the digital micrometer to ensure electrical isolation of the sample. A picture is shown in Figure 2.8

Powdered samples were loaded into the sample holder on top of the bottom platinum cylinder and gently compressed. Distilled, purified water was then added and allowed to hydrate the sample for 60 minutes. This duration of time was experimentally found to be sufficiently long for the sample to reach equilibrium. The top platinum cylinder connected to the stainless steel rod was then inserted and pressure was applied using a torque screwdriver to lower the piston of the micrometer. A pressure of ~2000 psi was achieved.

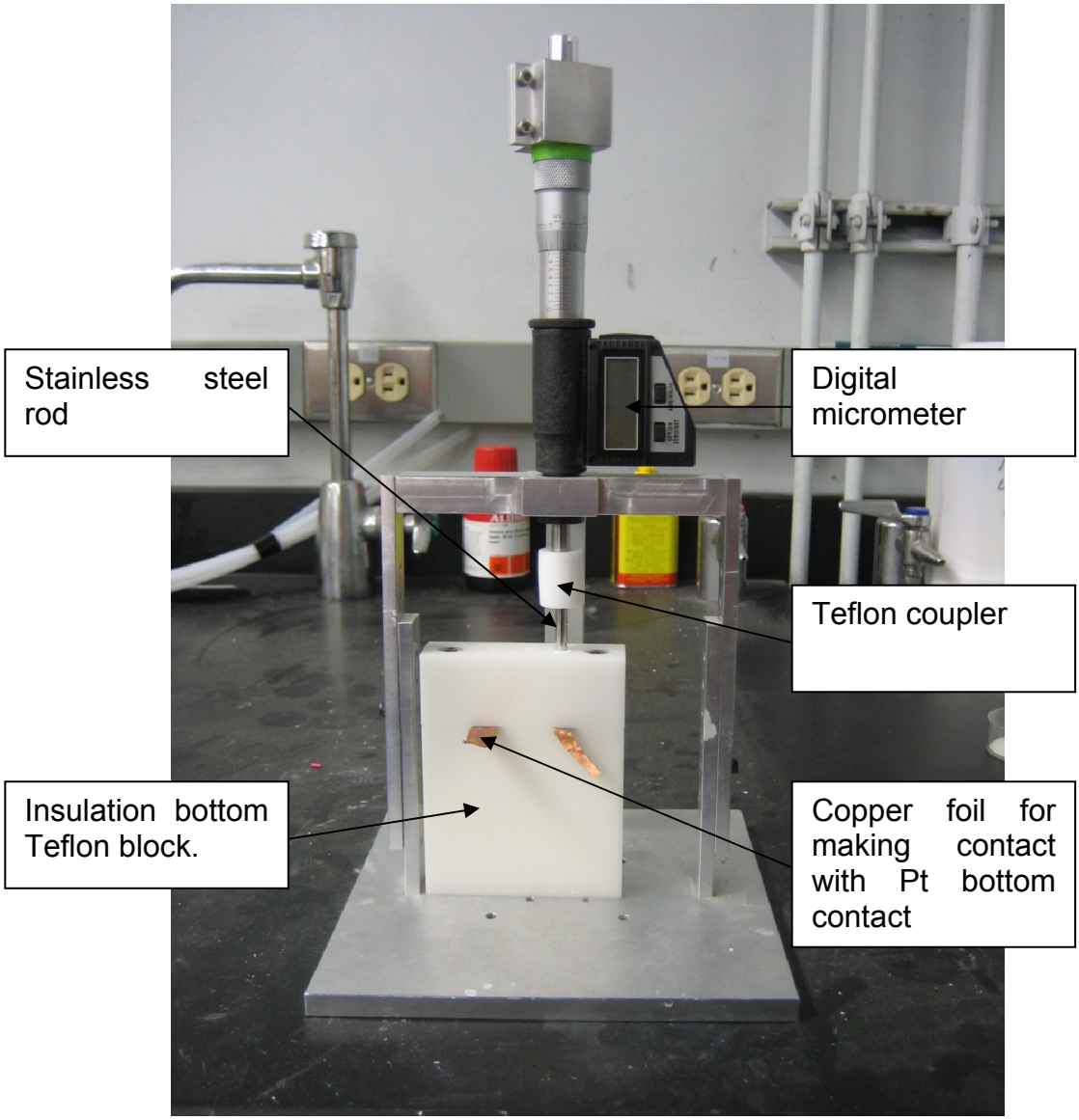

Figure 2.8. Apparatus for measuring proton conductivity of fully hydrated powders. Electrical contact is achieved by clipping Solartron 1260 cables to stainless steel rod and copper foil.

2.3. Apparatus for Variable Temperature/Humidity Measurements

Because our initial attempts to build an apparatus to measure proton conductivity as a function of temperature failed, a second device was constructed for this purpose. A few literature reports performed impedance spectroscopy to investigate the effect of hydration on conductivity (see Section 1.4.4.1.2, for example) in freestanding pelletized samples, and this avenue was, therefore, pursued. A Cincinnati Sub Zero temperature/humidity chamber was purchased to control both the temperature and relativity humidity of the sample environment. Another custom sample holder was constructed and is shown in Figure 2.9. The sample holder was designed for the simultaneous loading of sixteen samples and was constructed from Teflon.

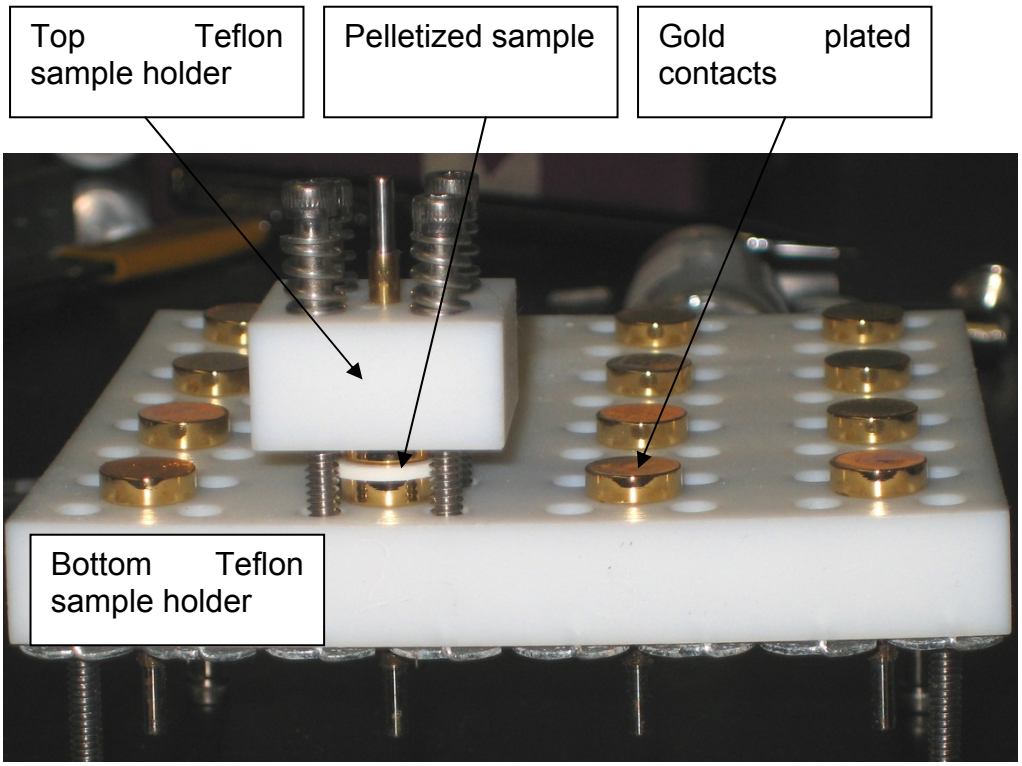

Figure 2.9. Sample holder for pelletized sample used in temperature/humidity chamber. A pellet can be seen between two of the gold coated contacts.

Gold coated, stainless steel electrodes were used to make contact with pelletized samples. Pressure was maintained during measurement by spring loaded screws that held the top Teflon blocks to the bottom Teflon plate, sandwiching the contacts and sample in between.

Pelletization of samples proved extremely difficult, particularly for hydrophobic samples, and achieving mechanically stable pellets without cracks and defects proved challenging. Once pellets were prepared, gold contacts were formed on pellet surfaces using shadow masks and thermal evaporation or sputtering. Pellets were then loaded into the sample holder which was hung in the temperature/humidity chamber. Electrical contact to each of the 32 electrodes was achieved by a high-temperature compatible coaxial cable running from inside the chamber, through a foam plug, out to the external laboratory environment. A Solartron 1260 was then manually connected to two of the coaxial cables, uniquely addressing an individual sample for measurement.

While this arrangement did allow for nearly simultaneous characterization of 16 samples in a temperature- and humidity-controlled environment, at elevated relative humidity and temperature, samples became mechanically unstable, and peeling of the gold contacts and loss of structural integrity was observed. While pellets did not often fall apart, impedance was not a stable function with time at a given temperature and relative humidity. The impedance of a representative sample over 3.5 days is shown in Figure 2.10.

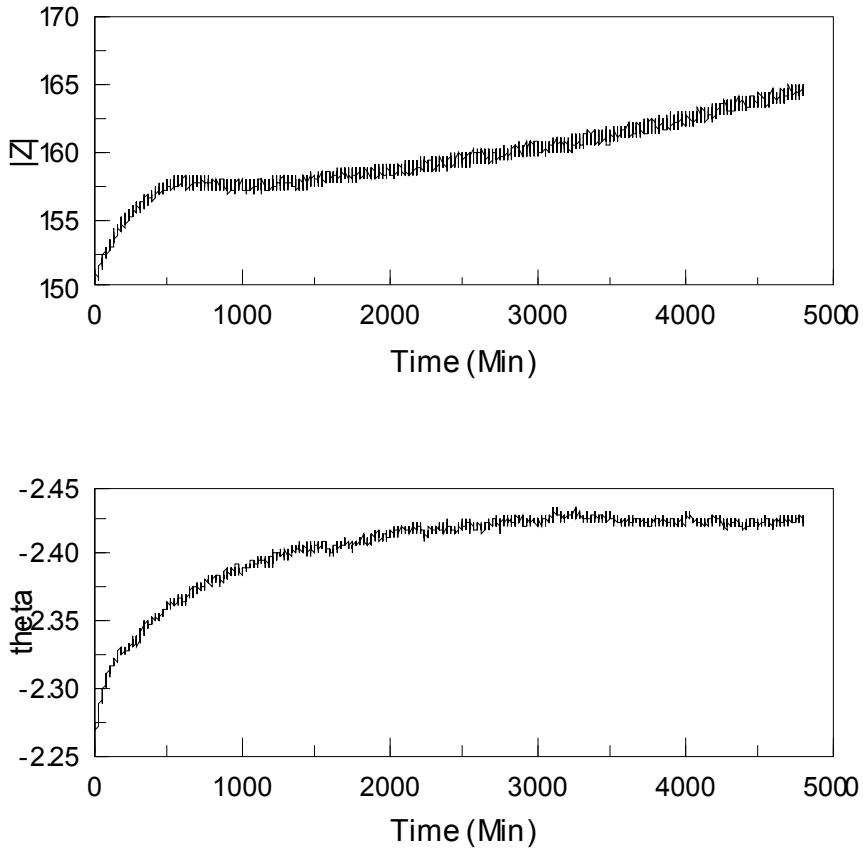

Figure 2.10. Impedance as a function of time at 65 °C and 95% relative humidity over 3.5 days.

2.4. Apparatus for Measuring Ion Conductivity

For measurement of ionic conductivity in microporous materials, all water must be removed from the pores as the presence of any water has been observed to significantly affect the conductivity. A vacuum system with a heater capably of elevating and controlling the sample temperature over the range 25-500 °C is, therefore, necessary to dehydrate samples and maintain a water-free environment for the duration of measurement. Furthermore, the sample holder must be capable of withstanding these temperatures. To meet these requirements a vacuum chamber and turbomolecular pump were purchased and a custom probe was constructed. The vacuum chamber is shown in Figure 2.11 and is capable of reaching vacuum levels of ~10^{-6} Torr. The sample holder is shown in Figure 2.12. A ceramic fiber heater (Watlow) is mounted inside the vacuum chamber to heat the sample. The inside bore is 3” and the outside pore of the sample holder is 2.5”, minimizing the vacuum space between the heater and sample and maximizing radiative heating. The heater temperature is adjusted and maintained by a Watlow temperature controller, using temperature data from a thermocouple mounted in the sample holder. The sample holder slides into the top of the vacuum chamber, down into the ceramic fiber heater.

Figure 2.11. Vacuum chamber used for dehydration and characterization of pelletized samples.

The sample holder began as a Novocontrol BDS1200, but was modified to achieve higher temperature operation. The lower half of the BDS1200 was replaced by a custom manufactured alumina holder with platinum electrodes and is shown in Figure 2.12. The alumina shielded thermocouple passes through the bottom alumina disc and approaches the bottom platinum contact from the bottom up. Electrical connection to the bottom contact is made by the indicated Pt wire which was attached by welding. A Pt wire running through the inside of an alumina tube wire welded to the Pt rod is used to contact the top of the sample. A sliding bushing (not visible) loads the visible spring to apply gentle force to the sample, through the Pt rod used to make electrical contact to the sample. A set screw holds the bushing vertically in place, keeping constant downward force on the spring. Connection to the top of the BDS is achieved using 3 mm gold plated banana connectors attached to the platinum wires from the top and bottom contacts. The BNC connectors of the BDS1200 then connect the sample to the frequency response analyzer (Solartron 1620 and Solartron 1296), through the aforementioned hardware. The alumina and platinum construction of the probe allow for high temperature, inert operation, without contamination from other metal sources, which was an issue when using the original BDS1200 sample holder. A second top contact was also constructed for the measurement of powdered samples and replaced the alumina tube with the Pt rod with a longer alumina tube having a flat, circular Pt plate on the bottom, mirroring the bottom contact shown in Figure 2.12 and producing a 1 cm diameter parallel plate capacitor structure. Powdered material was held in place by a quartz tube with an

internal diameter of 1 cm and pressure was applied using the described bushing and spring.

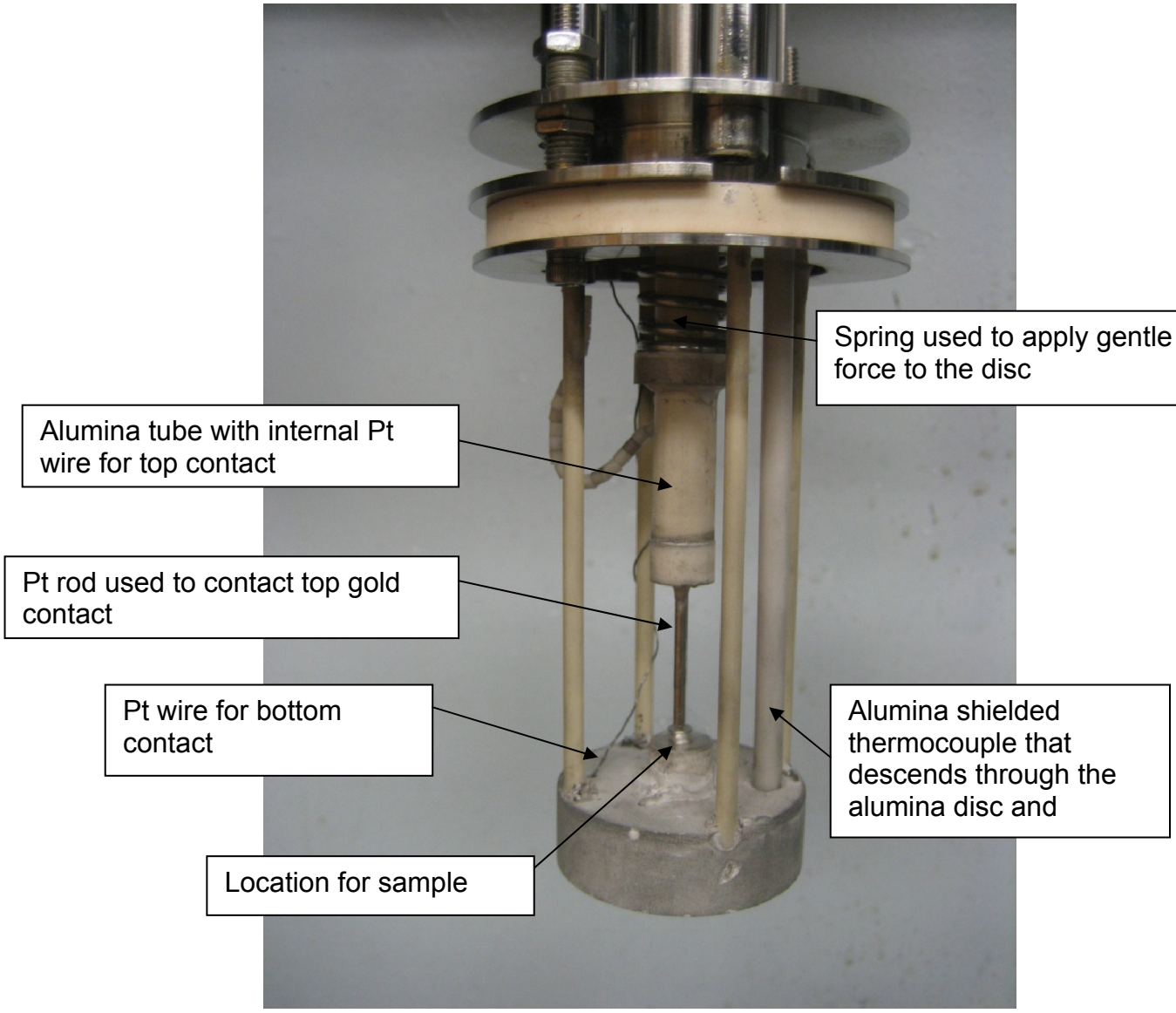

Figure 2.12. Sample holder for pelletized samples.

2.5. Measurement with Interdigitated Electrode Structures

Interdigitated electrode (IDE) structures, shown in Figure 2.13 were purchased from Novocontrol and used in an effort to help understand the features observed in modulus spectra of Na-X. Further discussion of this is presented in the following section. A vacuum system was constructed for characterization of the IDE chips and is shown in Figure 2.14. The IDE chips have three terminals, two used for characterization and the third for electrically grounding the guard ring on the chip. Watlow Firerod heaters in a copper block mounted inside the vacuum chamber (not shown) heat the IDE structure, which is held to the copper block by custom machined clips. Temperature is monitored and controlled by a Watlow temperature controller connected to a k-type thermocouple inserted into the copper block. Samples are prepared by slurrying Na-X in ethanol and applying a few drops of the slurry from a pipette onto the IDE structure. Vacuum was applied and samples were dehydrated at 250 °C under a low flow of argon. While a higher temperature was desirable, the IDE structures cannot survive higher temperatures.

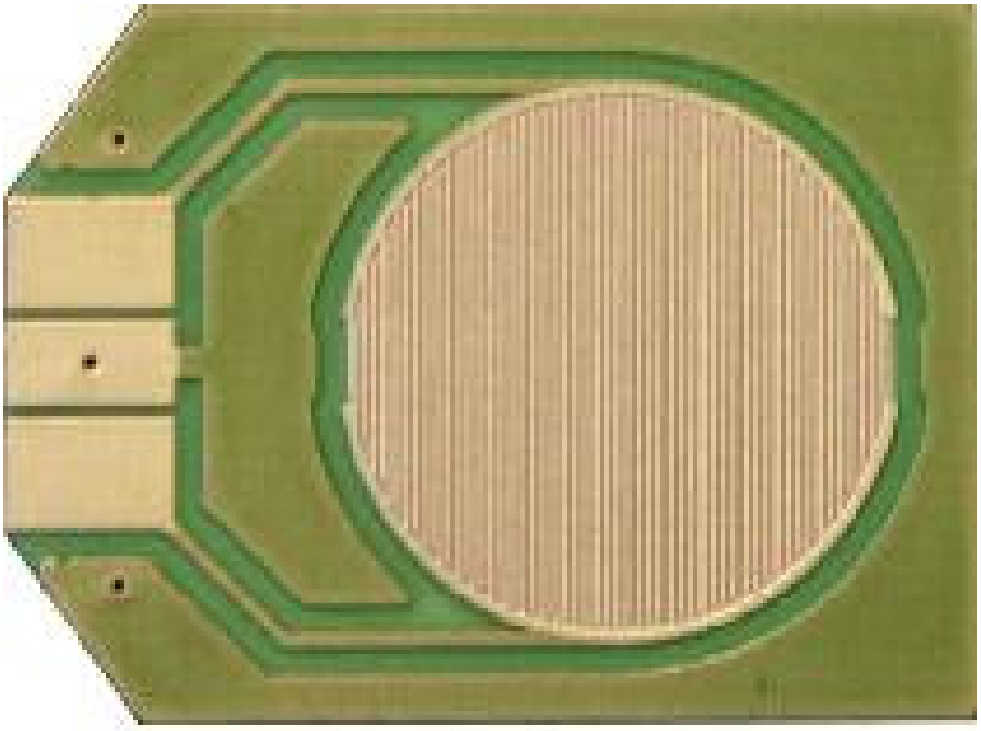

Figure 2.13. Interdigitated gold electrode structure purchased from Novocontrol.

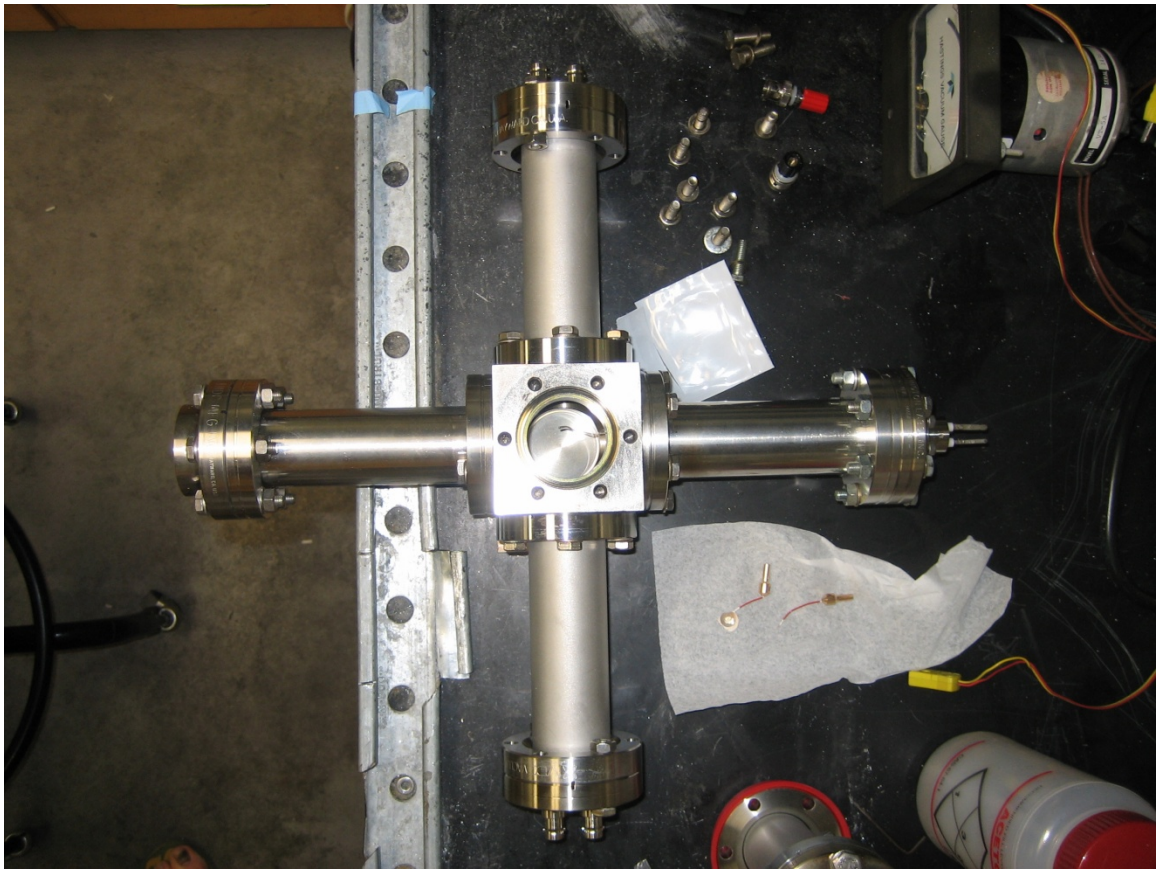

Figure 2.14. Vacuum chamber for characterizing IDE structures.

2.6. System Qualification and Analysis

In a series of papers on ionic motion in zeolites,[4-7] it was suggested the presentation of data in the modulus representation, Equation (2.15), and in particular the imaginary part of the modulus, M" as a function of frequency, rather than traditional impedance (Z*) data, allowed for more straightforward visualization of ionic conduction and local relaxations. In Equation (2.15) *i* is the square root of -1, ω is the frequency in radians per second, C_0 is the empty cell capacitance, M* is the complex modulus, and Z* is the complex impedance.

$$M^* = i\omega C_0 Z^* \tag{2.15}$$

A further article on ion conductivity in ETS-10 also uses modulus representation, and presents data on sodium exchanged zeolite X and ETS-10.[8]

In the investigation of ionic conductivity in VPI-9, it was of interest to first repeat literature results from the aforementioned papers on Na-X as a system check, but this was found this to be a non-straightforward process. Figure 2.15 shows M" data from a pressed pellet of Na-X with sputtered gold contacts, recorded at 303 K.

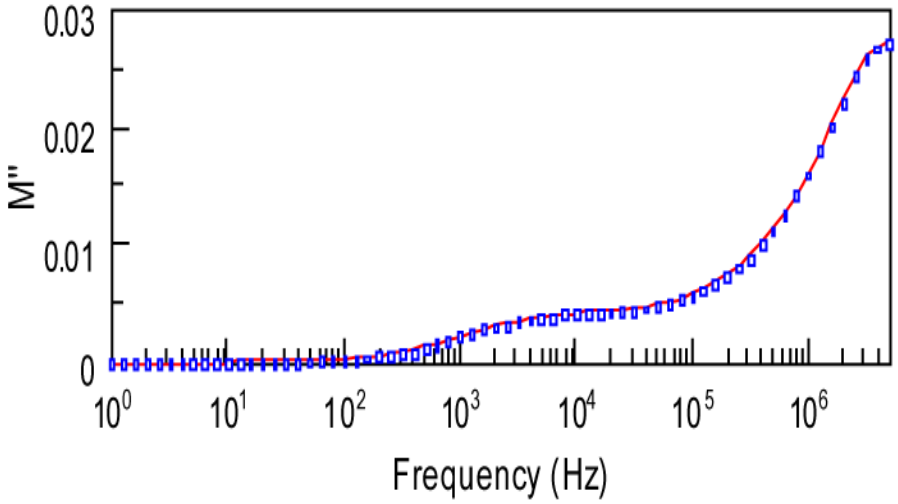

Figure 2.15. Imaginary part of the modulus as a function of frequency for a hydraulically pressed pellet of Na-X with sputtered gold contacts.

An intense peak at high frequency is clearly seen, which has been previously attributed to the local motion of a sodium ion within the large α cages in zeolite X.[7] The peak (or hump, rather) at low frequency, however is not well resolved from the large, high frequency peak, as in references 4 and 6. This was troubling at first, but further experimentation revealed the answer. Figure 2.16 shows M" spectra of Na-X powder, held between two platinum discs in vacuum, at various temperatures, and in this case two well resolved peaks are observed. The low frequency peak has been attributed to the long range ionic conduction process,[7] but the full interpretation is more complex, and will be discussed shortly. Finally, Figure 2.17 shows M" data for Na-X powder drop-cast from an ethanol slurry onto an interdigitated electrode (IE) structure (Novocontrol). The sample was dehydrated in vacuum to remove water and ethanol, and contributions to the spectra from the IE substrate have been subtracted. Again, two well resolved peaks are observed, with nearly equal peak heights. Pressed pellets of NaX without sputtered contacts were also characterized by directly sandwiching them between two Pt electrodes, and spectra similar to those show in Figure 2.16, but with less peak separation, were observed.

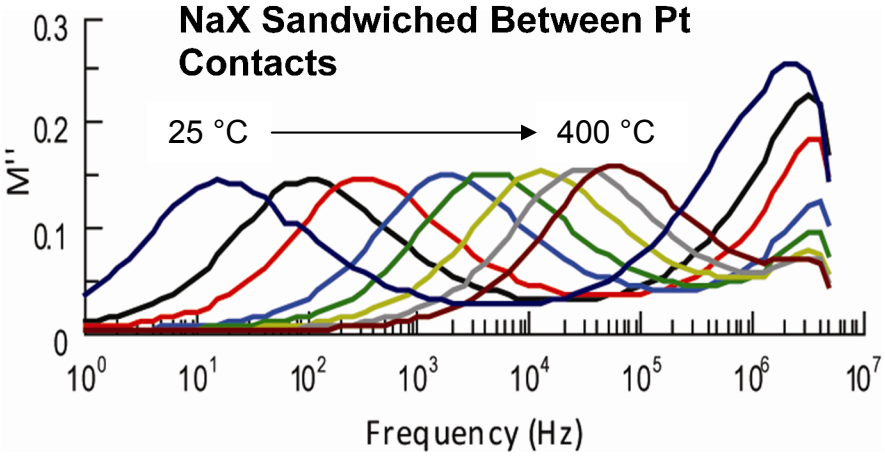

Figure 2.16. M" spectra of Na-X powder held between two circular Pt plates.

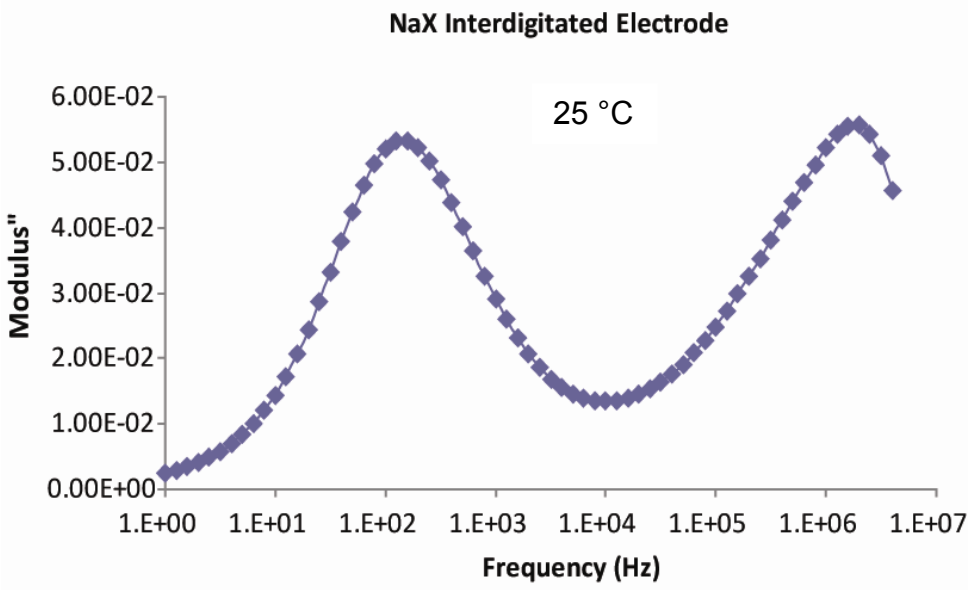

Figure 2.17. M" spectra for Na-X powder drop-cast from ethanol onto interdigitated electrode structure. Measurement performed in vacuum at 25 °C.

Circuit models are often used to describe the physical processes occurring in ionic conductors and the most common element is the parallel combination of a resistor and a capacitor. The M" spectra for Na-X can be modeled using two of these elements in series, one element corresponding to the motion of a sodium ion in an α cage and one to represent the long range process (such as DC conduction).[8]

To illustrate how circuit model parameter values (R_i and C_i) influence the fitting of data, and to help elucidate the nature of the variation in shape and position of the low frequency peak, Mathematica was used to plot M" as a function of frequency. This is shown in Figure 2.18, along with the circuit model used to generate the appropriate equations (by taking the Laplace transform of the appropriate transfer function). In the M" spectra, each RC parallel element corresponds to one of the peaks.

In Figure 2.18 a) and b) R2 and C2 are constant and correspond to the high-frequency peak. In a), however, a smaller value of C1 and larger value of R1 are used than in b). The peak position in frequency is controlled by the value R1, larger values of R1 shifting the peak to lower frequencies. The height of the peak is controlled by the value C1, smaller values of C1 increasing the peak height.

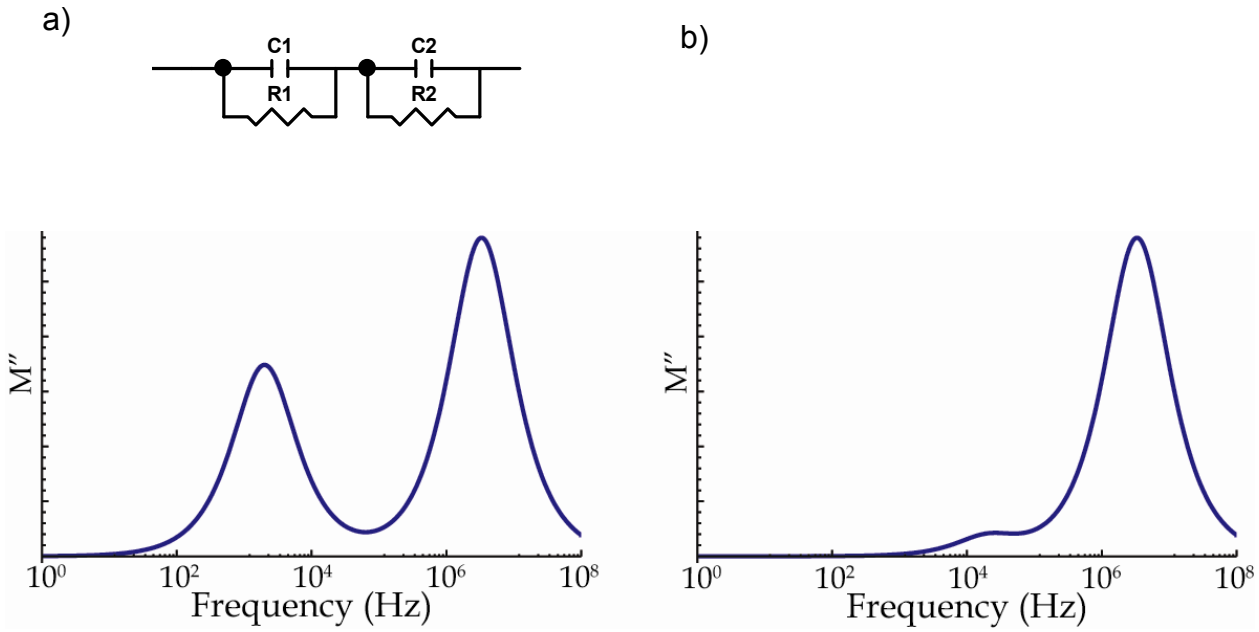

Figure 2.18. M" spectra calculated and plotted using Mathematica. Inset of a) is equivalent circuit model used to generate modulus plots.

Recall that the M” spectra for a pressed pellet with sputtered contacts looks like Figure 2.18b) while spectra of Na-X powder held between two Pt plates, Na-X powder drop cast onto IE electrodes, and pressed pellets of Na-X without sputtered electrodes more closely resemble Figure 2.18a). Poor interparticle contact, particularly in the non-hydraulically pressed powder samples and poor particle contact with the electrodes in all three latter cases significantly increase the value of R1, which can be thought of as an overall resistance of the sample (corresponding to long range ionic conductivity in the absence of these parasitic effects). The increase in R1 causes peak separation in frequency. In the latter three cases, C1, some overall capacitance, decreases with the addition of more series capacitors arising from an increase in space between particles and poor interfacial contact with the gold or platinum electrodes.

It should be noted that the high-frequency peak in Na-X samples appears at the same frequency for a give temperature for all methods of characterization, indicating true intragrain or intracage ion motion, as was previously suggested.[7]

While presenting data in M” representation is useful for over-emphasizing high frequency data and, therefore, studying internal processes that may occur very quickly, eliminating parasitic impedances by pressing pellets and forming intimate electrical contacts is more appropriate for extracting values of ionic conductivity from microporous and zeolite materials. (Nearly all reviewed literature on solid electrolytes reports on sintering powders and either painting on metallic contacts from Pt paste or using a physical vapor deposition technique to apply intimate metallic contacts.)

2.7. References

(1) *Impedance Spectroscopy: Theory, Experiment, and Applications*; Wiley, 2005.

(2) Almond, D. P.; Duncan, G. K.; West, A. R. *Solid State Ionics* **1983**, *8*, 159.

(3) Holmberg, B. A.; Yan, Y. *J. Electrochem. Soc.* **2006**, *153*, A146.

(4) Franke, M. E.; Simon, U. *Solid State Ionics* **1999**, *118*, 311.

(5) Franke, M. E.; Simon, U. *ChemPhysChem* **2004**, *5*, 465.

(6) Franke, M. E.; Simon, U.; Moos, R.; Knezevic, A.; Muller, R.; Plog, C. *Physical Chemistry Chemical Physics* **2003**, *5*, 5195.

(7) Simon, U.; Flesch, U. *J. Porous Mater.* **1999**, *6*, 33.

(8) Wei, T.-C.; Hillhouse, H. W. *J. Phys. Chem. B* **2006**, *110*, 13728.

3. Proton Conductivity in Sulfonic Acid-Functionalized Zeolite Beta: Effect of Hydroxyl Group

3.1. Abstract

The effect of hydroxyl group density on the proton conductivity in a model family of sulfonic-acid functionalized microporous materials with the *BEA framework topology is investigated. Nanocrystalline zeolite beta samples with a high concentration of hydroxyl groups are synthesized from tetraethylammonium hydroxide and aluminum containing gels and exhibit proton conductivity of ~5 x 10^{-3} S/cm. Pure silica zeolite beta with a nearly defect-free structure (low hydroxyl group density) is synthesized from tetraethylammonium fluoride containing gels and exhibits proton conductivity an order of magnitude lower, ~5 x 10^{-4} S/cm, than the samples with a high –OH density. Acetic acid at 80 and 135 °C is used to post synthetically "anneal" the framework of the zincosilicate zeolite beta analog, CIT-6, to produce pure silica materials with high and low concentrations of hydroxyl groups, respectively, to further confirm the effect of hydroxyl group density. CIT-6 treated at 80 °C (high –OH concentration) exhibits a proton conductivity of ~5 x 10^{-3} S/cm, while the proton conductivity of CIT-6 annealed at 135 °C (less defective framework and lower –OH density) is reduced to ~1 x 10^{-3} S/cm. In this family of sulfonic-acid containing materials it is, therefore, desirable to maximize the hydroxyl group density to best enhance the measured proton conductivity. This is presumably due to the formation of a more complete hydrogen-bonded water network inside the pores.

3.2. Introduction

Direct methanol fuel cells (DMFC's) and proton exchange membrane fuel cells (PEMFC's) have received considerable attention throughout the past decade because they are considered promising energy conversion devices for automobiles, homes and portable electronics. One of the critical components of these fuel cells is the proton conducting membrane electrically separating the anode from the cathode, and Nafion is the standard for new materials comparison. Nafion, while exhibiting excellent proton conductivity at low temperatures and high levels of hydration (~10^{-1} S/cm under conditions comparable to those used herein), has drawbacks including measurable methanol crossover and loss of hydration and proton conductivity at temperatures above 100°C. To address some of these issues, a number of reports suggest using various additives including metal oxides,[1-5] clays,[6] mesoporous materials[7-11] and zeolites.[12-15]

Among the oxide additives, acid functionalized mesoporous silicas and zeolites are advantageous because of their high acid strength (e.g., -SO_3H), adjustable acid group density, and the possibility to decrease methanol crossover and increase water retention at high temperature while allowing fast proton transport through the pore space. Acid functionalized mesoporous materials (by grafting or co-condensation) are used as solid catalysts, but only a few studies focus on their proton conducting properties.[9,10,16-22] Organically functionalized zeolite beta was first synthesized in our lab for catalysis applications nearly a decade ago.[23] Holmberg and co-workers investigated this solid as a potential

proton conducting material.[24] In their report, they synthesized zeolite beta containing phenethyl moieties from synthesis gels containing varying amounts of aluminum and suggested, after sulfonation of the phenyl ring, possible cooperativity between the negatively charged aluminum framework sites (counterbalanced by a proton or tightly bound tetraethyl ammonium ion, TEA^+) and the strong Bronsted acidity of the sulfonic acid in generating the observed proton conductivity, as the sample with the highest measured proton conductivity was crystallized from a synthesis gel having the lowest SiO_2/Al_2O_3 ratio (SiO_2/Al_2O_3 denoted here by X).

One goal of this study is to test the hypothesis of cooperativity between the sulfonic acid sites and the framework acid sites generated by framework aluminum by synthesizing molecular sieves with the *BEA framework that contained both sulfonic acid groups and varying concentrations of framework aluminum sites by either direct synthesis, as in the case of nanocrystalline beta, or by post synthetic insertion of aluminum in the hydroxyl nests left by the removal of framework zinc in CIT-6 (the zincosilicate analog to zeolite beta).[25] As shown below, framework aluminum is not maintained upon generation of the sulfonic acid sites. Instead of generating a series of samples with variable aluminum contents, the solids ended up being a series of samples that possess significantly different amounts of hydroxyl groups. Thus attention is paid to the effects of the hydroxyl group in the materials by choice of synthesis method and post synthesis ”annealing” of the framework silanols. Namely, sulfonic acid functionalized and unfunctionalized molecular sieves with the *BEA framework

topology (pure silica, ammonium, or proton exchanged) are prepared, and conductivity results are compared to sulfonic acid functionalized MCM-41. Furthermore, ammonium and proton exchanged nanocrystalline zeolite beta are investigated in an attempt to separate factors that contribute to the observed proton conduction, and to better design future materials.

3.3. Experimental

Tetraethylammonium hydroxide (35 wt%) (TEAOH), aluminum powder, fumed silica, zinc acetate dehydrate, Ludox© HS-40, pure silica MCM-41, and tetraethylammonium fluoride were purchased from Aldrich. Lithium hydroxide and tetraethylortho silicate (TEOS) were purchased from Fisher. Phenethyltrimethoxy silane (PETMS) was purchased from Gelest.

Nanocrystalline aluminosilicate (SiO_2/Al_2O_3 = x) zeolite beta was synthesized by a previously published procedure.[24,26] The final molar gel composition was 1.0 Al_2O_3:(*v**(1-*w*)) SiO_2:(*v***w*) PETMS:(0.26**v*+1) TEAOH:15**v* H_2O where *v* ranged from 50 to 1000, and w was 0 or 0.025 (2.5% Si coming from the PETMS). Half of the TEAOH was combined with the desired amount of aluminum powder. The other half of the TEAOH was combined with water and fumed silica. Both mixtures were stirred until all aluminum had dissolved. The mixtures were then combined and stirred with a Teflon coated stir bar for one hour. PETMS was then added, if desired, and the sample was stirred for one more hour. The gel was then loaded into Teflon lined stainless steel autoclaves (Parr). Typical crystallization parameters were 7 days at 140 °C with rotation at ~60 RPM. Crystallization products were collected by centrifugation, 1 hour at

50,000 g, and dried at 100 °C. PE containing samples (PE-BEA-x) were treated with 96 wt.% H_2SO_4 at 80 °C for 24 hours to remove the $TEA^+(OH^-)$. The extraction was repeated 2-3 times to ensure maximum removal of the structure directing agent (SDA). Following extraction, samples were dried at 110 °C under a rough vacuum and subsequently sulfonated by reaction with oleum for 12 hours at room temperature. See Figure 3.1. Oleum treated samples (S-PE-BEA-x) were quenched by addition to 500 mL of cold water followed by filtration and washing with at least 2 L of water. Samples were further washed by repeated sonication/centrifugation while monitoring the effluent pH. Samples were washed until the effluent pH was the same as the washing water (and until measured conductivity values did not change with subsequent washing). Non PE containing samples (BEA-x) were calcined at 550 °C in flowing air. The temperature was increased to 550 °C over 6 hours and then held at 550 °C for another 6 hours. Ammonium exchange was accomplished by contacting the samples with 1 M NH_4Cl at 90 °C for 24 hours. The supernatant was poured off and fresh solution was added 2-3 times to ensure maximum exchange. Samples were then collected by filtration, washed and dried at 100 °C. Thermal desorption of ammonia at 400 °C was used to produce proton exchanged samples.

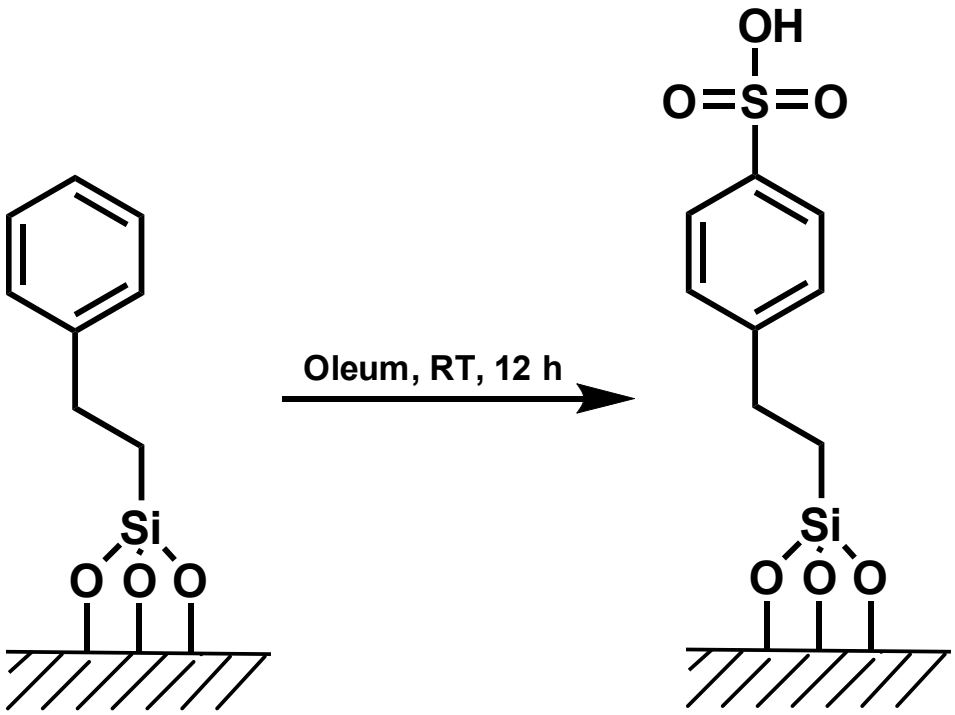

Figure 3.1. PETMS was incorporated into the pores of zeolite beta, or grafted onto the pore walls of MCM-41, and sulfonated using oleum.

Micrometer-sized pure silica beta (PS-BEA) was synthesized by dissolving the required amount of tetraethylammonium fluoride in water (6.25g TEAF/7.75 g water). Tetraethylorthosilicate and PETMS were then added and the initially 2-phase mixture was aggressively stirred for 12-24 hours. The resulting creamy white slurry was rotovaped to remove ethanol and excess water, and the appropriate amount of water was added back to the solution so that the final gel had a molar composition of 0.55 TEAF:*x* PETMS:(1-*x*) SiO_2 (TEOS): 7.25 H_2O. The thick gel was loaded into Teflon lined stainless steel autoclaves and heated, with rotation, in a convection oven to 140 °C. Crystallization time for non functionalized material was 5 days while phenethyl functionalized samples required 27 days[27,28]. Crystallization products were collected by filtration, washed with water and acetone, and dried at 100 °C. Aforementioned calcinations procedures were used to remove the SDA from non functionalized materials. PE functionalized materials were contacted with 1:1 (by volume) glacial acetic acid:water mixtures for 24 hours at 80 °C to remove occluded SDA molecules. The extraction procedure was repeated 2 to 3 times to ensure maximum removal of the SDA. The same procedure as described above was used to sulfonate the phenethyl groups.

CIT-6[25,29] and PE-CIT-6 were synthesized by dissolving lithium hydroxide and tetraethylammonium hydroxide in water. Zinc acetate dihydrate was then added and the mixture was stirred until all solids were dissolved. Dupont HS-40 silica was then added and the mixture was stirred for one hour. PTEMS was added and the mixture was stirred for another two hours. If no PETMS was

added, the mixture was stirred for a total of two hours. The final gel composition was 0.05 LiOH:0.65 TEAOH:0.03 $Zn(CH_3COOH)_2 \cdot 2H_2O$:*y* PETMS:(1-*y*) SiO_2:30 H_2O, where *y* was 0 or 0.025. The resulting clear liquid was loaded into Teflon lined stainless steel autoclaves and heated statically for 165 hours at 140 °C in a convection oven. Crystallization products were collected by filtration, washed with water and acetone, and dried at 100 °C. Non PE functionalized samples were calcined according to the aforementioned procedure. PE containing samples were extracted 2 to 3 times using the aforementioned acetic acid:water method. PE groups were sulfonated per the previously described method.

Phenethyl groups were grafted onto the surface of MCM-41 using the following procedure. MCM-41 (1 g) was dispersed into 100 mL toluene for 10 minutes with stirring. 4 mmol PETMS/g MCM-41 was added by syringe to the dispersion and the mixture was allowed to stir for 1 hour before the temperature of the oil bath was increased to 110 °C, causing the toluene to reflux. The grafting procedure was allowed to proceed for 24 hours. Grafted samples were collected by filtration and subsequently washed with 1 L of toluene (2 x 500 mL), 1 L of ethanol (2 x 500 mL), and 2 L of acetone (4 x 500 mL). The aforementioned oleum procedure was used to sulfonate the PE groups.

^{29}Si CPMAS and ^{13}C CPMAS NMR spectra were recorded using a Brucker Avance 200 MHz (^{1}H) spectrometer and 7 mm zirconia rotors. TGA data were collected using a Netzsch STA 449 C and Pt/Rh samples dishes. Powder X-ray diffraction patterns were obtained using a Scintag XDS 2000 with Cu k-α radiation.

The apparatus to measure proton conductivity consisted of a Delrin sample holder with 4 mm diameter sample wells and was discussed in Chapter 2. All samples were thoroughly washed and allowed to equilibrate with bulk water prior to measurement. Samples were compressed, after hydration with water, between two 4 mm diameter Pt cylinders using a torque screwdriver. A digital micrometer was connected to, but electrically isolated from, the Pt cylinders for *in situ* sample thickness measurement. Samples were compressed to 80 in-oz (~2000 psi) and held at this pressure for the duration of the measurement. A schematic of the sample holder is shown in Figure 3.2. Impedance spectroscopy was performed with a Solartron 1260 frequency response analyzer, and the conductivity calculated from the low frequency intersection of the semicircular arc with the real axis. At lower frequencies, a straight line routinely attributed to electrode polarization was observed (not shown). Attempts were made to characterize freestanding pellets with evaporated gold contacts in a controlled temperature-humidity chamber, but the pellets lost mechanical integrity at elevated temperatures and humidities, even when held between gold, platinum, or stainless steel plates.

Aluminum reinsertion into S-PE-CIT-6 extracted with acetic acid at 60 and 80 °C was attempted using $Al(NO_3)_3 \cdot 9H_2O$ according to a previously published procedure.[25]

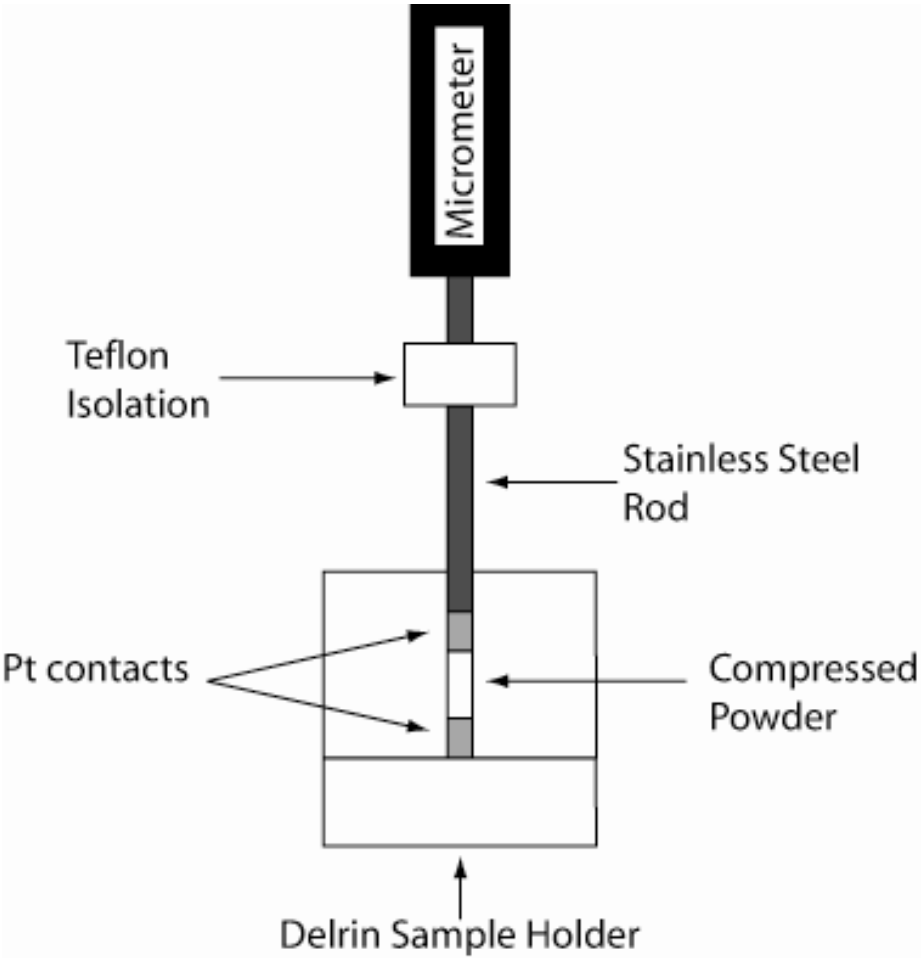

Figure 3.2. Sample holder used for proton conductivity measurements. Powder samples were loaded on top of the bottom Pt contact and allowed to equilibrate with water. The top contact was then inserted and the sample was compressed by applying torque to the micrometer with a torque screwdriver. An aluminum frame (not shown) held the structure in place, and the micrometer was zeroed before loading each sample.

3.4. Results and Discussion

Zeolite beta synthesized from gels containing tetraethylammonium hydroxide as the structure directing agent is known to have a high density of internal hydroxyl group nests,[26] and the removal of framework aluminum only increases this density. Similarly, when CIT-6 is treated with acetic acid at 80 °C, hydroxyl nests remain and the material is hydrophilic, but when treated with acetic acid at 135 °C the hydroxyl nests are annealed and the material becomes hydrophobic.[25] In contrast, pure silica zeolite beta crystallized from fluoride containing gels is known to possess many fewer hydroxyl defects[30] than the corresponding hydroxide-based synthesis product and is hydrophobic. For comparison, MCM-41 has many dangling hydroxyl groups and is hydrophilic. As shown and discussed below, the presence of hydroxyl groups is pivotal in achieving high proton conductivity, presumably due to the formation of a more complete hydrogen bonded water network in the materials with many dangling –OH, and better water saturation inside the molecular sieves.

Samples were characterized by powder X-ray diffraction (XRD) (Figure 3.3), thermogravimetric analysis (TGA) (Figure 3.4), ^{13}C CPMAS NMR Figure 3.5), and ^{29}Si CPMAS NMR (Figure 3.6). Silicon and aluminum contents were obtained by energy dispersive spectroscopy (EDS). To estimate acid loading, samples were titrated with 0.01 N NaOH followed by back titration with 0.01 N HCl.

From the EDS results shown in Table 3.1, it is observed that aluminum has been incorporated into as-made and calcined nanocrystalline beta samples

produced from aluminum containing gels (shown below for non-PE containing samples H-BEA-X and NH_4-BEA-X, but also true for PE containing samples prior to sulfuric acid treatment). While the SiO_2/Al_2O_3 ratio is greatly varied in the gels, a much narrower range is observed in the crystallized powders, and lower yields based on SiO_2 are observed with decreasing gel aluminum content. Treatment with sulfuric acid, however, removes aluminum from the framework, in addition to most of the TEA^+. Some residual TEA^+ exists, and may be bound to framework defects. Treatment of the zincosilicate CIT-6 with acetic acid removes framework zinc[25], and ^{27}Al MAS NMR indicates almost no reinsertion of aluminum into sulfonic acid functionalized CIT-6 (S-PE-CIT-6). We have yet to find a successful method for producing zeolite beta containing both organic sulfonic acids and framework aluminum (acid) sites.

Proton conductivities, sample and gel SiO_2/Al_2O_3, and acid loadings from TGA and titration are presented in Table 3.1 for the investigated samples. For comparison, the conductivity of as-made samples (containing ~20 wt % SDA) are presented in Table 3.2.

Acid site amounts from TGA and titration are in reasonable agreement and the acid density from sample to sample, and between synthesis methods, is consistent. Samples with many hydroxyl groups show slightly higher loading by titration than by TGA (S-PE-BEA-X, S-PE-CIT-6_80AA, S-PE-MCM-41) when compared to samples with fewer hydroxyl groups (S-PE-PS-BEA, S-PE-CIT-6_135AA), possibly due to deprotonation of some of the hydroxyl groups.

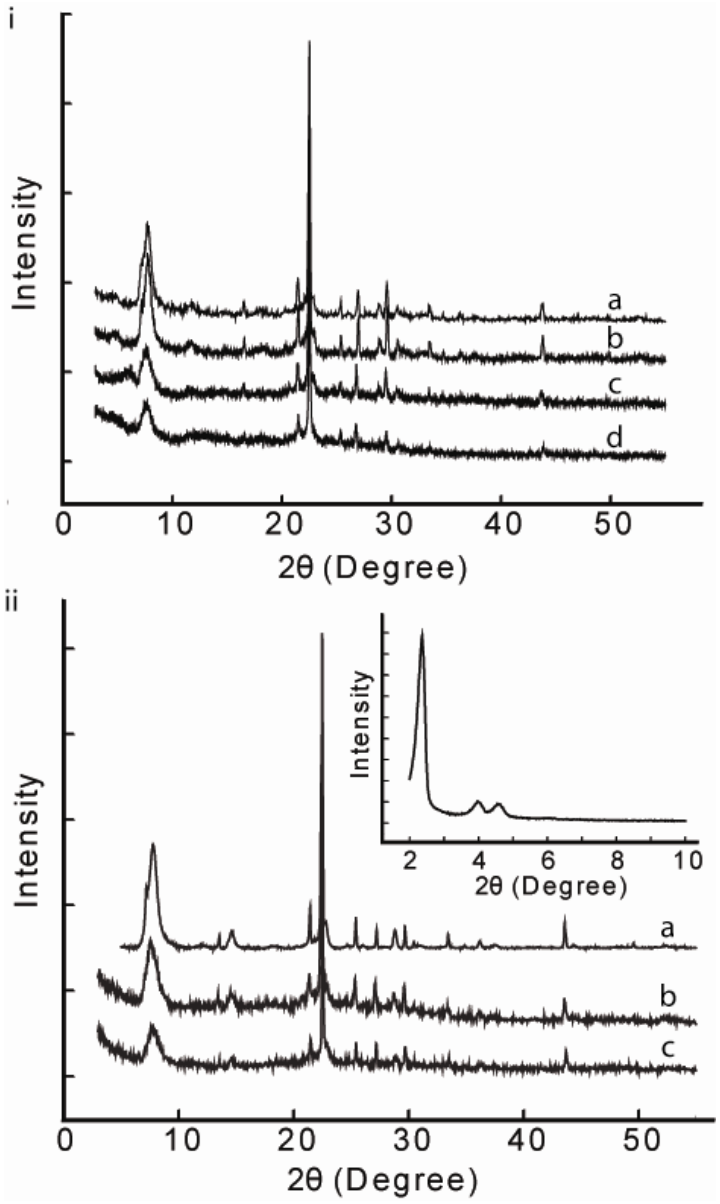

Figure 3.3. X-ray diffraction data from i) as-synthesized samples. a. Pure silica zeolite beta (PS-BEA), b. PE functionalized pure silica zeolite beta (PE-PS-BEA), c. PE-CIT-6, and d. PE-BEA-100 (PE functionalized nanocrystalline beta synthesized from a gel with a SiO_2/Al_2O_3 = 100). Ii) Sulfonated samples. a. S-PE-PS-BEA, b. S-PE-CIT-6, c. S-PE-BEA-100. Inset shows S-PE-MCM-41 (sulfonated, PE grafted MCM-41).

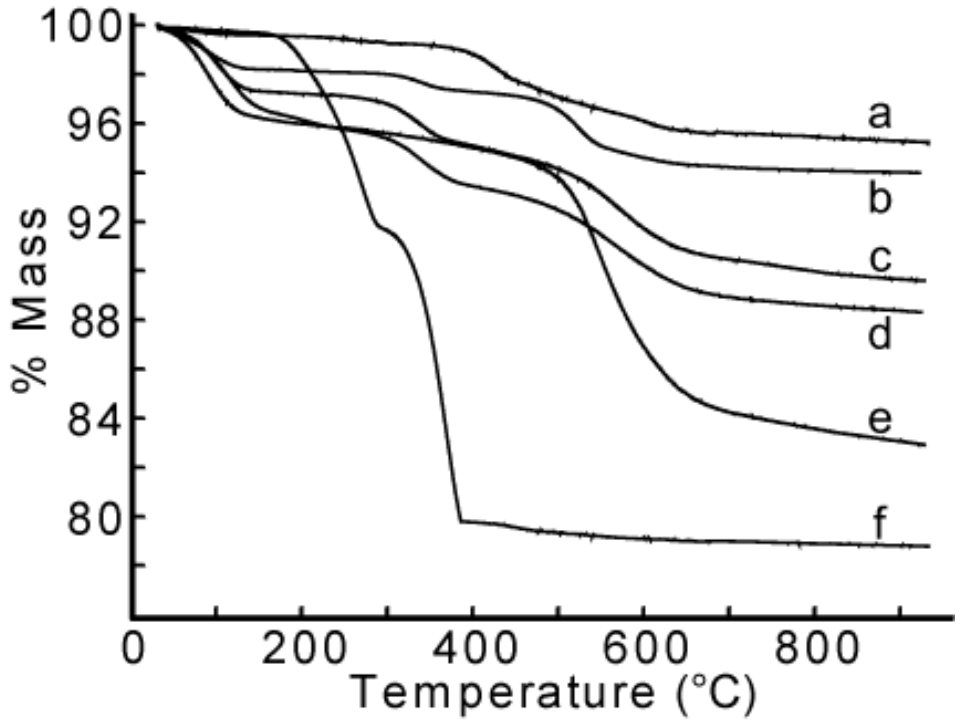

Figure 3.4. Thermogravimetric analysis traces of a. acetic acid extracted PE-PS-BEA, b. S-PE-PS-BEA, c. S-PE-CIT-6 (from 80 °C acetic acid extraction), d. S-PE-BEA-100, e. S-PE-MCM-41, f. as made PE-PS-BEA. Mass loss between 400 and 700 °C is attributed to combustion of the PE or S-PE groups. Mass loss under 200 °C is attributed to water and water bound to the sulfonic acid groups. The two mass losses in curve f are attributed to the combustion of TEAOH and TEA^+. A small amount of tightly bound TEA^+ is observed in curves b, c, and d.

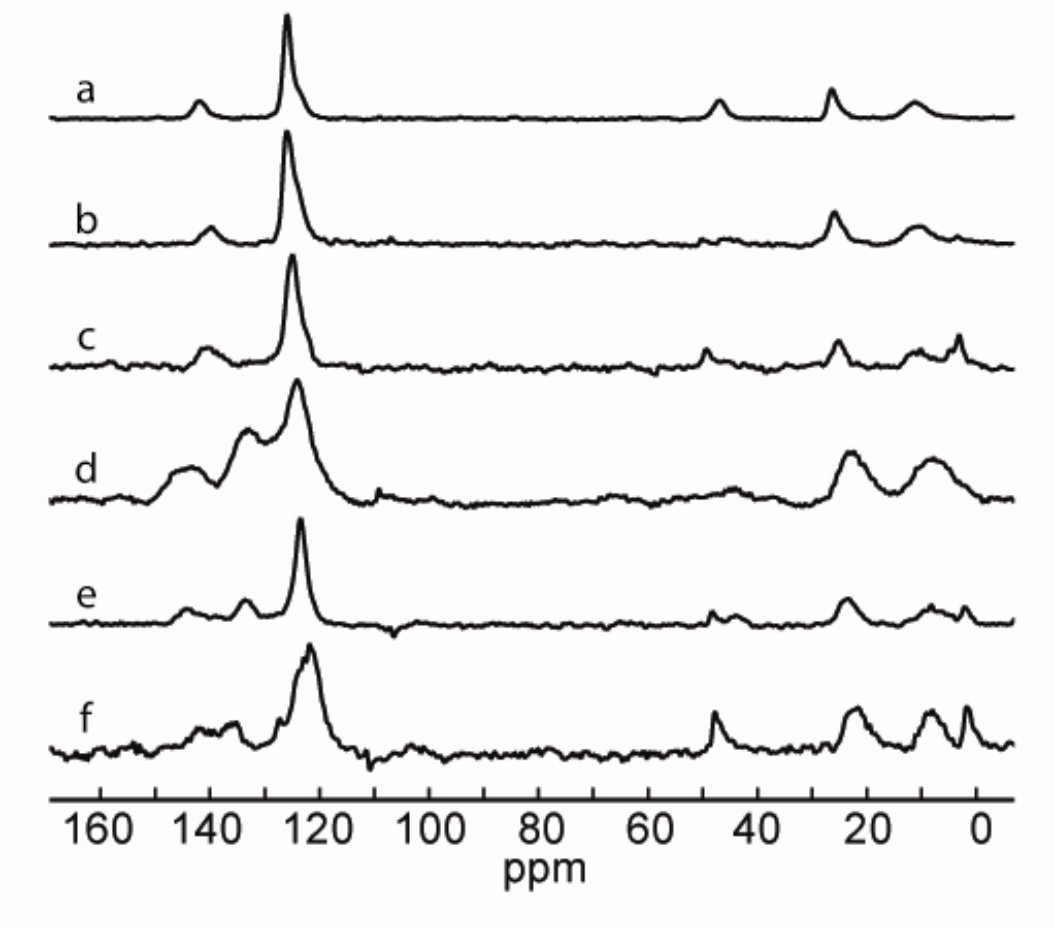

Figure 3.5. ^{13}C CPMAS NMR spectra of a. PE-MCM-41, b. acetic acid extracted PE-PS-BEA, c. acetic acid extracted (80 °C) PE-CIT-6, d. oleum treated (sulfonated) S-PE-MCM-41, e. oleum treated S-PE-PS-BEA, f. S-PE-CIT-6. Upon sulfonation, the aromatic peak at 140 ppm splits into two peaks at 133 and 145 ppm. The peak at 47 ppm in spectrum a is a spinning side band. Residual TEA^+ peaks are evident at 1 ppm and 48 ppm in spectra b, c, e, and f.

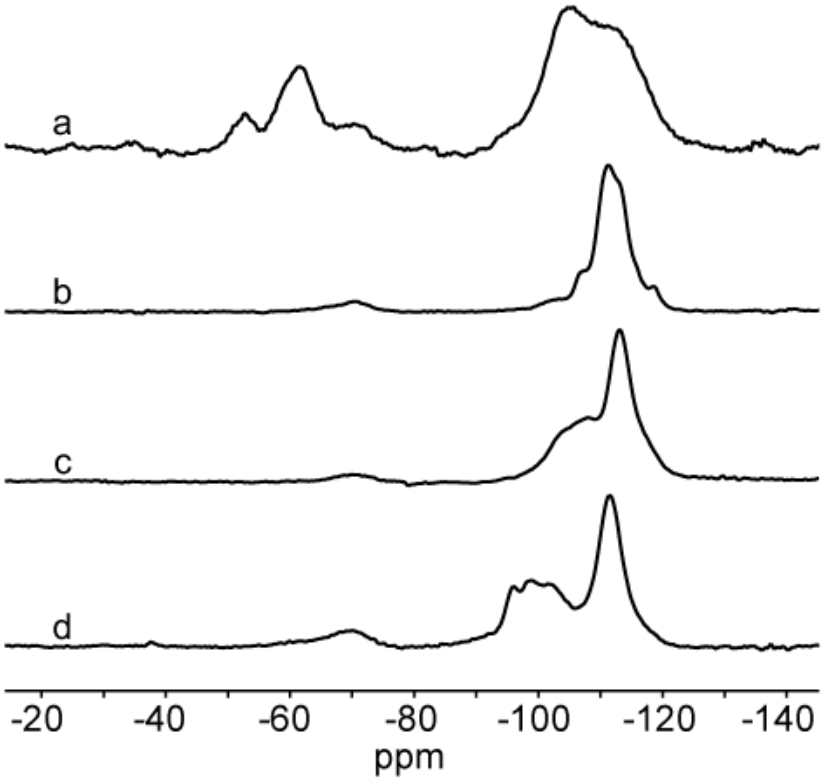

Figure 3.6. ^{29}Si CPMAS NMR spectra of a. PE-MCM-41, b. acetic acid extracted PE-PS-BEA, c. sulfuric acid extracted PE-BEA-100, and d. acetic acid extracted (80 °C) PE-CIT-6. T3 peaks are evident at -70 ppm in zeolite samples, while T3, T2, and T1 peaks appear in PE grafted MCM-41. Q peaks appear at more negative chemical shifts.

Table 3.1. Summary of sample characterization and proton conduction data.

Sample	σ (S/cm)	SiO_2/Al_2O_3 (EDS)	SiO_2/Al_2O_3 (rxn mixture)	TGA (mmol/g)	Titration (meq/g)
PS-BEA	8.8E-06	∞	∞	-	-0.003
O-PS-BEA	2.3E-05	∞	∞	-	0.0012
S-PE-PS-BEA	5.4E-04	∞	∞	0.17	0.18
BEA-50_80SA	1.1E-05	∞	50	-	-
BEA-400_80SA	6.4E-06	∞	400	-	-
BEA-1000_80SA	1.7E-05	∞	1000	-	-
NH_4-BEA-50	2.8E-03	30	50	-	-
NH_4-BEA-100	1.2E-03	73	100	-	-
NH_4-BEA-400	2.3E-03	69	400	-	-
NH_4-BEA-1000	1.2E-03	65	1000	-	-
H-BEA-50	7.0E-04	35	50	-	-
H-BEA-100	6.1E-04	75	100	-	-
H-BEA-400	4.8E-04	60	400	-	-
H-BEA-1000	3.1E-04	86	1000	-	-
S-PE-BEA-50	4.9E-03	∞	50	0.19	0.23
S-PE-BEA-100	6.7E-03	∞	100	0.24	0.30
S-PE-BEA-400	6.8E-03	∞	400	0.51	0.78
S-PE-BEA-1000	4.5E-03	∞	1000	0.23	0.24
S-PE-CIT-6_80AA	6.8E-03	∞*	33*	0.23	0.29
S-PE-CIT-6_135AA	1.2E-03	∞*	33*	0.24	0.23
MCM-41	2.9E-05	-	-	-	0.0055
O-MCM-41	1.5E-05	-	-	-	0.0052
S-PE-MCM-41	8.3E-03	-	-	0.59	0.87

∞* - for zincosilicate, dash line – not measured, ∞ – no Al detected, PS – pure-silica from fluoride synthesis, O – oleum treated, 80SA – extracted with 18 M H_2SO_4 at 80 °C, NH_4 – ammonium exchanged non-functionalized, H – proton exchanged non-functionalized, PE – Phenethyl functionalized, S – sulfonated with oleum, 80AA and 135AA –extracted with acetic acid at 80 and 135 °C

Table 3.2. Conductivity of as-made samples from gels with the indicated SiO_2/Al_2O_3 ratios. Typical SDA content is 20 wt%.

Sample Identity	Conductivity (RT/FH) (S/cm)
PE-PS-BEA	9.7E-05
PS-BEA	1.6E-04
BEA-50	1.9E-04
PE-BEA-50	1.7E-04
BEA-100	2.2E-04
PE-BEA-100	1.1E-04
BEA-400	1.8E-04
PE-BEA-400	4.8E-05

Examining the results in Table 3.1, unfunctionalized samples that do not contain aluminum in the framework (PS-BEA, O-PS-BEA, BEA-X_80SA, MCM-41, O-MCM-41) exhibit a conductivity of ~10^{-5} S/cm\ regardless of the hydrophilicity/hydrophobicity as no proton donating sites exist. Treatment of MCM-41 and PS-BEA with oleum does not significantly affect the measured conductivity, nor does the small amount of residual SDA, as sulfuric acid treated samples (BEA-X_80SA) exhibit conductivities similar to that of calcined PS-BEA. Zeolite beta samples containing tetrahedrally coordinated aluminum counterbalanced by a proton (H-BEA-X) exhibit conductivity ~$5*10^{-4}$ S/cm, and a slight trend of increasing conductivity with increasing aluminum content is observed as has been previously shown for ZSM-5.[31,32] Ammonium exchanged samples (NH_4-BEA-X) exhibit higher conductivity values (1-$2*10^{-3}$ S/cm) than those in the proton form in accordance with other reports using impedance spectroscopy[32] and NMR.[33] Direct current electrochemical[34] and NMR[33] results suggest that ammonium ions move by vehicular motion (chemical diffusion), and that hydrated ammonium exchanged zeolites should exhibit greater conductivity than hydrated, proton exchanged zeolites.[33]

The incorporation of phenyl sulfonic acid groups into hydrophilic nanocrystalline zeolite beta (S-PE-BEA-X) further increases the proton conductivity to ~$5*10^{-3}$ S/cm. Regardless of the aluminum content in the synthesis gel, no aluminum is detected by EDS in the sulfonated samples, and no significant difference in the measured conductivity values is observed among samples crystallized from synthesis gels containing differing amounts of

aluminum. In attempts to study cooperativity, however, it is observed that phenyl sulfonic acid-containing pure-silica beta (S-PE-PE-BEA, synthesized out of fluoride containing media) exhibits proton conductivity an order of magnitude lower than phenyl sulfonic acid-containing beta synthesized from TEAOH containing gels even when their acid loadings are similar. This may be due to the hydrophobicity/hydrophilicity of the pores, as the formation of a hydrogen bonded water network is important for fast proton hopping by the Grotthüss mechanism. Pores with many hydroxyl defects hold more water than defect-free pores, leading to a more “complete” hydrogen bonding network available for proton hopping. Results using phenyl sulfonic acid-containing CIT-6 further strengthen this hypothesis. S-PE-CIT-6 treated with acetic acid at 80 °C exhibits a proton conductivity similar to S-PE-BEA-X (X = 50, 100, 400, 1000). S-PE-CIT-6 from the same synthesis batch treated with acetic acid at 135 °C, however, shows conductivity a factor of 5 lower than the S-PE-BEA-X samples, and more closely resembles the conductivity of S-PE-PS-BEA. Additionally, phenyl sulfonic acid functionalized MCM-41 (S-PE-MCM-41) exhibits a conductivity value approximately that of S-PE-BEA-X. The acid loading by TGA and titration is slightly higher for S-PE-MCM-41, potentially leading to the slightly greater conductivity when compared to the S-PE-BEA-X samples.

3.5. Conclusion

In conclusion, it is shown that the incorporation of phenyl sulfonic acid groups into the pores of zeolite beta is more important for enhanced proton conductivity than framework alumina (in either the proton or ammonium

exchanged form) and that the conductivity observed in these samples does not arise from a cooperative effect between the bound organic sulfonic acid groups and the aluminum acid sites. Furthermore, the presence of framework hydroxyl groups is necessary for increasing the proton conductivity through the formation of a better hydrogen bonding water network in the pores leading to faster Grotthüss transport of the mobile protons.

3.6. References

(1) Watanabe, M.; Uchida, H.; Seki, Y.; Emori, M.; Stonehart, P. *J. Electrochem. Soc.* **1996**, *143*, 3847.

(2) Adjemian, K. T.; Lee, D. J.; Srinivasan, S.; Benziger, J.; Bocarsly, A. B. *J. Electrochem. Soc.* **2002**, *149*, A256.

(3) Ladewig, B. P.; Knott, R. B.; Hill, A. J.; Riches, J. D.; White, J. W.; Martin, D. J.; Costa, J. C. D. d.; Lu, G. Q. *Chem. Mater.* **2007**, *19*, 2372.

(4) Mauritz, K. A. *Mater. Sci. Eng., C* **1998**, *6*, 121.

(5) Shao, Z.-G.; Xu, H.; Li, M.; Hing, I.-M. *Solid State Ionics* **2006**, *177*, 779.

(6) Chang, J.-H.; Park, J. H.; Park, G.-G.; Kim, C.-S.; Park, O. O. *J. Power Sources* **2003**, *124*, 18.

(7) Baglio, V.; Di Blasi, A.; Arico, A. S.; Antonucci, V.; Antonucci, P. L.; Trakanprapai, C.; Esposito, V.; Licoccia, S.; Traversa, E. *J. Electrochem. Soc.* **2005**, *152*, A1373.

(8) Kim, H. J.; Lim, J. E.; Shul, Y. G.; Han, H. Mesoporous silica: Polymer composite membrane for direct methanol fuel cell. In *Recent Advances in the Science and Technology of Zeolites and Related Materials, Pts. A - C*, 2004; Vol. 154; pp 3036.

(9) Hogarth, W. H. J.; da Costa, J. C. D.; Drennan, J.; Lu, G. Q. *J. Mater. Chem.* **2005**, *15*, 754.

(10) Lin, Y.-F.; Yen, C.-Y.; Ma, C.-C. M.; Liao, S.-H.; Lee, C.-H.; Hsiao, Y.-H.; Lin, H.-P. *J. Power Sources* **2007**, *171*, 388.

(11) Pereira, F.; Valle, K.; Belleville, P.; Morin, A.; Lambert, S.; Sanchez, C. *Chem. Mater.* **2008**, *20*, 1710.

(12) Li, X.; Roberts, E. P. L.; Holmes, S. M.; Zholobenko, V. *Solid State Ionics* **2007**, *178*, 1248.

(13) Chen, Z. W.; Holmberg, B.; Li, W. Z.; Wang, X.; Deng, W. Q.; Munoz, R.; Yan, Y. S. *Chem. Mater.* **2006**, *18*, 5669.

(14) Libby, B.; Smyrl, W. H.; Cussler, E. L. *Electrochem. Solid-State Lett.* **2001**, *4*, A197.

(15) Libby, B.; Smyrl, W. H.; Cussler, E. L. *AIChE J.* **2003**, *49*, 991.

(16) Halla, J. D.; Mamak, M.; Williams, D. E.; Ozin, G. A. *Adv. Funct. Mater.* **2003**, *13*, 133.

(17) Marschall, R.; Bannat, I.; Caro, J.; Wark, M. *Microporous Mesoporous Mater.* **2007**, *99*, 190.

(18) Otomo, J.; Wang, S.; Takahashi, H.; Nagamoto, H. *J. Membr. Sci.* **2006**, *279*, 256.

(19) Alabi, C. A.; Davis, M. E. *Chem. Mater.* **2006**, *18*, 5634.

(20) Munakata, H.; Chiba, H.; Kanamura, K. *Solid State Ionics* **2005**, *176*, 2445.

(21) Mikhailenko, S.; Desplantier-Goscard, D.; Danumah, C.; Kaliaguine, S. *Microporous Mesoporous Mater.* **2002**, *52*, 29.

(22) Li, H.; Nogami, M. *Adv. Mater.* **2002**, *14*, 912.

(23) Jones, C. W.; Tsuji, K.; Davis, M. E. *Nature* **1998**, *393*, 52.

(24) Holmberg, B. A.; Hwang, S.-J.; Davis, M. E.; Yan, Y. *Microporous Mesoporous Mater.* **2005**, *80*, 347.

(25) Takewaki, T.; Beck, L. W.; Davis, M. E. *J. Phys. Chem. B* **1999**, *103*, 2674.

(26) Camblor, M. A.; Corma, A.; Mifsud, A.; Perez-Pariente, J.; Valencia, S. *Stud. Surf. Sci. Catal.* **1997**, *105*, 341.

(27) Jones, C. W.; Tsuji, K.; Davis, M. E. *Microporous Mesoporous Mater.* **1999**, *33*, 223.

(28) Camblor, M. A.; Corma, A.; Valencia, S. *Chem. Commun.* **1996**, 2365.

(29) Takewaki, T.; Beck, L. W.; Davis, M. E. *Top. Catal.* **1999**, *9*, 35.

(30) Camblor, M. A.; Corma, A.; Valencia, S. *Chem. Commun.* **1996**, 2365.

(31) Franke, M. E.; Simon, U. *Phys. Status Solidi B* **2000**, *218*, 287.

(32) Franke, M. E.; Simon, U. *ChemPhysChem* **2004**, *5*, 465.

(33) Afanassyev, I. S.; Moroz, N. K. *Solid State Ionics* **2003**, *160*, 125.

(34) Andersen, E. K.; Andersen, I. G. K.; Skou, E.; Yde-Andersen, S. *Solid State Ionics* **1986**, *18-19*, 1170.

4. Proton Conductivity of Acid Functionalized Zeolite beta, MCM-41 and MCM-48: Effect of Acid Strength

4.1. Abstract

Organically functionalized pure-silica zeolite beta, MCM-41, and MCM-48 samples containing phenyl sulfonic acid, propyl sulfonic acid, ethyl phosphoric acid, or ethyl carboxylic acid are prepared to test the effects of pore structure, pore dimensionality, and acid strength on proton conductivity. Four organic silanes are incorporated into pure-silica zeolite beta by direct synthesis, and grafted onto the surfaces of calcined MCM-41 and MCM-48. Post synthetic chemical reaction of the attached organic moieties creates acid functional groups and the resulting solid acids are investigated for their ability to transport protons. As may be expected, proton conductivity of the solid samples decreases with decreasing strength of the organic acid in solution. Acid functionalized pure-silica *BEA materials exhibit the lowest proton conductivities for each functionality when compared to MCM-41 and MCM-48 with the same organic functionality, and acid functionalized MCM-48 samples exhibited higher proton conductivity than the corresponding MCM-41 samples. Functionalized mesoporous materials are more conductive than similarly loaded pure-silica zeolite beta because of the presence of surface hydroxyls, and pure-silica nanocrystalline beta with a high density of surface hydroxyls exhibits nearly the same conductivity as similarly functionalized MCM-48.

4.2. Introduction

Direct methanol fuel cells (DMFCs) and hydrogen proton exchange membrane fuel cells (PEMFCs) are two types of fuel cells where commercial products have been developed, but have yet to find widespread deployment. While these devices are compact, easily refuelable, and operate at comparatively low temperatures, problems such as catalyst poisoning, methanol crossover, and water management exist and are current topics of research. One important component of both the DMFC and PEMFC is a protonically conducting but electronically insulating membrane placed between the anode and cathode. To minimize internal ohmic losses, the membrane must possess a high proton conductivity, and is commonly formed from Nafion or other perfluorosulfonic acid polymers. When fully hydrated, these polymers exhibit proton conductivities on the order of 10^{-1}-10^{-2} S/cm. For hydrogen PEMFC without active humidification, proton conductivity decreases rapidly with increasing temperature. For DMFC, membrane swelling allows methanol diffusion directly from anode to cathode decreasing cell efficiency.

To combat dehydration and methanol crossover, the addition of amorphous[1-4], mesostructured[5-9], and microporous silicas[10,11] to the perfluorosulfonic acid polymer has been suggested. Silica based micro- and mesoporous materials possess desirable traits including large internal surface areas, mechanically stable frameworks, chemical inertness, and negligible electronic conductivity. Furthermore, materials functionalized with organic sulfonic acids (through co-condensation or grafting) have shown proton

conductivities on the order of Nafion.[7,8,12-16] While a few reports address the use of sulfonic acid functionalized mesoporous materials and zeolites,[11,17] and a non-porous organic carboxylic acid-containing silicate[18] for fuel cell applications, no reports are found on phosphoric and carboxylic acid containing zeolites or mesoporous materials for use in fuel cell membranes. Further, there is little information on how the pore structure (i.e., pore size and dimensionality) may influence proton transport under conditions of similar acid loading. Here, zeolite beta, MCM-41, and MCM-48 samples are compared to address the effects of acid strength, pore size, and dimensionality on proton conductivity.

Organically functionalized zeolite beta (denoted BEA), MCM-41, and MCM-48 containing phenyl sulfonic acid, propyl sulfonic acid, ethyl phosphoric acid, or ethyl carboxylic acid were prepared to test the effects of pore structure and acid strength on proton conductivity. Four organic silanes are incorporated into pure-silica zeolite beta by direct synthesis, and grafted onto the surfaces of calcined MCM-41 and MCM-48. The attached organic moieties are then converted into acid functional groups and the resulting solid acids are investigated for their ability to transport protons.

4.3. Experimental

Tetraethylammonium fluoride (TEAF), cetyl trimethylammonium bromide (CTAB), 30 wt% hydrogen peroxide in water, and MCM-41 were purchased from Aldrich. The organic silanes, phenethyltrimethoxy silane (PETMS), mercaptopropyltrimethoxy silane (MPTMS), diethylphosphatoethyltriethoxy silane (DEPTES), and 2-(carbomethoxy)ethyltrichloro silane (CMETCS), were

purchased from Gelest. Potassium hydroxide was purchased from Fischer Scientific.

Pure-silica beta was synthesized by dissolving the required amount of tetraethylammonium fluoride in water (6.25 g TEAF/7.75 g water). Tetraethylorthosilicate and the organic silane were then added and the initially 2-phase mixture was aggressively stirred for 12-24 hours. The resulting creamy white slurry was rotovaped to remove excess water, and the appropriate amount of water was added back to the solution so that the final gel had a molar ratio of 0.55 TEAF: *x* Organic Silane:(1-*x*) SiO_2: 7.25 H_2O. x = 0.028 was used in the preparation of all zeolite beta samples for this work, even though it appears from TGA and titration that some samples have higher or lower loading in the crystalline products. Previous experience in the group has shown that attempts to incorporate higher organic loadings lead to less than 100% crystalline products. The thick gel was loaded into Teflon-lined stainless steel autoclaves and heated, with rotation, in a convection oven to 140 °C. Crystallization times for non functionalized material was 5 days while phenethyl functionalized samples required 27 days[19,20] Crystallization times for Mercaptopropyl, diethylphosphatoethyl, and 2-(carbomethoxy)ethyl required approximately 50 days. Crystallization products were collected by filtration, washed with water and acetone, and dried at 100 °C. Non-functionalized materials were calcined in flowing air at 550 °C for six hours to remove the tetraethylammonium structure directing agent (SDA). Organically functionalized materials were contacted with 1:1 (by volume) glacial acetic acid:water mixtures for 24 hours at 80 °C to

remove occluded SDA molecules. The extraction procedure was repeated 2-3 times to ensure maximum removal of the SDA. To sulfonate PE functionalized samples, ~1 g of PE-BEA was dried at 110 °C under rough vacuum and contacted with ~25 g of oleum (fuming sulfuric acid) for 12 hours at room temperature. The mixture was quenched by addition to 500 mL of cold water and samples were further washed with at least 2 L of water (4 x 500 mL). Mercaptopropyl functionalized samples were oxidized to propylsulfonic acids by contacting ~1 g of MP-BEA with ~25 g of 30 wt.% for 12 hours at room temperature. The mixtures were then filtered and dried at 100 °C and the resulting powders were acidified with 1 M H_2SO_4 for 2 hours at room temperature. Diethylphosphatoethyl groups were cleaved and converted to phosphonic acid groups by refluxing ~1 g of diethylphosphatoethyl functionalized beta in ~25 g of concentrated hydrochloric acid for 24 hours. Samples were quenched in 500 mL of cold water and washed with at least 2 L of additional water (4 x 500 mL). Finally, 2-(carbomethoxy)ethyl groups were converted to carboxylic acids by stirring ~1 g of 2-(carbomethoxy)ethyl functionalized material in 1 N hydrochloric acid for 24 hours. The powder was then filtered and rinsed with at least 2 L of water (4 x 500 mL). Acid functionalities are shown in Figure 4.1.

MCM-48 was synthesized according to a published procedure.[21] Tetraethylorthosilicate, potassium hydroxide, and water were combined in a Teflon jar and stirred for 10 minutes. Cetyl trimethylammonium bromide (CTAB) was then added and the mixture was stirred for an additional 10 minutes before

loading into a Teflon lined stainless steel autoclave. The final molar gel composition was 1 SiO_2:1 KOH:62 H_2O:0.65 CTAB. After statically heating at 115 °C for 48 hours, the crystallization products were collected by filtration, washed with 500 mL of water and 500 mL of acetone, and dried at 100 °C. CTAB was removed from the pores of MCM-48 by calcination at 550 °C in flowing air.

Organic silanes were grafted onto the surfaces of MCM-41 and MCM-48 using the following procedure. Approximately 1 g of powder was dispersed into 100 mL toluene for 10 minutes with stirring. 0.30 mmol organic silane/g MCM-41(8) was added by syringe to the dispersion, and the mixture was allowed to stir for 1 hour before the temperature of the oil bath was increased to 120 °C, causing the toluene to reflux. Higher loadings were also prepared during this investigation by using up to 4 mmol organic silane/g MCM-41(8). The grafting procedure was allowed to proceed for 24 hours. Grafted samples were collected by filtration and subsequently washed with 1 L of toluene (2 x 500 mL), 1 L of ethanol (2 x 500 mL), and 2 L of acetone (4 x 500 mL). The aforementioned post treatments were used to functionalize or modify the attached organic moieties shown in Figure 4.1.

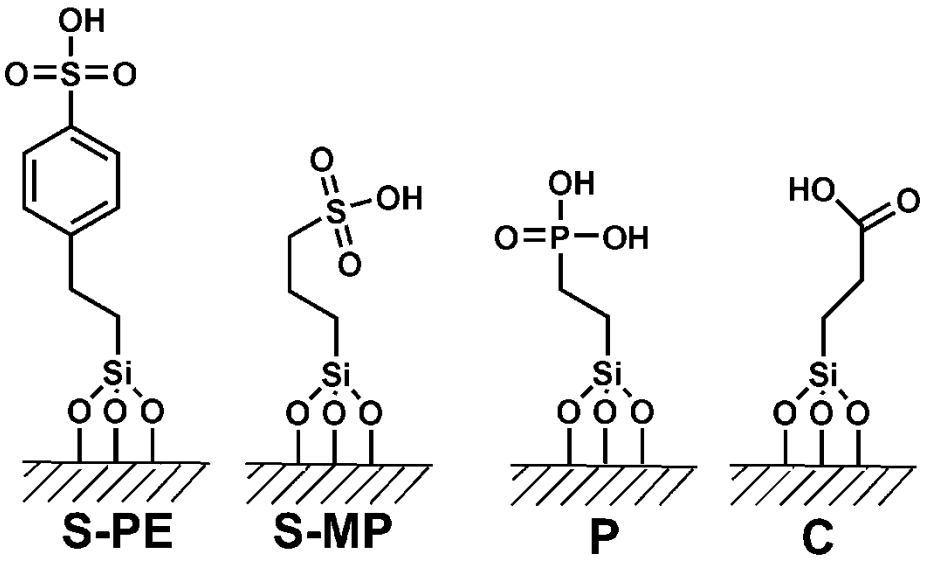

Figure 4.1. Illustration of the acid groups incorporated into zeolite beta, MCM-41, and MCM-48.

Attempts to synthesize hydrophilic, nanocrystalline zeolite beta (possibly a better comparison to MCM-41 and MCM-48 as they are also hydrophilic, containing many hydroxyls) containing mercaptopropyltrimethoxy silane, diethylphosphatoethyltriethoxy silane, or 2-(carbomethoxy)ethyltrichloro silane, led to crystallization without any incorporated organic. This difficulty may arise from the crystallization kinetics associated with the use of TEAF versus TEAOH. Synthesis of pure silica BEA containing phenethyltrimethoxy silane requires approximately 27 days, while mercapto propyltrimethoxy silane, diethylphosphatoethyltriethoxy silane, or 2-(carbomethoxy)ethyltrichloro silane require nearly twice that time in comparison to the much shorter crystallization times required for nanocrystalline (PE and non-PE containing), 5 days.

^{29}Si CPMAS and ^{13}C CPMAS NMR spectra were recorded using a Brucker Avance 200 MHz (^{1}H) spectrometer and 7 mm zirconia rotors, unless otherwise noted. TGA data were collected using a Netzsch STA 449 C and Pt/Rh samples dishes. Powder X-ray diffraction patterns were collected using a Scintag XDS 2000 with Cu k-α radiation.

Prior to proton conductivity measurements samples were ground with a mortar and pestle and further washed with water by repeated sonication/centrifugation while monitoring the effluent pH. Samples were washed until the effluent pH was the same as the washing water (and until measured conductivity values did not change with subsequent washing).

The apparatus for measuring proton conductivity consisted of a Delrin sample holder with 4 mm diameter sample wells and was discussed in Chapter

2. Samples were compressed, after equilibration with bulk water for 1-2 hours, between two 4 mm diameter Pt cylinders using a torque screwdriver. Other reports[16,17,22,23], and trial and error suggest equilibration with bulk water (added, by pipette, on top of the uncompressed powder in the sample holder) occurs in less than an hour. A digital micrometer was connected to, but electrically isolated from, the Pt cylinders for *in situ* sample thickness measurement. Samples were compressed for the duration of the measurement by applying a torque of 80 in-oz to the micrometer screw. A schematic of the sample holder is shown in Figure 3.2. A Solartron 1260 analyzer was used to scan a 100 mV ac voltage[16,23] over the frequency range 1 Hz to 5 MHz. Reported values are averages from 2 to 3 measurements.

4.4. Results and Discussion

Powder X-ray diffraction verifies crystalline products with the *BEA framework topology, MCM-41 pore structure and MCM-48 pore structure (Figure 4.1). ^{29}Si CPMAS NMR data confirm the silicon-carbon connectivity between the organic groups and inorganic structure (Figure 4.3). T3 peaks are visible in BEA samples, while T3, T2, and T1 resonances are observed in the grafted MCM-41 and MCM-48 materials indicating successful attachment of organic silanes. ^{13}C CPMAS NMR spectra (Figure 4.4) were used to verify the presence of the incorporated organic group, with the exception of the phosphoric acid containing materials. ^{31}P CP MAS NMR spectra for the phosphoric acid containing materials are shown in Figure 4.5. Thermogravimetric analysis (TGA) is used to estimate the organic loading in each material, and representative TGA traces are shown in

Figure 4.6. TGA loadings are corroborated by acid titration (samples contacted with excess 0.01 N NaOH followed by back titration with 0.01 N HCl). Fourier transform-infrared spectroscopy (FTIR) further verifies post-grafting chemical modification to produce phosphonic and carboxylic acids (Figure 4.7). Representative impedance data are shown in Figure 4.8.

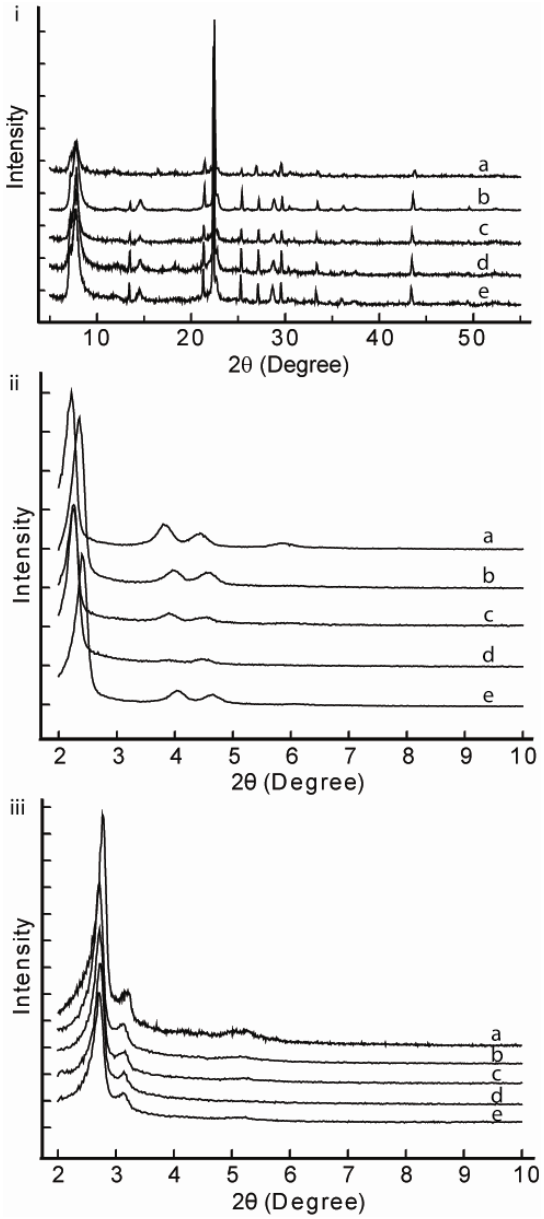

Figure 4.2. X-ray data of i) pure-silica zeolite beta (BEA) containing a. no organic silane (but uncalcined), b. sulfonated phenethyl groups (S-PE-BEA), c. oxidized mercaptopropyl groups (S-MP-BEA), d. cleaved diethylphosphatoethyl groups (P-BEA), and e. cleaved 2-(carbomethoxy)ethyl groups. ii) a. MCM-41, b. S-PE-MCM-41, c. S-MP-MCM-41, d. P-MCM-41, e. C-MCM-41. iii) a. MCM-48, b. S-PE-MCM-48, c. S-MP-MCM-48, d. P-MCM-48, e. C-MCM-48.

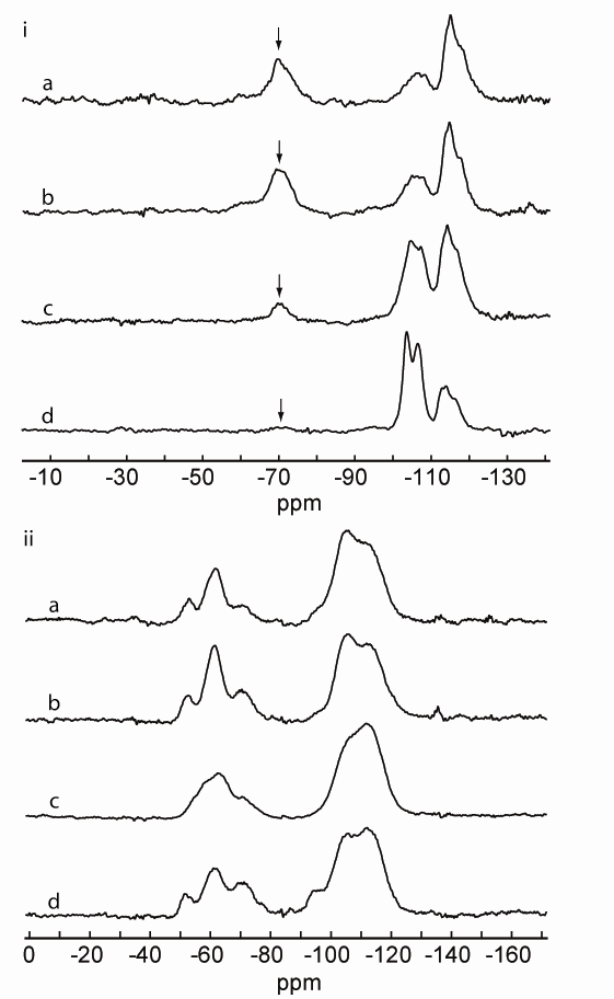

Figure 4.3. ^{29}Si CPMAS NMR spectra of i) acetic acid extracted pure-silica beta samples as follows: a. PE-BEA, b. MP-BEA, c. P-BEA, d. C-BEA. The T3 resonance centered at -70 ppm is indicative of a C-Si-$(OSi)_3$ bond. ii) grafted MCM-41 samples as follows: a. PE-MCM-41, b. MP-MCM-41, c. P-MCM-41, d. C-MCM-41. T1, T2, and T3 resonances are clearly seen near -50 ppm, -60 ppm, and -70 ppm, respectively, indicative of C-Si$(OH_{(3-x)})Si_x$ where *x* is from T*x*. Spectra of functionalized MCM-48 samples gave spectra similar to those shown in ii.

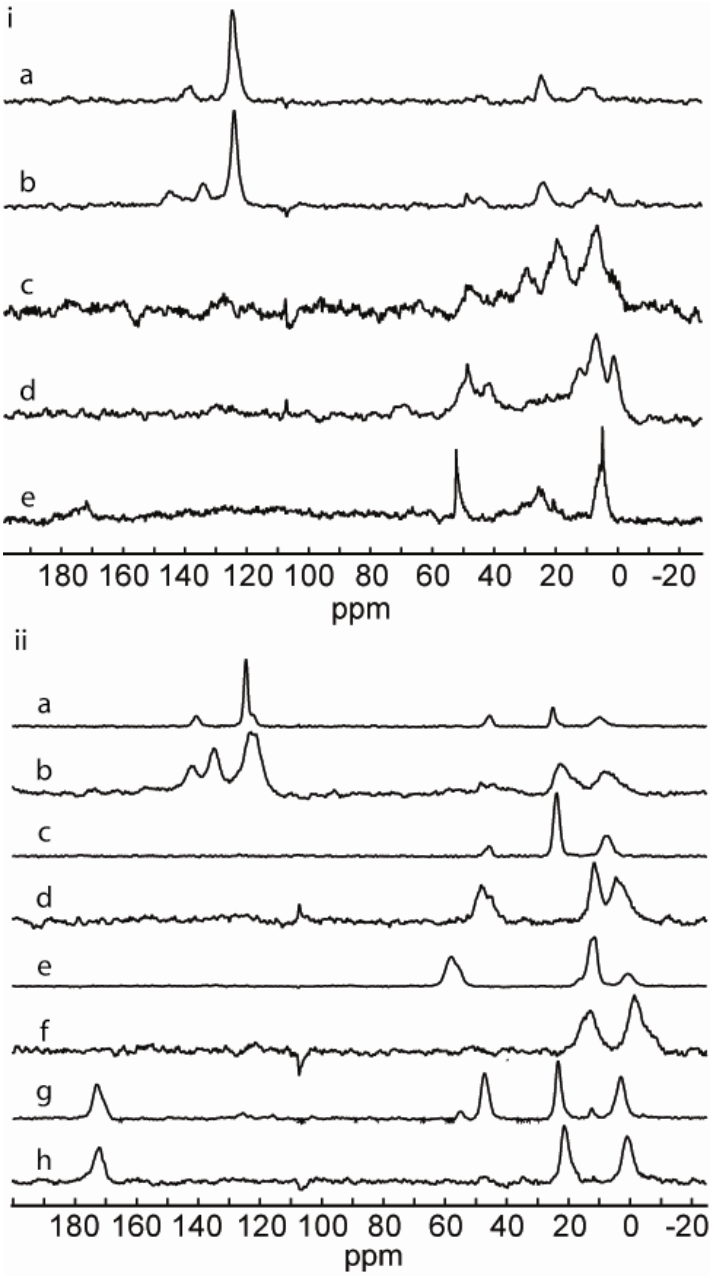

Figure 4.4. ^{13}C CPMAS NMR of i) pure-silica beta samples as follows: a. PE-BEA showing two aromatic resonances and two alkyl resonances arising from the ethyl chain, b. S-PE-BEA showing the same two ethyl resonances but now three aromatic resonances arising from sulfonation, c. MP-BEA, d. S-MP-BEA, e. C-BEA showing a carbonyl resonance centered near 175 ppm and a broad

resonance around 25 ppm arising from ethyl carbons. Spectra were collected on a Bruker Avance 500 MHz spectrometer with a 4 mm rotor. Residual TEA^+ gives rise to resonances near 5 and 50 ppm seen in all spectra. ii) representative MCM-41 samples as follows: a. PE-MCM-41, b. S-PE-MCM-41, c. MP-MCM-41, d. S-MP-MCM-41, e. P-MCM-41 before concentrated HCl reflux, f. P-MCM-41 after concentrated HCl reflux, g. C-MCM-41 before HCl reflux, h. C-MCM-41 after HCl reflux. Spectra of functionalized MCM-48 samples gave spectra similar to those shown in ii.

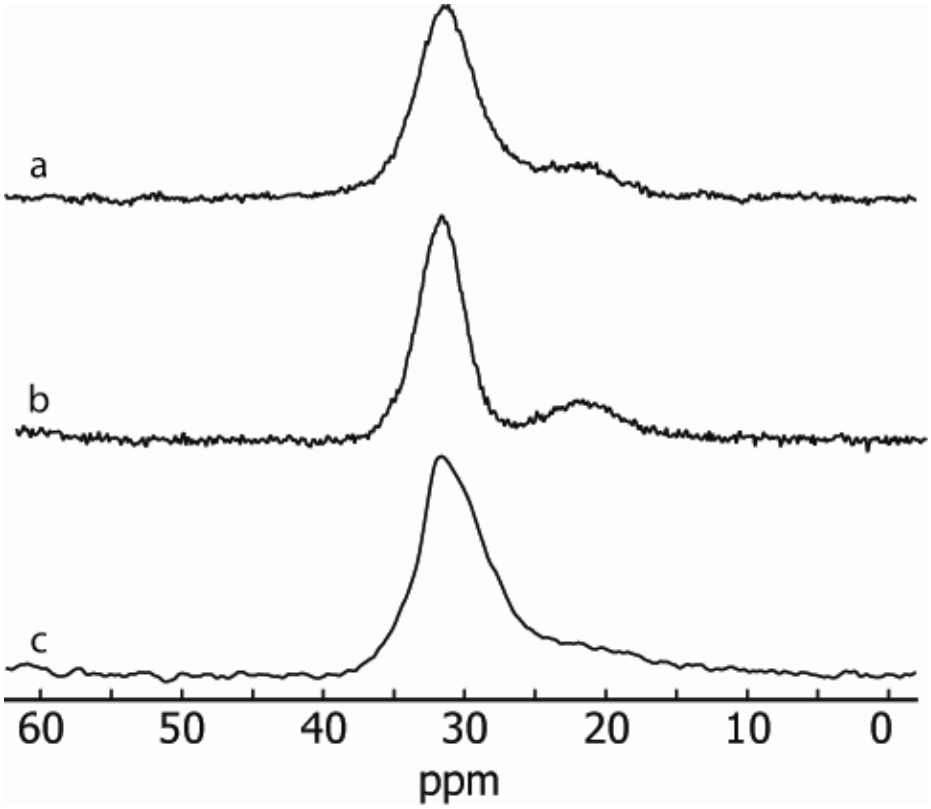

Figure 4.5. ^{31}P CPMAS NMR of HCl refluxed a. P-MCM-41, b. P-MCM-48, and P-BEA. The resonance centered around 32 ppm arises from the di-acid phosphorous while the shoulder at lower chemical shift is from phosphorous with uncleaved ethoxy groups.

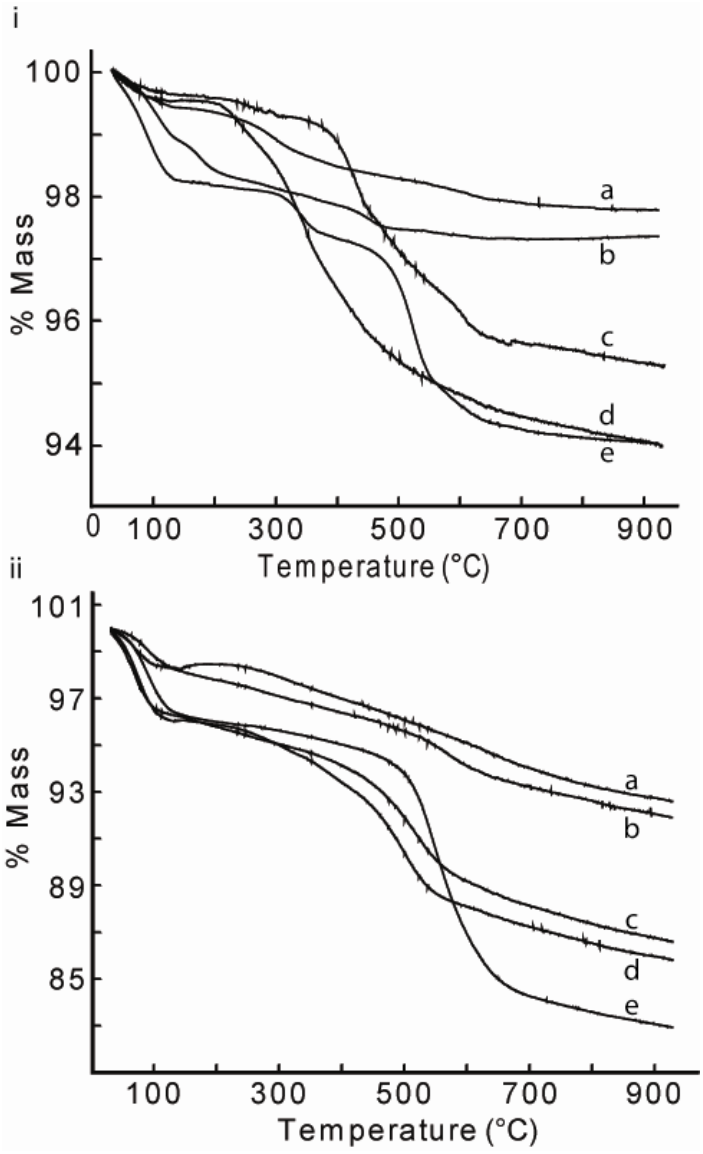

Figure 4.6. Thermogravimetric analysis data of i) acetic acid extracted, organically functionalized pure-silica beta samples as follows: a. P-BEA b. C-BEA, c. unsulfonated PE-BEA illustrating the effective removal of most of the structure directing agent, d. S-MP-BEA, e. S-PE-BEA. ii) representative functionalized MCM-41 samples as follows: a. unfunctionalized MCM-41, b. P-MCM-41, c. C-MCM-41, d. S-MP-MCM-41, e. S-PE-MCM-41. MCM-48 samples gave similar results as those shown for MCM-41 in ii.

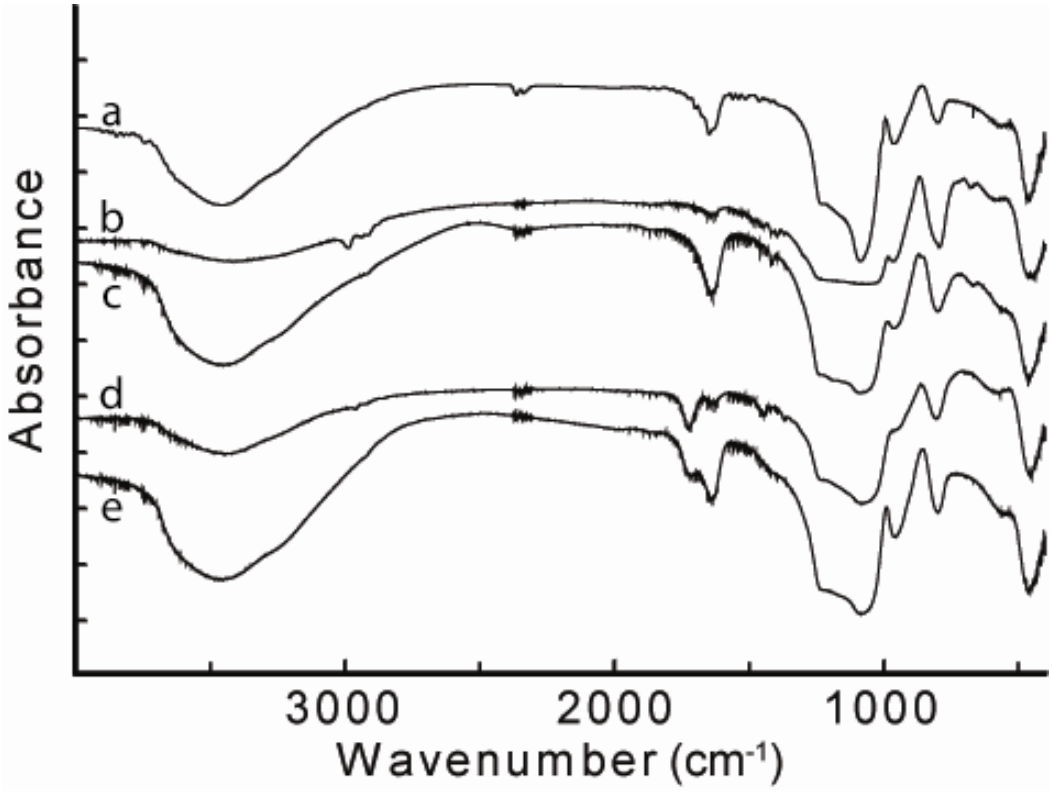

Figure 4.7. FTIR spectra of a. representative MCM-41, b. P-MCM-41 prior to HCl treatment showing a band at 2990 cm^{-1} from the ethoxy groups attached to the phosphorus and a small band at 1390 cm^{-1} from the P=O., c. HCl treated P-MCM-41 where the band at 2990 cm^{-1} is now missing, indicating cleavage of the ethoxy groups, d. C-MCM-41 prior to HCl treatment showing a band at 1730 cm^{-1} from the carbonyl and a band at 1460 cm^{-1} from the methyl ester, e. HCl treated C-MCM-41 showing a carbonyl band at 1730 cm^{-1}, but no band at 1460 cm^{-1} indicating cleavage of the methyl ester.[24]

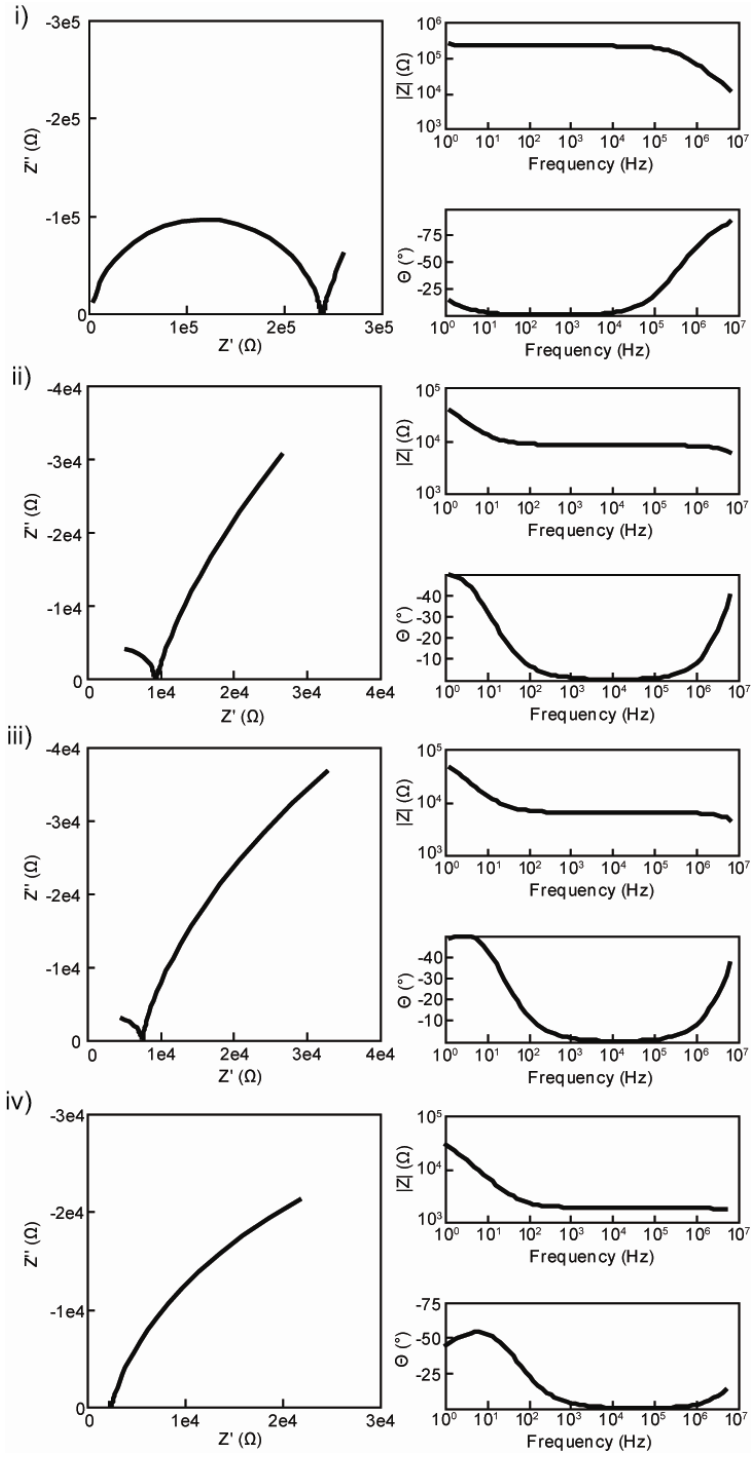

Figure 4.8. Representative impedance spectra of functionalized MCM-41 samples. i) C-MCM-41, ii) P-MCM-41, iii) S-MP-MCM-41, iv) S-PE-MCM-41. Figures in the left column show the commonly observed semicircle observed at

higher frequencies and a low frequency tail generally attributed to charge accumulation at the contacts. Figures in the right column show magnitude and phase of the impedance as functions of frequency. A minimum in the phase curve corresponds to the low-frequency, real-axis intercept of the semicircular arcs depicted in the first column.

Proton conductivity results, organic loadings approximated from thermogravimetric analysis, and acid loadings determined from titration are presented in Table 4.2 for comparison. While care was taken to prepare samples with as similar acid loadings as possible, there is slight variation in the measured acid loadings among samples. These differences, however, are not believed to greatly affect the conclusions, and Table 4.1 shows data for MCM-41 samples with higher organic acid loading, but exhibiting the same trends as those discussed below.

Unfunctionalized, pure-silica materials (MCM-41, MCM-48, BEA) exhibit proton conductivities on the order of 10^{-5} S/cm and treatment with fuming sulfuric acid (O-BEA, O-MCM-41) does not significantly affect these values. MCM-41 and MCM-48 both exhibit slightly higher conductivity than BEA, most likely due to an increased number of surface hydroxyl groups. Measurements were also made on phenethyl functionalized materials prior to sulfonation with oleum, and these non-acidic, organic-containing samples (PE-BEA, PE-MCM-41) exhibit proton conductivities similar to non-functionalized materials.

When samples have acidic organic groups, trends in the proton conductivities within each family of materials exist. Aryl sulfonic acid materials exhibit the highest conductivity values followed by propyl sulfonic acid containing samples, then phosphoric acid functionalized materials, and finally carboxylic acid functionalized materials. This trend of decreasing proton conductivity correlates well with acid strength of organic acid in solution. Acid functionalized materials exhibit higher conductivity than the unfunctionalized parent materials

with the exception of the carboxylic acid containing samples that show nearly the same conductivity as the unfunctionalized materials. This is not surprising as the pKa of propylcarboxylic acid (4.88) is in the range of suggested pKa values for surface hydroxyls of hydrated silica under aqueous conditions.[25-27]

Table 4.1. MCM-41 samples with higher loading

Sample Identity	σ (S/cm)	TGA Loading (mmol/g)	Acid Loading (meq/g)
S-PE-MCM-41	8.3E-03	0.59	0.87
S-MP-MCM-41	4.2E-03	0.62	0.68
P-MCM-41	2.0E-03	0.25	*a*
C-MCM-41	5.7E-05	1.00	0.99

4 mmol/g added to refluxing toluene. The same trend of increasing conductivity with increasing organic acid strength is observed. Note *a.* Ran out of material prior to base reaction/acid back titration.

Table 4.2. Summary of Proton Conductivity and Acid Loading

Sample Identity	σ (S/cm)	TGA Loading (mmol/g)	Acid Loading (meq/g)
BEA	8.8E-06	-	-0.003
MCM-41	2.9E-05	-	0.0055
MCM-48	3.5E-05	-	0.0053
O-BEA	1.5E-05	-	0.0012
O-MCM-41	2.3E-05	-	0.0052
PE-BEA	2.9E-05	0.22	0.0099
PE-MCM-41	1.6E-05	0.27	0.09
C-BEA	1.1E-05	0.06	0.1
P-BEA	1.0E-04	0.04	0.21
S-MP-BEA	4.4E-04	*	0.15
S-PE-BEA	5.4E-04	0.17	0.18
S-PE-BEA-100**	6.7E-03	0.24	0.30
S-PE-BEA-50**	4.9E-03	0.19	0.23
C-MCM-41	2.4E-05	0.43	0.35
P-MCM-41	3.2E-04	0.20	0.41
S-MP-MCM-41	6.9E-04	0.33	0.31
S-PE-MCM-41	2.4E-03	0.34	0.34
C-MCM-48	2.5E-05	0.36	0.30
P-MCM-48	1.1E-03	0.19	0.36
S-MP-MCM-48	2.7E-03	0.29	0.23
S-PE-MCM-48	3.9E-03	0.29	0.28

O – Oleum treated, S – sulfonated, PE – phenethyl, MP – mercaptopropyl, P – phosphonic acid containing, C – carboxylic acid containing, * - could not determine from TGA due to overlap with residual TEA^+, ** data from ref. [28].

Acid functionalized BEA materials (S-PE-BEA, S-MP-BEA, P-BEA, C-BEA) exhibit the lowest proton conductivities for each functionality when compared to MCM-41 and MCM-48 with the same organic functionality. As is shown in a recent report[28], this is due to the hydrophobic nature of the nearly hydroxyl-defect-free framework leading to a less complete hydrogen bonding water network for Grotthüss transport.

Interestingly, acid functionalized MCM-48 samples exhibit higher proton conductivity than the corresponding MCM-41 sample. This observation may arise because of the 3-dimensional interconnected pore structure of MCM-48 as compared to the 1-dimensional pore structure of MCM-41. MCM-41 particles may have their one-dimensional pores aligned perpendicular to the applied electric field, appearing electrically as series resistance, leading to lower measured conductivity as there is no driving force for proton motion along the direction of the pore.

A further comparison can be made between S-PE-MCM-48 and S-PE-BEA-100. S-PE-BEA-100 is an organically functionalized zeolite beta sample (see ref. 22 for synthesis details) crystallized from an aluminum containing gel (SiO_2/Al_2O_3 = 100) using tetraethylammonium hydroxide (instead of the tetraethylammonium fluoride used in the synthesis of the pure silica BEA samples), and has hydroxyl groups like MCM-48. Both S-PE-MCM-48 and S-PE-BEA-100 have interconnected 3-dimensional pore structures and exhibit nearly identical acid loadings by TGA and titration. While the measured conductivities of both of these samples are within the same order of magnitude, the microporous

zeolite beta appears to transport protons at a slightly faster rate than the mesoporous MCM-48 sample.

S-PE-BEA-50, also synthesized from an aluminum containing gel (SiO_2/Al_2O_3 = 50) using tetraethylammonium hydroxide, shows a slightly lower loading than both S-PE-BEA-100 and S-PE-MCM-48 by titration and TGA but has an intermediate proton conductivity, ~$5*10^{-3}$ S/cm. The loading, however, is nearly the same as S-PE-BEA, the pure-silica sample with very little hydroxyl groups. The conductivity of S-PE-BEA, however, is an order of magnitude less than S-PE-BEA-50. As discussed in a recent report[28] this is attributed to the higher number of hydroxyl groups in zeolite beta samples crystallized from hydroxide containing synthesis gels.

From a device perspective where proton conductivity is to be maximized to reduce internal ohmic losses, hydroxyl groups are clearly necessary, but further considerations exist. While, S-PE-MCM-48 and S-PE-BEA-100(50) exhibit similar proton conductivity (~$5*10^{-3}$ S/cm), the small pores of zeolite beta may better inhibit the crossover of methanol from the anode to the cathode, eliminating one cause of decreased efficiency. The small zeolitic pores may also retain water at high temperatures better than the mesopores of MCM-41 or MCM-48. Admittedly, particle size, which does not seem to affect the measured conductivy[17,28], may play a role in the reduction of methanol crossover if these powder materials are successfully fabricated into membranes, but methanol crossover measurements are beyond the scope of this investigation.

4.5. Conclusion

In conclusion, pure-silica zeolite beta, MCM-41 and MCM-48 containing sulfonic acids, phosphonic acid, or carboxylic acid were prepared and investigated for use as solid electrolytes. Aryl sulfonic acid containing samples exhibit the highest measured proton conductivity values, followed by propyl sulfonic acid containing materials, phosphoric acid containing materials and carboxylic acid materials that were approximately the same as non-organically modified silicas. MCM-41 and MCM-48 show higher proton conductivities than corresponding pure-silica zeolite beta samples, and MCM-48 samples are slightly more conductive than corresponding MCM-41 samples. An aryl sulfonic acid functionalized zeolite beta sample with hydroxyl groups, however, appears to be a slightly better proton conductor than the corresponding MCM-48 sample functionalized to the same acid loading level, although the improvement is small and would, alone, no industrially justify the increased cost of synthesis of nanocrystalline materials in comparison to mesoporous materials. Reduced methanol crossover, however, may provide further benefit to the nanocrystalline zeolite beta sample.

4.6. References

(1) Watanabe, M.; Uchida, H.; Seki, Y.; Emori, M.; Stonehart, P. *J. Electrochem. Soc.* **1996**, *143*, 3847.

(2) Adjemian, K. T.; Lee, D. J.; Srinivasan, S.; Benziger, J.; Bocarsly, A. B. *J. Electrochem. Soc.* **2002**, *149*, A256.

(3) Ladewig, B. P.; Knott, R. B.; Hill, A. J.; Riches, J. D.; White, J. W.; Martin, D. J.; Costa, J. C. D. d.; Lu, G. Q. *Chem. Mater.* **2007**, *19*, 2372.

(4) Mauritz, K. A. *Mater. Sci. Eng., C* **1998**, *6*, 121.

(5) Baglio, V.; Di Blasi, A.; Arico, A. S.; Antonucci, V.; Antonucci, P. L.; Trakanprapai, C.; Esposito, V.; Licoccia, S.; Traversa, E. *J. Electrochem. Soc.* **2005**, *152*, A1373.

(6) Kim, H. J.; Lim, J. E.; Shul, Y. G.; Han, H. Mesoporous silica: Polymer composite membrane for direct methanol fuel cell. In *Recent Advances in the Science and Technology of Zeolites and Related Materials, Pts. A - C*, 2004; Vol. 154; pp 3036.

(7) Hogarth, W. H. J.; da Costa, J. C. D.; Drennan, J.; Lu, G. Q. *J. Mater. Chem.* **2005**, *15*, 754.

(8) Lin, Y.-F.; Yen, C.-Y.; Ma, C.-C. M.; Liao, S.-H.; Lee, C.-H.; Hsiao, Y.-H.; Lin, H.-P. *J. Power Sources* **2007**, *171*, 388.

(9) Pereira, F.; Valle, K.; Belleville, P.; Morin, A.; Lambert, S.; Sanchez, C. *Chem. Mater.* **2008**, *20*, 1710.

(10) Li, X.; Roberts, E. P. L.; Holmes, S. M.; Zholobenko, V. *Solid State Ionics* **2007**, *178*, 1248.

(11) Chen, Z. W.; Holmberg, B.; Li, W. Z.; Wang, X.; Deng, W. Q.; Munoz, R.; Yan, Y. S. *Chem. Mater.* **2006**, *18*, 5669.

(12) Halla, J. D.; Mamak, M.; Williams, D. E.; Ozin, G. A. *Adv. Funct. Mater.* **2003**, *13*, 133.

(13) Marschall, R.; Bannat, I.; Caro, J.; Wark, M. *Microporous Mesoporous Mater.* **2007**, *99*, 190.

(14) Otomo, J.; Wang, S.; Takahashi, H.; Nagamoto, H. *J. Membr. Sci.* **2006**, *279*, 256.

(15) Li, H.; Nogami, M. *Adv. Mater.* **2002**, *14*, 912.

(16) Mikhailenko, S.; Desplantier-Goscard, D.; Danumah, C.; Kaliaguine, S. *Microporous Mesoporous Mater.* **2002**, *52*, 29.

(17) Holmberg, B. A.; Hwang, S.-J.; Davis, M. E.; Yan, Y. *Microporous Mesoporous Mater.* **2005**, *80*, 347.

(18) Alabi, C. A.; Davis, M. E. *Chem. Mater.* **2006**, *18*, 5634.

(19) Jones, C. W.; Tsuji, K.; Davis, M. E. *Microporous Mesoporous Mater.* **1999**, *33*, 223.

(20) Camblor, M. A.; Corma, A.; Valencia, S. *Chem. Commun.* **1996**, 2365.

(21) Thommes, M.; Kohn, R.; Froba, M. *J. Phys. Chem. B* **2000**, *104*, 7932.

(22) Holmberg, B. A.; Yan, Y. *J. Electrochem. Soc.* **2006**, *153*, A146.

(23) Mikhailenko, S. D.; Kaliaguine, S.; Ghali, E. *Microporous Materials* **1997**, *11*, 37.

(24) Colthup, N. B.; Daly, L. H.; Wimberly, S. E. *Introduction to Infrared and Raman Spectroscopy*; Academic Press Incorporated: New York, 1975.

(25) Iler, R. K. *The Chemistry of Silica: solubility, Polymerization. Colloid and Surface Properties, and Biochemistry*; John Wiley & Sons, Inc.: New York, 1979.

(26) Rosenholm, J. M.; Czuryszkiewicz, T.; Kleitz, F.; Rosenholm, J. B.; Linden, M. On the Nature of the Bronsted Acidic Groups on Native and Functionalized Mesoporous Siliceous SBA-15 as Studied by Benzylamine Adsorption from Solution, 2007; Vol. 23; pp 4315.

(27) Ong, S.; Zhao, X.; Eisenthal, K. B. *Chem. Phys. Lett.* **1992**, *191*, 327.

(28) McKeen, J. C.; Yan, Y. S.; Davis, M. E. *Chem. Mater.* **2008**, *20*, 3791.

5. Conductivity of Mono- and Divalent Cations in the Microporous Zincosilicate VPI-9

5.1. Abstract

Impedance spectroscopy is used to investigate the long-range ionic conductivity of the microporous, zincosilicate VPI-9 (Si/Zn = 4.0) (International Zeolite Association framework type VNI) containing the alkali cations Li^+, Na^+, K^+, Rb^+, and Cs^+, and the alkaline earth cations Mg^{2+}, Ca^{2+}, and Sr^{2+}. Monovalent cation exchanged samples Li- and Na-VPI-9 lose X-ray crystallinity upon vacuum dehydration at 450 °C, while K-, Rb-, and Cs-VPI-9 remain crystalline and exhibit conductivities of 1.7 x 10^{-4}, 3.5 x 10^{-4}, and 4.9 x 10^{-4} S/cm, respectively, at 450 °C and activation energies of 0.72, 0.64, and 0.69 eV, respectively, in the temperature range 150 to 450 °C. Divalent cation exchanged sample Mg-VPI-9 also loses X-ray crystallinity, while Ca-, and Sr-VPI-9 remain crystalline and exhibit conductivities of 2.3 x 10^{-6} S/cm and 7.7 x 10^{-7} S/cm, respectively, at 450 °C, and activation energies of 0.88 and 0.91 eV, respectively, over the temperature range 150 to 450 °C. When compared to aluminosilicate zeolite X (Si/Al = 1.25) exchanged with the same cations, all crystalline M-VPI-9 materials have greater conductivities than M-X with the exception of K-X (1.6 x 10^{-3} S/cm at 450 °C), with the greatest differences arising between the divalent exchanged materials. Dense, crystalline zincosilicate samples with the compositions $K_2ZnSi_xO_{2(x+1)}$ (x = 2-5), $Rb_2ZnSi_5O_{12}$, and $Cs_2ZnSi_5O_{12}$ are also prepared and characterized for comparison with the microporous materials, and exhibit much

lower conductivities than their microporous counterparts at the same composition.

5.2. Introduction

While zeolites and zeolite-like materials have been used in ion exchange, adsorption and catalytic applications for decades, new potential applications continue to arise[1], including low-k dielectric films for microelectronics[2], proton conductors in fuel cells[3-6], anticorrosion[7] and antimicrobial[8] coatings, and small molecule drug delivery agents[9]. Microporous materials exist where the $[AlO_4]^{1-}$ are replaced with other tetrahedral units such as $[BeO_4]^{4-}$, $[GaO_4]^{3-}$, and, in the case of the zincosilicates, $[ZnO_4]^{4-}$. The incorporation of tetrahedrally coordinated zinc into the silica framework creates two anionic framework sites per zinc atom and, as in the aluminosilicates, these anionic sites must be balanced by positively charged entities. This is schematically shown in Figure 5.1 for the case of sodium exchanged materials. The first synthetic, microporous zincosilicates were prepared in the mid 1990s in the search for lower-framework-density materials and include VPI-7 [10], VPI-8 [11-13], VPI-9 [14-16], VPI-10, CIT-6 [17-19], and RUB-17 [20], among others. Of the known high zinc content zincosilicates, VPI-7, VPI-9, VPI-10, and RUB-17, there are no pure-silica or aluminosilicate analogs because of the high number of 3-membered rings (3MRs). VPI-9 has all of the tetrahedrally coordinated zinc located within these 3MRs that are ordered throughout the crystalline, microporous framework[16]. The ordering of the zinc leads to ordering of the charge-balancing cations in the channels of the 3-dimensional pore network. VPI-9 does not contain cages like the high charge

containing zeolites. Figure 5.1 also illustrates the absence of internal cages in VPI-9 in comparison to the presence of the smaller β cages and larger α cages in zeolite X or Y. Because of this unique, long-range ordering and the fact that the framework zinc imparts two anionic framework charge centers per zinc atom, it is of interest to study the ionic conductivity (as the zincosilicate framework is electronically insulating) arising from the charge balancing cations within the pores of VPI-9. While reports on the ionic conductivity of various cations exist for a handful of the known aluminosilicates, containing single anionic frameworks sites from framework aluminum, only one report on potential conductivity arising from octahedrally coordinated titanium sites in ETS-10, a non zeolite, microporous, crystalline solid, has appeared [21].

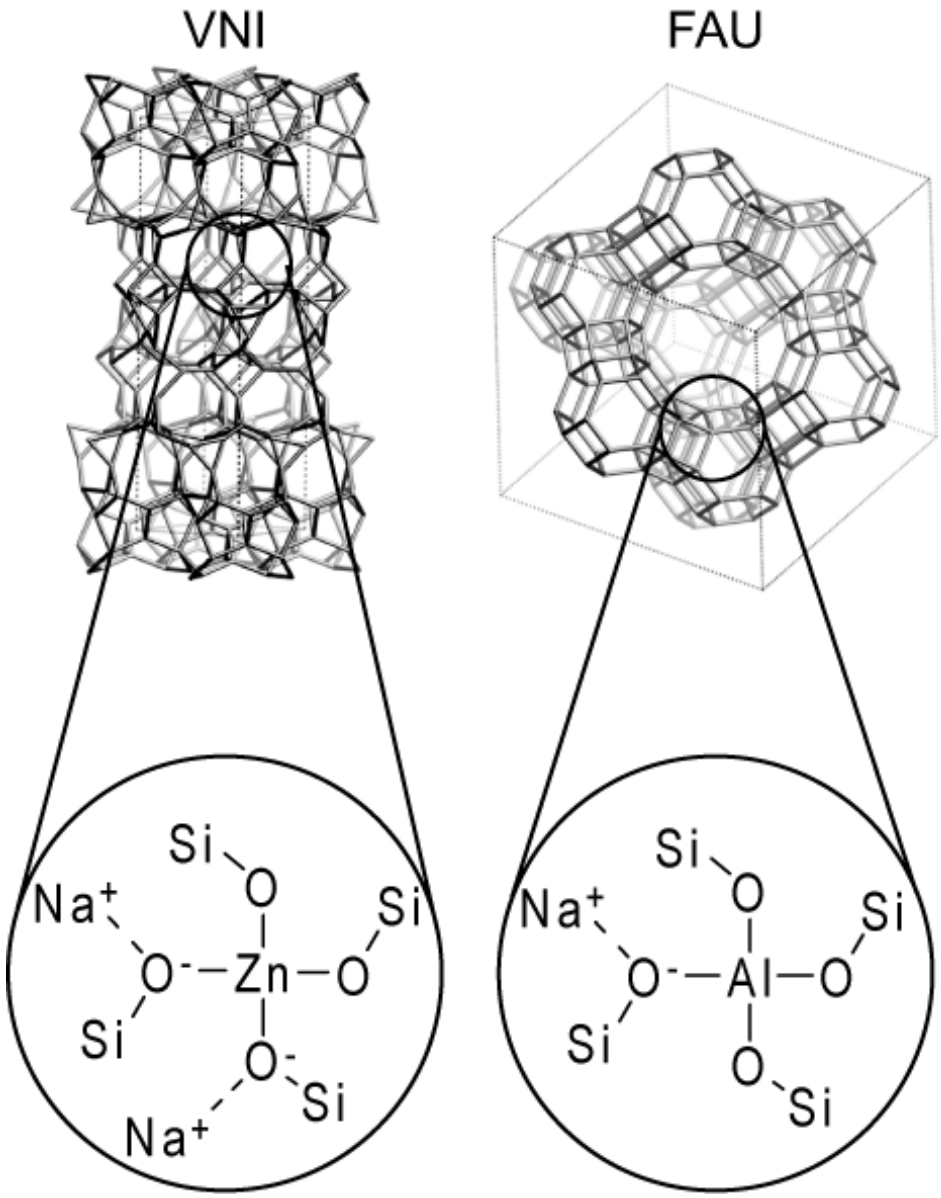

Figure 5.1. Schematic representation of anionic sites arising from framework zinc in VPI-9 versus anionic sites arising from framework aluminum in zeolite X. Dashed lines represent electrostatic interaction of the charge balancing cation with the anionic framework.

A method for measuring ionic conductivity is impedance spectroscopy, where a sinusoidally varying voltage is applied across the sample of interest, and the current flowing through the sample is measured as a function of the sinusoidal frequency. The complex impedance (Z*) is then calculated by dividing the complex voltage by the complex current, as a function of frequency. A typical model for ion transport through a grain of powdered material is the parallel combination of a resistor and capacitor, which in the frequency domain (after applying the Laplace transform) traces out a semicircle in the complex (-Z" v. Z') plane as a function of frequency. The conductivity of the sample is then calculated by geometrically scaling the low frequency intercept of the semicircle with the Z' (real) axis. In practice, the low-frequency, Z', intercept may be a combination of impedances, such as intragrain and grain boundary impedances, although a powerful aspect of impedance spectroscopy is the ability to separate various contributions to the overall impedance if the time constants for the various processes are well resolved. When impedance data are collected as a function of temperature, activation energy for transport, E_A, can be measured by fitting conductivity data to Equation 5.1, where k is Boltzman's constant, E_A is the activation energy, σ is the conductivity, σ_0 is the preexponential factor, and T is the temperature in Kelvin.

$$\sigma = \frac{\sigma_0}{T} Exp\left(\frac{E_A}{kT}\right) \tag{5.1}$$

Zeolite X and zeolite Y (framework topology FAU) have received considerable attention and exhibit among the best reported ionic conductivities

among zeolites and zeolite-like materials.[22-37] Numerous research efforts have been devoted to characterizing the ion conducting properties of zeolite X and Y, as well as understanding internal relaxation properties occurring within the α cages of these zeolites. Zeolites X and Y have also been used as standards in characterizing new materials, and data on zeolite X are presented herein alongside the VPI-9 data, and in the supporting information in modulus representation.

Here, impedance spectroscopy has been used to study the ion conducting properties of microporous zincosilicate VPI-9 containing various mono- and divalent cations over the temperature range 25 – 450 °C. Comparisons to zeolite X are presented and activation energies are reported. In addition, dense zincosilicate samples containing potassium, rubidium, and cesium, have been prepared and characterized using impedance spectroscopy, with results presented for comparison to porous VPI-9.

5.3. Experimental

5.3.1. VPI-9 Synthesis and Ion Exchange

VPI-9 was synthesized according to a published procedure.[16] In short, a reaction mixture with the composition 0.6 RbOH:0.3 KOH:0.08 TEAOH:0.04 ZnO: 1.0 SiO_2:22 H_2O was prepared by combining the inorganic and organic cations in water, followed by the addition of zinc oxide. Silicon dioxide (Syloid 63) was then added and the resulting mixture was stirred for 2 hours. The final reaction mixture was loaded into Teflon-lined, stainless steel autoclaves (Parr) and allowed to

crystallize under autogeneous pressure, statically, at 200 °C in convection ovens for 5 days. Rubidium hydroxide (50 wt.%, aq.), potassium hydroxide (45 wt.%, aq.), tetraethylammonium hydroxide (TEAOH, 35 wt% aq.), and zinc oxide were purchased from Aldrich and the water used in the synthesis and later ion exchange was deionized and distilled (DDI). After crystallization, the bombs were removed from the convection ovens and quenched in cold water. Crystallized products were collected by vacuum filtration, washed with DDI water, dried at 100 °C, and ground with a mortar and pestle.

Ion exchange of VPI-9 and zeolite X (Aldrich, Si/Al = 1.25, sodium form) was accomplished by repeatedly contacting powder samples with 1 M aqueous solutions of nitrate or chloride salts of the desired cation. A typical exchange cycle was 1 g of powder to 20 mL of solution contacted for 24 hours at 37 °C on a shaker table. For each subsequent exchange cycle, samples were decanted and 20 mL of fresh solutions were added. Exchange was monitored semi-quantitatively by energy dispersive spectroscopy (EDS).

5.3.2. Synthesis of Dense Zincosilicates

Four dense zincosilicate samples were synthesized in accordance with published procedures,[38-40] while the remaining two were prepared using the same high temperature method as above, but not hydrothermally, as reported in literature.[41,42] The desired alkali metal carbonate (Aldrich, 99.999%), zinc oxide (Aldrich, 99.999%), and silicon dioxide (Aldrich, 99.995+%) were mixed in the appropriate molar quantities and ground with a marble mortar and pestle to insure good mixing. The powders were then loaded into a platinum crucible and

heated to 750 °C for 12 hours to decompose the carbonates. Samples were then heated to a temperature above their melting temperature (see Table 5.1), held there for 12 hours, slowly cooled to 650 °C, and then allowed to cool to room temperature. Upon removal from the platinum crucible, all samples appeared glassy. The resulting materials were ground to fine powders, pressed axially into pellets with a hydraulic press between tungsten carbide dies, and heated to a crystallization temperature (see Table 5.1) for 60 hours. This process was repeated until no changes in the powder X-ray diffractograms were observed from subsequent firings.

Table 5.1. Synthesis, Crystallization, and Sintering Temperatures for Dense Zincosilicates.

	Synthesis (°C)	Crystallization (°C)	Sintering (°C)
$K_2ZnSi_2O_6$	1150	850	900
$K_2ZnSi_3O_8$	1050	850	900
$K_2ZnSi_4O_{10}$	1050	850	900
$K_2ZnSi_5O_{12}$	1075	850	900
$Rb_2ZnSi_5O_{12}$	1350	850	900
$Cs_2ZnSi_5O_{12}$	1410	1000	1100

5.3.3. Powder X-ray Diffraction

Powder X-ray diffraction patterns were obtained using a Scintag XDS 2000 with Cu *k-α* radiation (40 kV, 36 mA). Step sizes were generally 0.04° with accumulation times of 0.5 – 1 second. Pelletized samples were mounted on modeling clay and leveled with a glass slide.

5.3.4. Energy Dispersive Spectroscopy (EDS)

Energy Dispersive Spectroscopy was used to monitor ion exchange and estimate the final composition of all samples. EDS was performed using a LEO 1550 VP Field Emission SEM equipped with an Oxford INCA 300 X-ray energy dispersive spectrometer system.

5.3.5. Impedance Spectroscopy

Powder samples were prepared for impedance spectroscopic (IS) characterization by axial hydraulic pressing between 13 mm tungsten carbide dies. All samples were pressed with 12000 lbs of force and measured 300-600 microns in thickness. It was experimentally determined that pressing above 8000 lbs led to consistent results regardless of further applied force. VPI-9 and zeolite X samples were used as-pressed, but dense samples were sintered to produce mechanically stable pellets and decrease grain boundary impedances. See Table 5.1 for sintering temperatures. Gold contacts were then masked and vacuum sputtered onto both sides of the pellet to ensure good electrical contact with the samples and eliminate interface impedance effects.

A vacuum system and probe were constructed for sample characterization. The probe consisted of an alumina sample holder with platinum contacts. The bottom contact was a flat plate while the top contact was a rounded platinum rod used to gently touch the masked 4 mm gold contact through a thin 3 mm diameter platinum disc. The probe was spring loaded for the application of light force. An electrically insulated thermocouple was mounted within 1/8" of the bottom electrode to accurately measure the sample temperature, and a ceramic fiber heater was used to change the temperature of the sample and holder. The sample cell was mounted to a modified Novocontrol BDS1200 sample cell and short platinum wires formed the electrical connections between the platinum contacts and the coaxial vacuum lines of the BDS12000.

A Solartron 1260A Impedance/Gain-Phase analyzer connected to a Solartron 1296A dielectric interface was used to measure the impedance of the sample, in conjunction with the Solartron SMaRT software.

Prior to characterization, all samples were heated to 450 °C under high vacuum (1×10^{-6} – 7×10^{-6} Torr) for at least 12 hours to ensure proper dehydration. Measurements were then made in decreasing temperature increments with 10 points per decade of frequency.

5.4. Results and Discussion

5.4.1. Ion Exchange of VPI-9 and Zeolite X

Energy dispersive spectroscopy (EDS) was used to analyze the composition of the exchanged VPI-9 and zeolite X samples and Table 5.2 shows

the results obtained. Sample compositions have been normalized to silicon. Lithium is not detectable by EDS, so lithium exchange was monitored and inferred by the disappearance of potassium and rubidium in VPI-9 and sodium in zeolite X. Peaks arising from strontium and silicon overlap in the EDS spectra, so strontium exchange was also monitored by the disappearance of the aforementioned elements. VPI-9 and zeolite X containing alkali metals as the charge balancing cation all appear slightly deficient in the alkali cation. This may be an artifact of the EDS method as alkali exchanged zeolite X and potassium, rubidium, and cesium containing dense zincosilicates exhibit similar deficiencies. Magnesium and calcium exchanged samples appear closer to the as-expected 1:1, M:Zn (M = Mg, Ca). With the exception of Sr-VPI-9, in which occasional grains contained trace potassium (less than 1 atomic %), all exchanges appear quantitative. Zeolite X, however, is known to not fully exchange with all alkali and alkaline earth cations, and the exchange levels achieved correspond to the maximum exchange levels, as suggested by Breck.[43] Quantitative exchange was achieved in K-X, Ca-X, and Sr-X. All materials characterized by EDS also show an excess of oxygen, perhaps another artifact of the analytical methodology.

Table 5.2. EDS Elemental Analysis Results for Ion Exchanged VPI-9 and Zeolite X Samples.

	M	Si	Zn	O		M	Si	Al	O	Na
Li-VPI-9	ND[a]	4	1.0	11.8	Li-X	ND[a]	1	0.8	6.0	0.1
Na-VPI-9	1.6	4	1.0	11.2	Na-X	0.7	1	0.8	5.1	-
K-VPI-9	1.7	4	1.0	14.4	K-X	0.6	1	0.8	4.9	ND[c]
Rb-VPI-9	1.4	4	1.0	12.5	Rb-X	0.3	1	0.7	5.0	0.2
Cs-VPI-9	1.8	4	1.0	12.1	Cs-X	0.3	1	0.8	5.3	0.2
Mg-VPI-9	0.9	4	1.0	12.4	Mg-X	0.4	1	0.8	6.2	0.1
Ca-VPI-9	1.0	4	0.9	13.6	Ca-X	0.3	1	0.8	5.9	ND[c]
Sr-VPI-9[b]					Sr-X[b]					ND[c]

ND - none detected

a. lithium is not detectable by this EDS instrument

b. strontium and silicon peaks overlap in EDS spectra and an accurate separation could not be made

c. no sodium was detected in sample

5.4.2. Powder X-ray Diffraction Patterns of M-VPI-9

Powder X-ray diffraction was performed after ion exchange to confirm that diffraction patterns were consistent with the as-synthesized VPI-9 parent material and with published X-ray data.[16] Powder X-ray diffraction patterns for the VPI-9 materials are shown in Figure 5.2a and while there are slight shifts in peak intensity and position as the charge balancing cation changes, as was first observed in VPI-7 by Annen,[44] the VPI-9 framework remains intact, perhaps with the exception of magnesium exchanged VPI-9, which exhibits a larger decrease in peak intensity when compared to all other samples.

After vacuum dehydration at 450 °C and subsequent impedance spectroscopic characterization, diffractograms of pelletized samples were collected and are shown in Figure 5.2b. In all samples, the peak appearing near 38.5° arises from the gold top contact. While peak intensities are decreased in comparison to the respective powder samples due to a reduced sample area and partial gold coating, samples of strontium, calcium, cesium, rubidium, and potassium exchanged VPI-9 retain their crystallinity upon dehydration. Magnesium, sodium, and lithium exchanged samples become X-ray amorphous upon dehydration and this is further reflected by their significantly decreased conductivities (shown later) in comparison to the exchanged VPI-9s that remain crystalline. Dehydration at 350 °C was attempted in an effort to not destroy the VPI-9 structure in Mg, Na, and Li exchanged samples, but pellets were found to be X-ray amorphous even after this more mild dehydration. Diffractograms of

dehydrated zeolite X samples (not shown) all remained crystalline and exhibited the well-known FAU diffraction pattern.

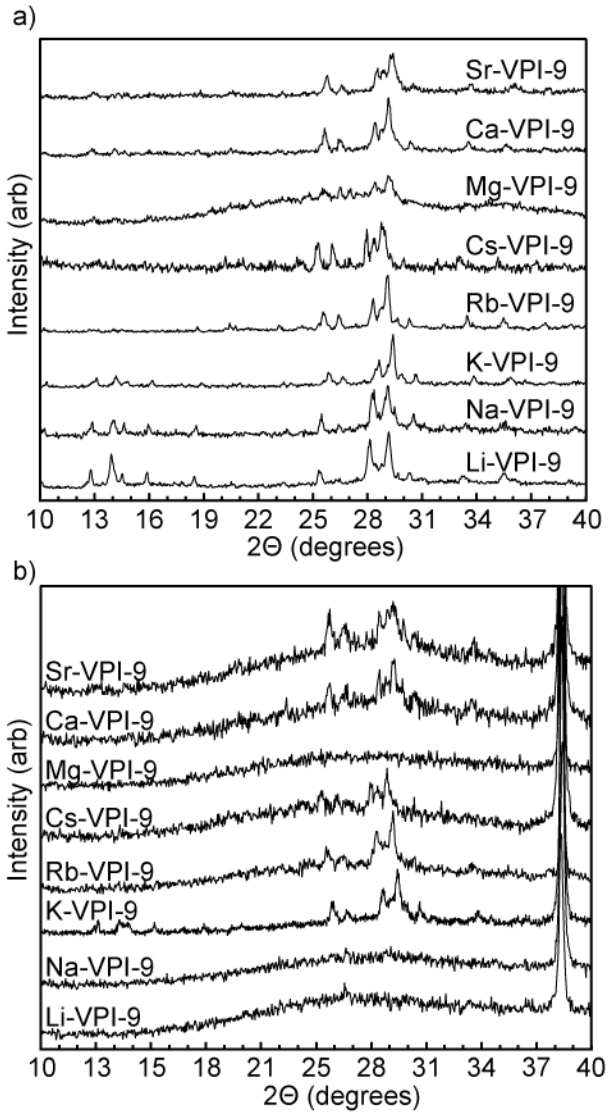

Figure 5.2. a) Powder X-ray diffractograms of ion exchanged VPI-9 showing, with perhaps the exception of Mg-VPI-9, that VPI-9 structure is maintained after ion exchange. b) X-ray diffractograms of vacuum dehydrated pellets of ion-exchanged VPI-9 samples. Li-, Na-, and Mg-VPI-9 become X-ray amorphous.

5.4.3. Impedance Spectroscopy

Impedance spectroscopy is performed to investigate the ionic conductivity of VPI-9 (and zeolite X) exchanged with various alkali and alkaline earth cations. Using a parallel plate capacitor structure, the impedance is measured and the conductivity extracted by scaling the direct current DC resistance with the cross-sectional area of the capacitor structure and thickness of the pellet, typically 300-600 μm. Typical impedance spectra are shown in Figure 5.3 for potassium exchanged VPI-9 and zeolite X at 350 °C, and data exhibit a high frequency, depressed semicircle and the often observed low frequency tail indicative of ionic conductivity (normally attributed to the ionically blocking nature of gold or other metallic contacts). The DC resistance of each sample is read from the low frequency intercept of the semicircular arc with the real axis or by curve-fitting a semicircular arc to the data and extrapolating to the Z' axis. While curves for both K-VPI-9 and K-X are shown in the same figure, note the different scales for each curve (the K-VPI-9 pellet exhibits a larger resistance than the K-X pellet).

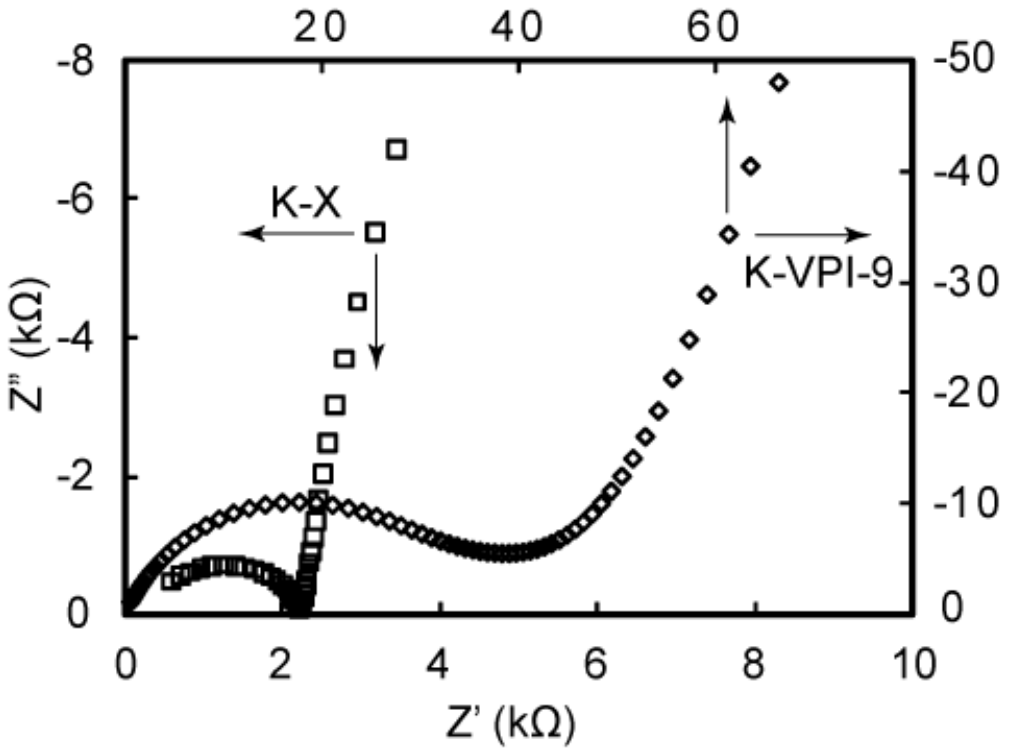

Figure 5.3. Typical impedance spectra showing high-frequency semicircular arc and low frequency “tail” arising from contact effects. Notice the different scales for potassium exchanged zeolite X and potassium exchanged VPI-9.

5.4.4. Ionic Conductivity and Activation Energy in M^+-VPI-9

Impedance spectra recorded from 450 °C to room temperature were used to calculate the conductivity of each sample as a function of temperature, and the data, presented in terms of the product of the DC conductivity, σ_{DC}, and the temperature are plotted versus the inverse temperature in Figure 5.4a for monovalent cation exchanged samples and in Figure 5.4b for divalent cation exchanged samples. Open markers indicate zeolite X samples while filled markers correspond to VPI-9 samples. All samples display activated transport behavior, that is decreasing conductivity with decreasing sample temperature. To help elucidate trends in conductivity with ionic radius, the conductivity of each ion-exchanged sample, measured at 400 °C, is plotted versus ionic radius for both mono- and divalent exchanged samples of VPI-9 and zeolite X in Figure 5.5a. Activation energy for each sample is extracted from the slope of the corresponding line, and these values are reported in Figure 5.5b.

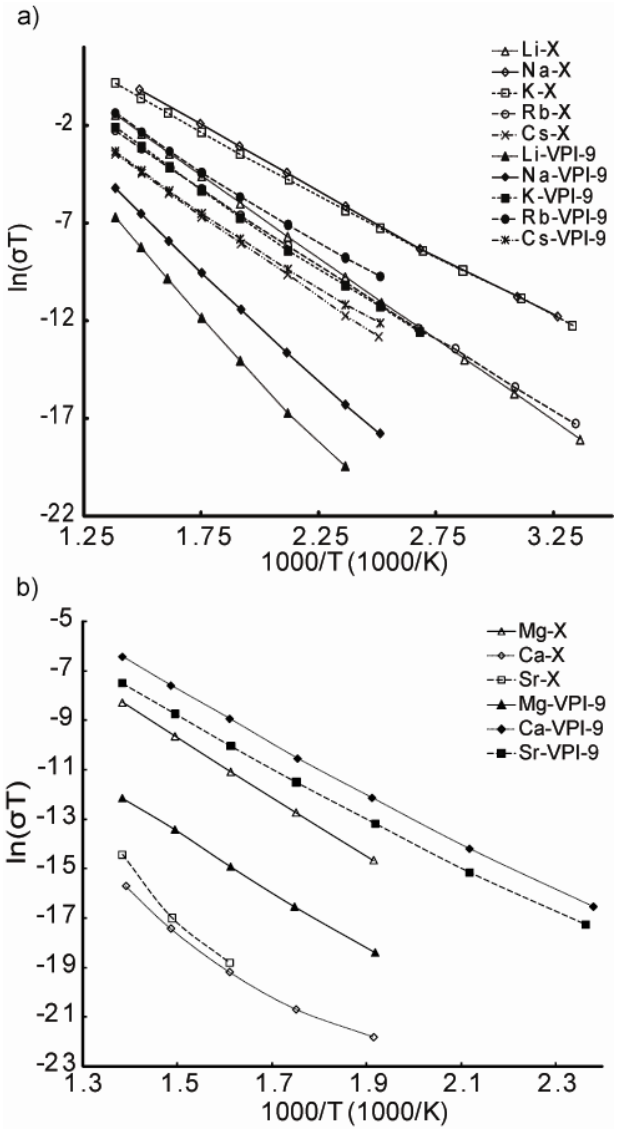

Figure 5.4. Ionic conductivity presented as the natural log of the product of conductivity and temperature versus the inverse temperature for a) monovalent exchanged zeolite X samples shown with open markers, and monovalent exchanged VPI-9 samples shown with filled markers, and b) divalent exchanged zeolite X samples shown with open markers, and monovalent exchanged VPI-9 samples shown with filled markers. Lines connecting markers are for the eyes' guidance.

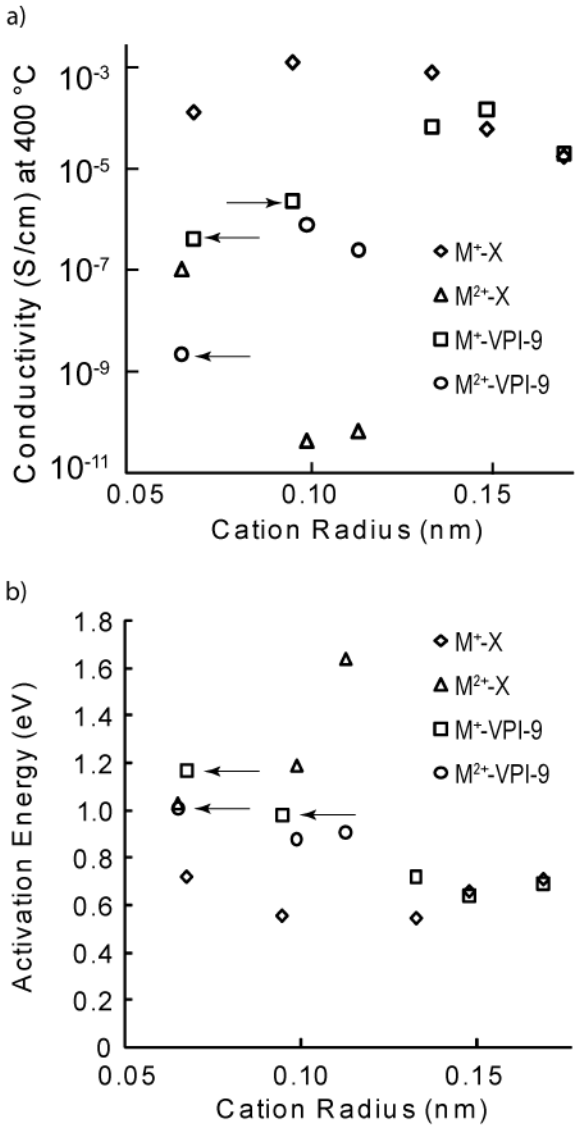

Figure 5.5. a) Ionic conductivity at 400 °C of mono- and divalent exchanged zeolite X and VPI-9 shown as a function of cation radius. b) activation energy of mono- and divalent exchanged zeolite X and VPI-9 shown as a function of cation radius. Arrows in both a) and b) point to amorphous Li-, Na-, and Mg-VPI-9 samples.

Sodium and potassium exchanged zeolite X possesses the highest conductivity among the alkali exchanged X zeolites. The lithium cation, while smaller than the sodium and potassium cations, has less mobility within the zeolite X framework, and this has been attributed to stronger electrostatic interactions of the small lithium cation with the anionic framework sites when compared to the larger and more delocalized sodium and potassium cations.[28] For the cases of rubidium and cesium cations that are even more delocalized than sodium and potassium cations, cation-cation interaction, due to their increased ionic radii, has been suggested as a potential reason for the increased activation energy, as the activation energy has been shown to monotonically decrease from lithium to cesium in zeolite Y [28,37] where the cations are, on average, spaced further apart than in zeolite X due to the reduced number of anionic aluminum framework sites. Further spacing between cations reduces contributions to the activation energy from cation-cation repulsion and the activation energy is dominated by electrostatic interaction of the charge balancing cation with the anionic framework site. In monovalent cation containing VPI-9, lithium and sodium exchanged samples lose crystallinity upon vacuum dehydration (data in Figure 5.4 indicated by arrows) and will not be discussed further. Potassium, rubidium, and cesium exchanged VPI-9 retain crystallinity upon dehydration. Rb-VPI-9 shows the highest conductivity, followed by Cs-VPI-9 and K-VPI-9. One plausible explanation for this trend is that the increased size of rubidium leads to reduced electrostatic interaction with the anionic framework sites thus increasing the ease with which Rb^+ moves from site to site. While the

Cs^+ would have even lower electrostatic interaction than Rb^+, sterics or ion-ion interactions in the small pores of VPI-9 may adversely affect the conductivity of the larger cesium ion. Potassium exchanged VPI-9 has lower conductivity than potassium exchanged zeolite X, but both cesium and rubidium exchanged VPI-9 exhibit higher conductivity than cesium and rubidium exchanged zeolite X, respectively. The data most likely under exaggerates this higher conductivity in VPI-9 materials compared to corresponding zeolite X materials as cesium and rubidium exchange in zeolite X were not complete (Cs and Rb are too large to enter the small β cages) and fast-moving, residual sodium can significantly contribute to the overall conductivity. In Rb-VPI-9 and Cs-VPI-9 the exchange appears complete by EDS and measure conductivity values reflect the conductivity of the desired cation.

Activation energies from K-, Rb-, and Cs-VPI-9 follow an opposite trend from their conductivities as the activation energies order, Rb-VPI-9 < Cs-VPI-9 < K-VPI-9. Activation energies measured here for alkali exchanged zeolite X are in accordance with previously reported values, *e.g,.* 0.56 eV for Na-X.[26,28,37] As the data in Figure 5.5b show, activation energy is a concave function of cation radius for both the VPI-9 and zeolite X exhibiting minimum in activation energy, Rb^+ for VPI-9 and K^+ for zeolite X, and is contrary to the monotonically decreasing trend observed in zeolite Y. Other high alumina content materials also reveal this concave shaped trend.[45,46] Potassium exchanged VPI-9 exhibits a higher activation energy than K-X, 0.72 versus 0.55 eV, but rubidium and cesium exchanged VPI-9 show lower activation energies than the respective exchanged

zeolite X samples, 0.64 eV and 0.66 eV for rubidium exchanged VPI-9 and X, respectively, and 0.69 versus 0.71 eV for cesium exchanged VPI-9 and X, respectively. It is suggested that activation energies measured for the present rubidium and cesium containing zeolite X materials, which contain residual sodium, are lower than activation energies that would be measured for fully exchanged rubidium and cesium X samples, could full exchange be achieved.

5.4.5. Ionic Conductivity and Activation Energy in M^{2+}-VPI-9

Figure 5.5a also shows the experimentally measured conductivities for VPI-9 and zeolite X exchanged with divalent alkaline earth cations, Mg^{2+}, Ca^{2+}, and Sr^{2+}. Mg-VPI-9 becomes amorphous upon vacuum dehydration and the arrows in Figure 5.5a,b indicate data for this sample. Zeolite X exchanged with divalent cations has been reported to exhibit low conductivity[37] and similar results are observed here with conductivities below 10^{-10} S/cm at 400 °C for magnesium, calcium, and strontium containing samples. By comparison, calcium and strontium containing VPI-9 exhibit conductivities approaching 10^{-6} S/cm at 400 °C, an improvement of nearly four orders of magnitude. This is quite impressive considering the decreased number of anionic framework sites and the reduced overall framework charge density in VPI-9 (Si/Zn = 4, Si/- = 2 where "-" indicates a -1 framework charge) compared to zeolite X (Si/Al = 1.25, Si/- = 1.25). The two anionic framework sites created by each zinc and the arrangement thereof must play a fundamental role in facilitating divalent ion transport in the microporous zincosilicate VPI-9. It should be noted, however, that the conductivity measured

in divalent cation exchanged VPI-9 is one to two orders of magnitude lower than the conductivity measured for monovalent cation exchanged VPI-9.

The activation energies for Ca-VPI-9 and Sr-VPI-9 are 0.88 and 0.91 eV, respectively, and are also reduced compared to those calculated for Ca-X and Sr-X (1.19 and 1.64 eV, respectively). One potential explanation for greater conductivity and reduced activation energy in VPI-9 is that each framework zinc creates two anionic framework sites in close proximity to one another. Each framework zinc can, therefore, act as an individual hopping site for a divalent ion. Furthermore, because the Si/Zn is low and zinc is ordered in the VPI-9 structure, well-defined conduction paths may be present, although computational work in accordance with work by Franke on proton hopping in H-ZSM-5[47] would be helpful for obtaining a more detailed explanation. In zeolite X, however, the anionic framework sites are created by framework aluminum and are univalent. To minimize the overall free energy of the framework and charge balancing cations, two of these univalent sites must be in an appropriate arrangement to electrostatically charge balance a divalent ion, and many different spatial arrangements (from the geometry of the framework and distribution of aluminum among the T sites) are envisioned, each with a different potential energy landscape for ion hopping. Simplified 2-dimensional schematics illustrating this concept are shown in Figure 5.6a-c for the case of calcium ion charge balancing framework zinc (Figure 5.6a) and two hypothetical situations for calcium ion charge balancing two monovalent anionic aluminum sites (Figure 5.6b,c). The presence of different arrangements of univalent anionic sites, possibly far

removed from one another, could lead to a reduced number of mobile cations and a reduced number of accessible hopping sites (increasing the distance between available sites, decreasing the conductivity[47]), thereby decreasing the conductivity and increasing the hopping activation energy in zeolite X. The physical 3-dimensional situation is clearly more complicated as cations will reside in the most stable coordination sites, but sites arising from zinc are, undoubtedly, electrostatically different than those arising from aluminum.

Interestingly, while it may be expected that the electrostatic interaction between divalent cationic and anion charges would lead to significantly increased transport activation energy, this is not is what has been experimentally observed in VPI-9.

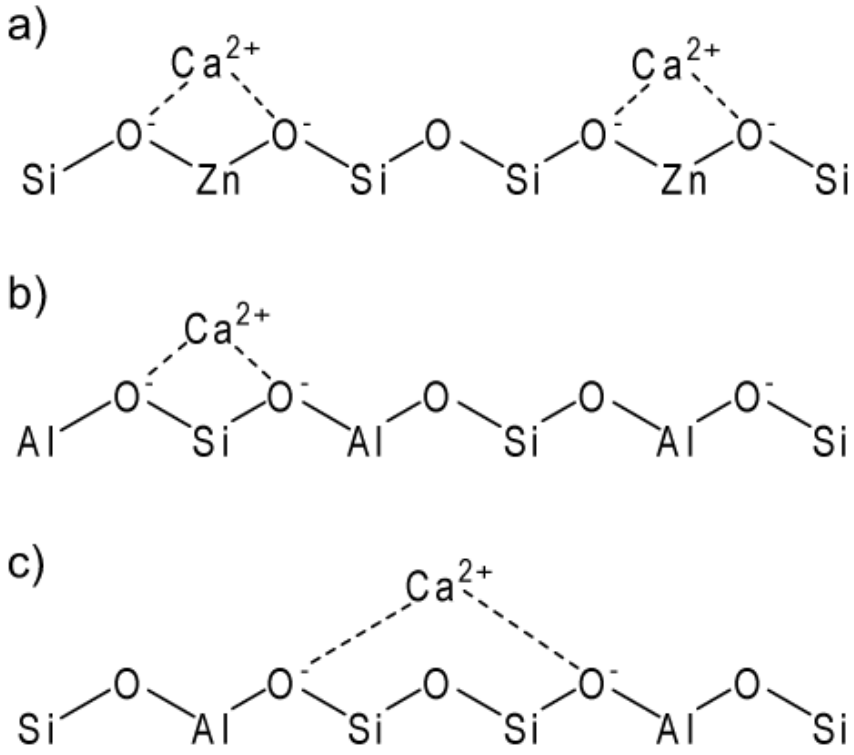

Figure 5.6. a) Framework zinc creates two anionic sites in close proximity to one another providing a more uniform site for divalent cations than can be obtained with zeolites. b) and c) show two hypothetical situations to charge balance a divalent cation with two individual framework sites. The two situations appear different from the perspective of the cation, and will have different associated energies.

5.4.6. Powder X-ray Diffraction and EDS of $M_2ZnSi_XO_{2(X+1)}$

In the interest of comparing the conductivity of alkali exchanged VPI-9, K-VPI-9, Rb-VPI-9, and Cs-VPI-9 microporous solids to the conductivity of dense materials with similar compositions (as a few dense, sodium containing analogs have been studied as sodium ion conductors[48-53]) dense zincosilicates were prepared. No phases with compositions of $Rb_2ZnSi_4O_{10}$ or $Cs_2ZnSi_4O_{10}$ (Si/Zn = 4, like VPI-9) could be found in the literature. However, the series of $M_2ZnSi_5O_{12}$ (where M = K, Rb, Cs) has been synthesized previously,[38,40] as has the series of potassium containing compounds $K_2ZnSi_xO_{2(x+1)}$ with x ranging from 2 to 5.[38,39,41,42] These materials were, therefore, prepared for comparison with VPI-9. The $M_2ZnSi_5O_{12}$ series was used to study effect of the alkali cation at constant zincosilicate composition, and the $K_2ZnSi_xO_{2(x+1)}$ series to investigate the effect of Si/Zn ratio ($M_2ZnSi_4O_{10}$ materials are not know for all three cations of interest, K, Rb, and Cs).

Powder X-ray diffraction patterns for the prepared dense materials are shown in Figure 5.7, and, with the exception of $K_2ZnSi_2O_6$, match known diffraction patterns. The peaks in the $K_2ZnSi_2O_6$ spectra were compared against known structures and the known phase of $K_2ZnSi_2O_6$ was the only minor impurity detected. The powder diffraction pattern reported here may represent a new phase of $K_2ZnSi_2O_6$, but further characterization is beyond the scope of this study. An unknown impurity in $K_2ZnSi_4O_{10}$ may also exist in small amounts. $K_2ZnSi_3O_8$ appears pure as do $K_2ZnSi_5O_{12}$, $Rb_2ZnSi_5O_{12}$, and $Cs_2ZnSi_5O_{12}$. The powder X-ray diffraction patterns for $K_2ZnSi_5O_{12}$, $Rb_2ZnSi_5O_{12}$, and $Cs_2ZnSi_5O_{12}$

appear similar to one another, with peaks shifting to smaller 2θ values with increasing size of the alkali cation, $Cs^+ > Rb^+ > K^+$.

EDS results from crystallized compounds are shown in Table 5.3, and, as previously mentioned, crystallized samples are slightly deficient in the alkali cations and show a surplus of oxygen. Volatilization of the alkali metal is not ruled out, but is not believed to be significant, as ion exchanged VPI-9 and zeolite X samples show a similar deficiency by EDS, and powder X-ray diffraction indicates the appropriate phases (with the exception of $K_2ZnSi_2O_6$ for which the phase is unknown).

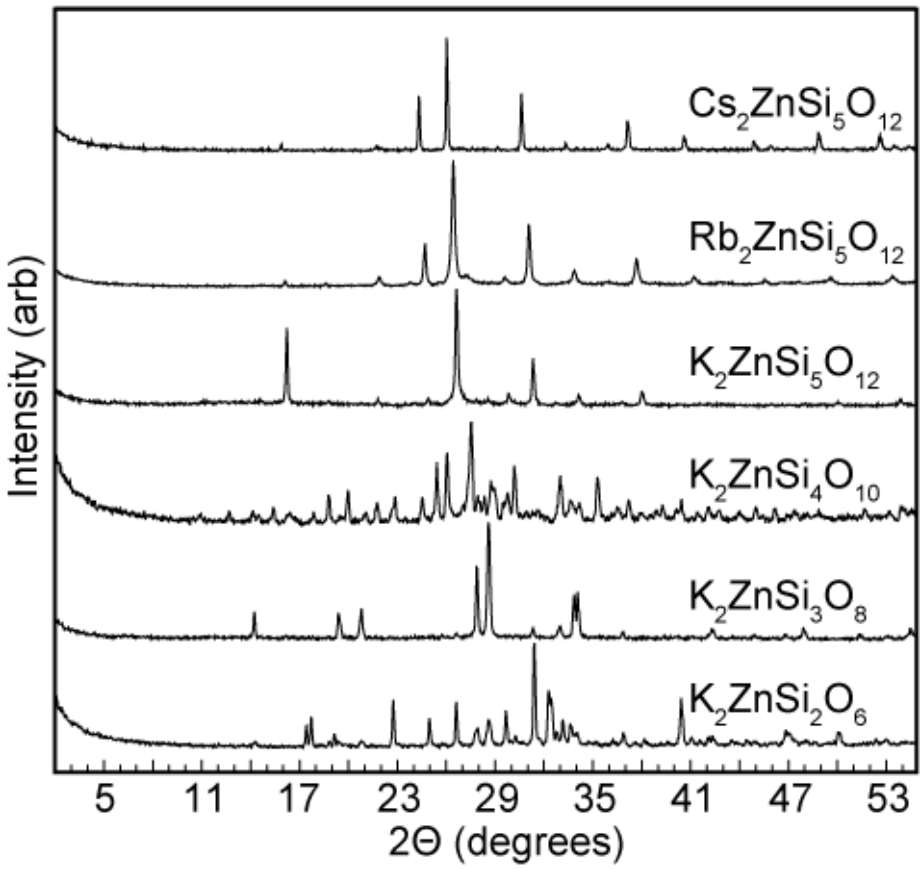

Figure 5.7. Powder X-ray diffraction spectra of crystallized dense zincosilicates.

Table 5.3. EDS Elemental analysis results for crystallized dense zincosilicates.

	M[a]	Si	Zn	O
$K_2ZnSi_2O_6$	1.6	2	1.1	7.4
$K_2ZnSi_3O_8$	1.9	3	1.1	9.2
$K_2ZnSi_4O_{10}$	1.8	4	1.2	12.6
$K_2ZnSi_5O_{12}$	1.6	5	1.1	14.8
$Rb_2ZnSi_5O_{12}$	1.7	5	1.1	14.8
$Cs_2ZnSi_5O_{12}$	1.7	5	1.0	14.6

a. M = K, Rb, Cs

5.4.7. Ionic Conductivity in $M_2ZnSi_XO_{2(x+1)}$ and Comparison to Microporous VPI-9

Conductivity values calculated from impedance spectra are presented in Figure 5.8a for the $K_2ZnSi_XO_{2(x+1)}$ (x = 2-5) series of solids and in Figure 5.8b for the $M_2ZnSi_5O_{12}$ (M = K, Rb, Cs) series of materials. All samples show activated behavior, and impedance spectra (not shown) have similar appearance to those previously shown with a high frequency semicircular arc and a low frequency tail. Within the $K_2ZnSi_XO_{2(x+1)}$ (x = 2-5) series, conductivity increases with decreasing Si/Zn; $K_2ZnSi_2O_6$ exhibiting the highest conductivity and $K_2ZnSi_5O_{12}$ the lowest conductivity. This behavior is not surprising as the distance between zinc tetrahedra, and hence anionic framework sites, decreases with increasing zinc content (decreasing Si/Zn), leading to shorter distances between equilibrium cation sites.

Within the $M_2ZnSi_5O_{12}$ (M = K, Rb, Cs) series, rubidium containing samples exhibit the highest conductivity at all temperatures, followed by the potassium containing sample, and finally the cesium containing sample. For comparison with microporous VPI-9 containing potassium, rubidium, and cesium cations, conductivity data and activation energy from dense and microporous samples are plotted together in Figure 5.9. VPI-9 samples, indicated by the filled markers, exhibit over four orders of magnitude greater conductivity than their dense counterparts. Using the conductivity of $K_2ZnSi_4O_{10}$ at 400 °C compared to

the conductivity of $K_2ZnSi_5O_{12}$ at 400 °C as an estimate for what the conductivity of hypothetical $Rb_2ZnSi_4O_{10}$ and $Cs_2ZnSi_4O_{10}$ would be if they were to exist, a factor of four improvement could be suggested. These hypothetical conductivities, and indeed the conductivity of dense $K_2ZnSi_4O_{10}$ compared to K-VPI-9, are dramatically lower than the conductivities observed in their microporous counterparts.

Figure 5.9b shows that the trend in conductivity with ionic radius is the same for both VPI-9 and $M_2ZnSi_5O_{12}$; Rb > K > Cs. Activation energies of corresponding microporous and dense samples also show the same trend, that is decreasing from potassium to rubidium and then increasing from rubidium to cesium. It is interesting to note that the activation energy for $M_2ZnSi_5O_{12}$ is nearly twice that of the respective microporous sample.

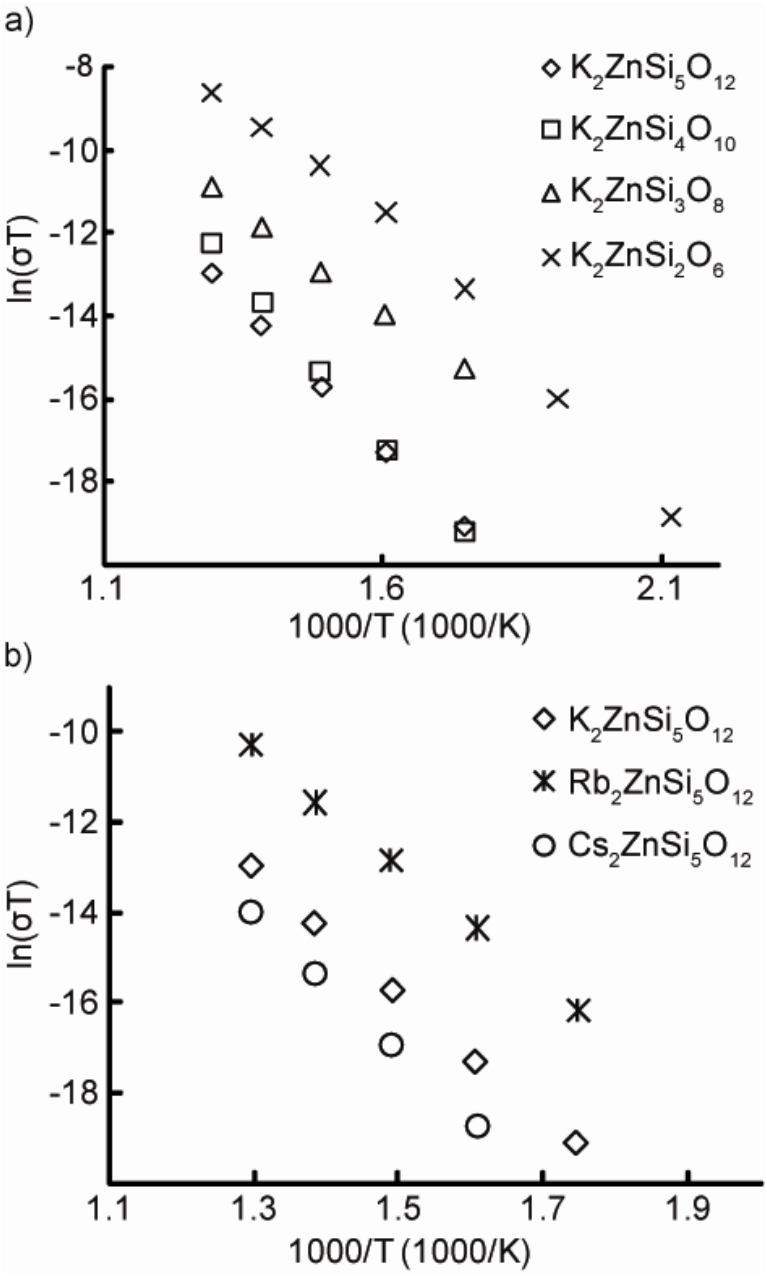

Figure 5.8. Ionic conductivity presented as the natural log of the product of conductivity and temperature versus the inverse temperature for a) $K_2ZnSi_xO_{2(1+x)}$ dense zincosilicates, and b) $K_2ZnSi_5O_{12}$, $Rb_2ZnSi_5O_{12}$, and $Cs_2ZnSi_5O_{12}$ dense zincosilicates.

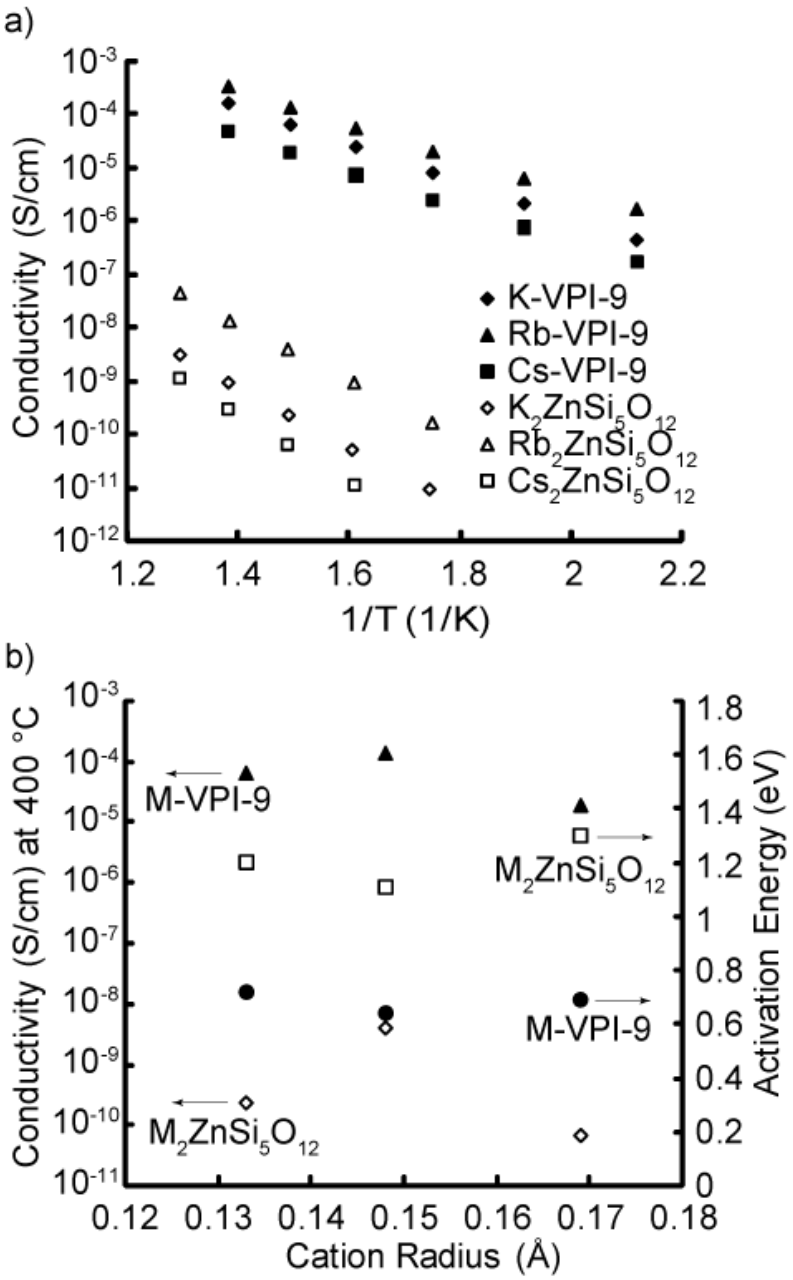

Figure 5.9. Comparison of a) ionic conductivity as a function of inverse temperature of K-, Rb-, and Cs-VPI-9 and K, Rb, and Cs containing dense zincosilicates, and b) ionic conductivity at 400 °C and activation energy as functions of cation radius for the same samples.

5.5. Summary

The microporous zincosilicate VPI-9 has been prepared and ion exchanged to contain the alkali cations Li^+, Na^+, K^+, Rb^+, Cs^+, and alkaline earth cations Mg^{2+}, Ca^{2+}, Sr^{2+}, and ionic conductivities have been measured with impedance spectroscopy. When compared to correspondingly exchanged zeolite X samples, K-VPI-9 exhibits lower conductivity and higher activation energy, while Rb-, and Cs-VPI-9 have higher conductivity and lower activation energy than rubidium and cesium exchanged zeolite X. Where VPI-9 is particularly interesting, however, is in its ability to transport divalent cations. Indeed, Ca- and Sr-VPI-9 show conductivity nearly four orders of magnitude greater than correspondingly exchanged zeolite X samples. It is suggested, therefore, that this unique property could arise from the two anionic sites created by each tetrahedral zinc framework site, which are ordered in the structure of VPI-9. Furthermore, M-VPI-9 (M = K, Rb, Cs) possess significantly greater conductivity and lower activation energy than dense, crystalline samples containing tetrahedrally coordinated zinc and silicon of similar silicon, zinc, and alkali metal composition.

5.6. References

(1) Davis, M. E. *Nature* **2002**, *417*, 813.

(2) Wang, Z. B.; Wang, H. T.; Mitra, A.; Huang, L. M.; Yan, Y. S. *Adv. Mater.* **2001**, *13*, 746.

(3) McKeen, J. C.; Yan, Y. S.; Davis, M. E. *Chem. Mater.* **2008**, *20*, 3791.

(4) McKeen, J. C.; Yan, Y. S.; Davis, M. E. *Chem. Mater.* **2008**, *20*, 5122.

(5) Holmberg, B. A.; Wang, Z.; Yan, Y. *J. Membr. Sci.* **2008**, *320*, 86.

(6) Holmberg, B. A.; Hwang, S.-J.; Davis, M. E.; Yan, Y. *Microporous Mesoporous Mater.* **2005**, *80*, 347.

(7) Cheng, X. *Electrochem. Solid-State Lett.* **2001**, *4*, B23.

(8) Chen, G. *Langmuir* **2009**, *25*, 1620.

(9) Rimoli, M. *J. Biomed. Mater. Res. A* **2008**, *87a*, 156.

(10) Annen, M. J.; Davis, M. E.; Higgins, J. B.; Schlenker, J. L. *J. Chem. Soc., Chem. Commun.* **1991**, 1175.

(11) Yoshikawa, M.; Zones, S. I.; Davis, M. E. *Microporous Materials* **1997**, *11*, 127.

(12) Yoshikawa, M.; Zones, S. I.; Davis, M. E. *Microporous Materials* **1997**, *11*, 137.

(13) Camblor, M. A.; Yoshikawa, M.; Zones, S. I.; Davis, M. E. *Chemical Industries* **1997**, *69*, 243.

(14) Camblor, M. A.; Davis, M. E. *J. Phys. Chem.* **1994**, *98*, 13151.

(15) Annen, M. J.; Davis, M. E. *Microporous materials* **1993**, *1*, 57.

(16) McCusker, L. B.; Grosse-Kunstleve, R. W.; Baerlocher, C.; Yoshikawa, M.; Davis, M. E. *Microporous Materials* **1996**, *6*, 295.

(17) Takewaki, T.; Beck, L. W.; Davis, M. E. *J. Phys. Chem. B* **1999**, *103*, 2674.

(18) Takewaki, T.; Beck, L. W.; Davis, M. E. *Top. Catal.* **1999**, *9*, 35.

(19) Serrano, D. P.; Grieken, R. v.; Davis, M. E.; Melero, J. A.; Garcia, A.; Morales, G. *Chemistry: A European Journal* **2002**, *22*, 5153.

(20) Rohrig, C.; Gies, H. *Angew. Chem., Int. Ed. Engl.* **1995**, *34*, 63.

(21) Wei, T.-C.; Hillhouse, H. W. *J. Phys. Chem. B* **2006**, *110*, 13728.

(22) Schoonheydt, R. A.; Wilde, W. d. *J. Chem. Soc., Faraday Trans. I* **1974**, *70*, 2132.

(23) Schoonheydt, R. A.; Velghe, F. *J. Chem. Soc., Faraday Trans. I* **1976**, *72*, 172.

(24) Schoonheydt, R. A.; Uytterhoeven, J. B. *Advances in Chemistry Series* **1971**, *101*, 456.

(25) Schoonheydt, R. A. *Proc. Int. Conf. Zeolites* **1980**, *5*, 242.

(26) Schoonheydt, R. A.; Uytterhoeven, J. B. *Clay Minerals* **1969**, *8*, 71.

(27) Mortier, W. J.; Schoonheydt, R. A. *Prog. Solid State Chem.* **1985**, *16*, 1.

(28) Jansen, F. J.; Schoonheydt, R. A. *J. Chem. Soc., Faraday Trans. I* **1973**, *69*, 1338.

(29) Kalogeras, J. M.; Vassilikou-Dova, A. *Cryst. Res. Technol.* **1996**, *31*, 693.

(30) Kalogeras, I. M.; Vassilikou-Dova, A. *Defect and Diffusion Forum* **1998**, *164*, 1.

(31) Simon, U.; Franke, M. E. *Microporous Mesoporous Mater.* **2000**, *41*, 1.

(32) Simon, U.; Flesch, U. *J. Porous Mater.* **1999**, *6*, 33.

(33) Nischwitz, P.; Amels, P.; Fetting, F. *Solid State Ionics* **1994**, *73*, 105.

(34) Tabourier, P.; Carru, J.-C.; Wacrenier, J.-M. *J. Chem. Soc., Faraday Trans. I* **1983**, *79*, 779.

(35) Tabourier, P.; Carru, J. C.; Wacrenier, J. M. *Zeolites* **1983**, *3*, 50.

(36) Stamires, D. N. *J. Chem. Phys.* **1962**, *36*, 3174.

(37) Freeman, D. C.; Stamires, D. N. *J. Chem. Phys.* **1961**, *35*, 799.

(38) Kohn, S. C.; Henderson, C. M. B.; Dupree, R. *Phys. Chem. Min* **1994**, *21*, 176.

(39) Dollase, W. A.; II, C. R. R. *Zeitschrift Fur Kristallographie* **1993**, *206*, 25.

(40) Bell, A. M. T.; Henderson, C. M. B. *Acta Crystallographica. Section C, Crystal structure communications* **1994**, *c50*, 984.

(41) Kohara, S.; Kawahara, A. *Acta Crystallogr., Sect. C: Cryst. Struct. Commun.* **1990**, 1373.

(42) Hogrefe, A. R.; Czank, M. *Acta Crystallogr., Sect. C: Cryst. Struct. Commun.* **1995**, *9*, C51.

(43) Breck, D. W. *Zeolite Molecular Sieves*; Robert E. Krieger Publishing Company: Malabar, Florida, 1984.

(44) Annen, M., Virginia Polytechnic University.

(45) Kelemen, G.; Schon, G. *J. Mater. Sci.* **1992**, *27*, 6036.

(46) Beattie, I. R. *Transactions of the Faraday Society* **1954**, *50*, 581.

(47) Franke, M. E.; Sierka, M.; Simon, U.; Sauer, J. *Physical Chemistry Chemical Physics* **2002**, *4*, 5207.

(48) Grins, J. *J. Mater. Sci.* **1986**, *21*, 887.

(49) Grins, J. *Solid State Ionics* **1982**, *7*, 157.

(50) Grins, H.; Frostang, S.; Nygren, M. *Mater. Res. Soc. Symp. Proc.* **1991**, *210*, 657.

(51) Frostang, S.; Grins, J.; Nygren, M. *Mater. Res. Soc. Symp. Proc.* **1989**, *135*, 239.

(52) Frostang, S.; Grins, J.; Nygren, M. *Chemica Scripta* **1988**, *28*, 107.

(53) Delmas, C.; Maazaz, A.; Hagenmuller, P. *Solid State Ionics* **1983**, *9-10*, 83.

6. Impedance Spectroscopic Measurement of Other Zeotypes

6.1. Isostructural Zinc and Aluminum Containing Materials

One of the first directions taken in the study of ion conductivity in zinc containing microporous materials was to investigate how zinc containing materials compare to aluminum containing materials with the same structure, same framework substitution density (zinc versus aluminum), and same exchanged cation. While no aluminosilicate analog for VPI-9 is known, materials with the BEA, ANA, and SOD framework topologies have been synthesized containing either framework zinc or framework aluminum. These materials were prepared and characterized by impedance spectroscopy. CIT-6 and aluminum containing CIT-6 (heretofore referred to as Zn-CIT-6 and Al-CIT-6 for clarity) were prepared from clear gels according to published procedures.[1,2] Zn-ANA was synthesized from gels with the composition 1.18 CsOH:0.08 TEAOH:0.04 ZnO:1 SiO_2:22 H_2O in accordance with Annen's procedure[3] while Al-ANA was prepared from gels with composition 1.4 CsOH:2.8 NaOH:1 $NaAlO_2$ (sodium aluminate, Aldrich):10 SiO_2:140 H_2O, crystallized over three days at 200 °C. Zn-SOD was prepared according to published procedures[4] from a gel with composition 0.78 TMAOH:0 TMACl:0.18 NaOH:0 NaCl:0.025 $Zn(Ac)_2$*2H_2O (zinc acetate):1 SiO_2 (Ludox HS-40):21 H_2O and Al-SOD was crystallized from gels with composition 0.78 TMAOH:0 TMACl:0.18 NaOH:0 NaCl:0.025 $NaAlO_2$ (sodium aluminate, EM Chemicals):1 SiO_2 (Ludox HS-40):21 H_2O kept, statically, at 175 °C for 5 days.

All materials were calcined in flowing air at temperatures of at least 550 °C for at least 6 hours. Zinc and aluminum containing materials with the SOD framework topology became black upon calcination indicating the formation of carbonaceous species and incomplete removal of carbon from the pore structure, even when calcined at temperatures above 550 °C. Impedance spectroscopy was not used to characterized sodalite (SOD) materials as the presence of carbon should greatly affect the impedance of the sample (carbon is electronically conductive). Template free Zn-CIT-6, Al-CIT-6, Zn-ANA, and Al-ANA, however, were successfully prepared. CIT-6 materials were contacted with 1 M NaCl solutions to ensure sodium exchange, and ANA type materials were contacted with 1 M $CsNO_3$ solutions to prepare cesium exchanged materials. Sodium exchange in ANA type materials was attempted, but found to be incomplete. EDS results are shown in Table 6.1. Somewhat fortuitously, Zn-CIT-6 and Al-CIT-6 have similar framework substitution concentrations (Zn or Al), but consequently, the charge balancing cation density in Zn-CIT-6 is twice that of Al-CIT-6. Al-ANA and Zn-ANA have different framework substitution concentrations, and hence, different concentrations of charge balancing cesium cations. Nevertheless, IS was used to characterize the ability of these four materials to conduct cations. As shown in Table 6.1, Zn-CIT-6 samples appear deficient in sodium and Al-ANA appears slightly deficient in Cs (but no Na was detected by EDS).

Table 6.1. EDS and E_A results for CIT-6 and ANA type materials.

	Cation	E_A (eV)	Si/M* (EDS)	M*/Cs, Na (EDS)
Zn-CIT-6	Na	1.01	16	1.1
Al-CIT-6	Na	0.78	20	1
Zn-ANA	Cs	0.94	4	0.5
Al-ANA	Cs	0.68	2.9	0.82

*M = Zn, Al

Powdered materials were pelletized and prepared for IS measurements in accordance with previous discussion. Conductivity results are presented in Figure 6.1 and activation energies in Table 6.1. While no direct comparison can be made between CIT-6 and ANA samples because they do not contain the same charge balancing cation, a common trend in conductivity is shared between both families of materials; aluminum containing materials possess higher conductivity and lower activation energy than corresponding zinc containing samples. While the higher activation energy for conduction observed in zinc containing samples could be rationalized as greater cation-cation, particularly when comparing Zn-CIT-6 to Al-CIT-6 where the sodium cation density is nearly double in Zn-CIT-6 (or, theoretically, should be, as EDS results indicate the correct Si/Zn ration but not the correct Na/Zn ratio), it is unknown why such a drastic decrease in conductivity is observed in zinc containing materials. There must either be fewer sites available for hopping, or the sodium cation must have reduced mobility (velocity per unit electric field) in the pores of the zinc containing framework. Unfortunately, no conclusion has been reached.

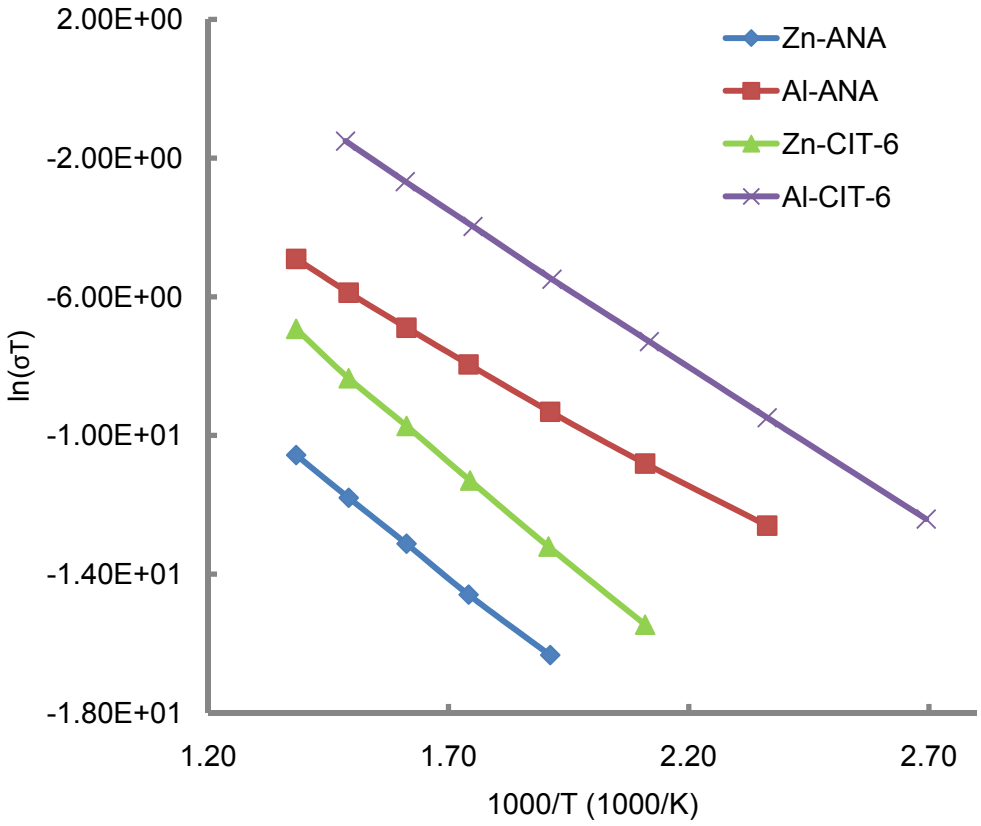

Figure 6.1. Conductivity of Zn and Al containing ANA and CIT-6.

6.3. Sodium Exchanged FAU and EMT from Crown Ether Synthesis

As has been previously discussed, relaxation and ion conductivity in zeolite X and Y (faujasite type structures) have been topics of interest for the past four decades. EMT is a closely related 'hexagonal' structure formed from the stacking of sodalite layers in an ABAB fashion (leading to larger cages than in FAU) compared to the 'cubic' FAU formed from the stacking of sodalite layers in an ABCABC fashion. Both materials have three-dimensional pore structures, and, while intergrowths of the two materials often crystallize, Burkett and Davis produced pure phases having the same Si/Al from crown-ether containing gels.[5] Materials were used as received, but calcined to remove the occluded structure directing crown ether. Calcination was performed in flowing oxygen to ensure the complete removal of carbonaceous species. The Si/Al was calculated from solid state magic angle spinning (MAS) NMR and found to be 3.9 in both FAU and EMT materials. IS was performed on pelletized samples to measure sodium ion conductivity and also on non-pelletized powders (see Section 2.6) to elucidate internal relaxations. Ionic conductivity for sodium forms of FAU and EMT is shown in Figure 6.2. The conductivity of the materials is nearly identical and only small variations are observed at lower temperatures. The activation energy of transport in EMT is 0.78 eV and in FAU is 0.81 eV, nearly identical.

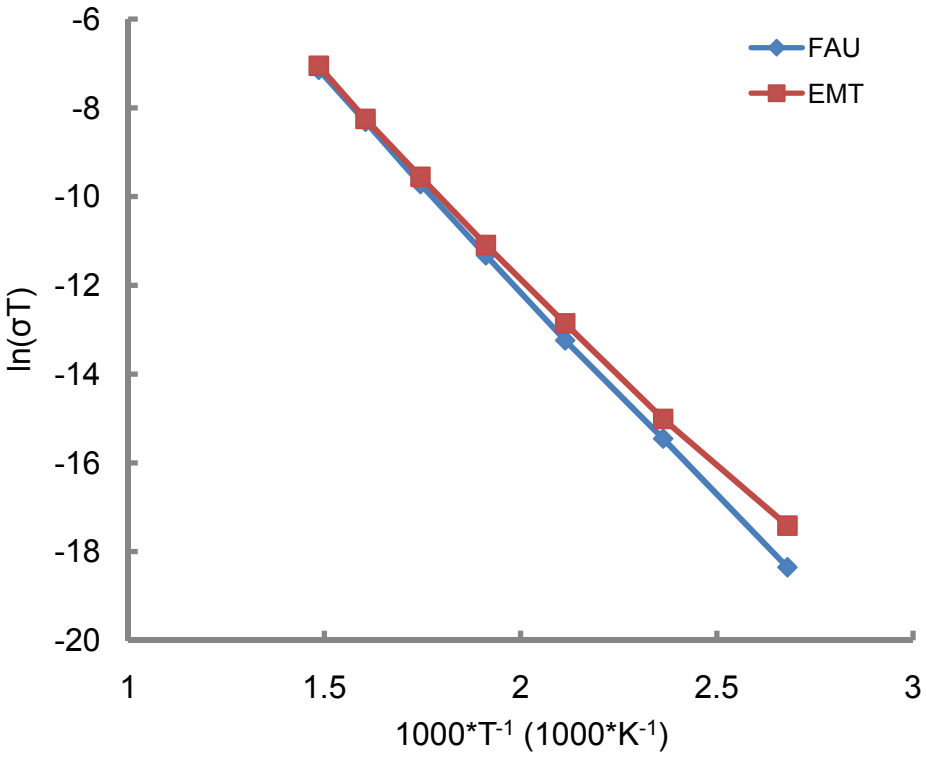

Figure 6.2. Ionic conductivity of FAU and EMT from Pelletized Powders.

When dielectric measurements were performed on non-pelletized powder samples, the two commonly observed peaks in the M” spectra were observed, the lower frequency peak arising from an overall sample conductivity, and a high frequency peak generally attributed to the short range motion of a sodium ion (in FAU, within the α cage between sites II → III → III → II as has been previously discussed). Peak-maximum frequencies were recorded for the high and low frequency M” peaks as functions of temperature and are shown in Figure 6.3. The low frequency peak is indistinguishable between the FAU and EMT samples, in accordance with the nearly identical conductivity of the pelletized samples and identical powder measurement technique (as contributions to the low frequency arise from both materials properties and preparation techniques such as pressure, etc), but the peak frequency for a given temperature is higher in EMT than in FAU suggesting more facile movement of a sodium ions in the large cages of EMT when compared to FAU. The activation energy for the high frequency peak in EMT is lower than for the high frequency peak in FAU. While no explanation is offered as to why $E_{A_HF}^{EMT}$is lower than $E_{A\_HF}^{FAU}$ the observation of a difference is not surprising due to the different cage structures.

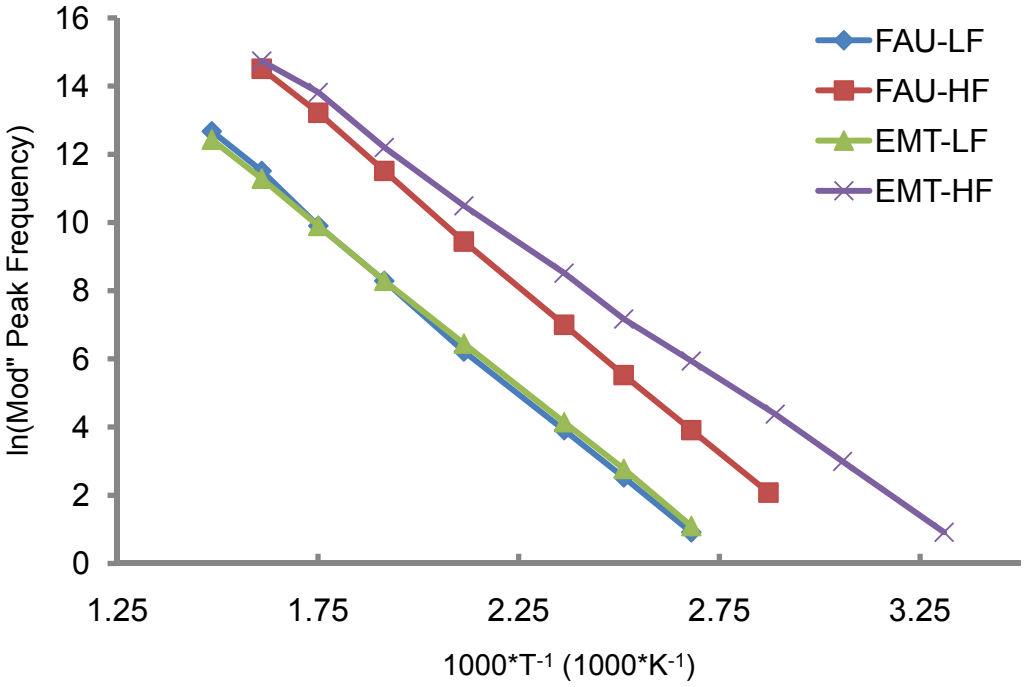

Figure 6.3. Peak Frequency of high and low frequency relaxations observed in the M" spectra as functions of temperature for sodium containing FAU and EMT type materials.

6.4. Gallium and Containing FAU

In attempting to address how various framework substitutions (Zn, Ga, Al) affect ion conductivity, gallium and aluminum containing faujasite with the same substitutional heteroatom density were prepared. Synthesis were according to a published procedure.[6] (Gel composition 1 Ga_2O_3:9 NaOH:10 SiO_2 (Dupont HS-40):200 H_2O). Separation and integration of peaks in solid MAS NMR, shown in Figure 6.4, gives Si/Al = 2 and Si/Ga = 2 in respective materials. Powdered samples were pelletized according to previously discussed procedures and IS was used to measure the sodium ion conductivity. Results are shown in Figure 6.5. Interestingly, gallium and aluminum containing materials with the same framework substitution density have nearly identical sodium ion conductivities and activation energies.

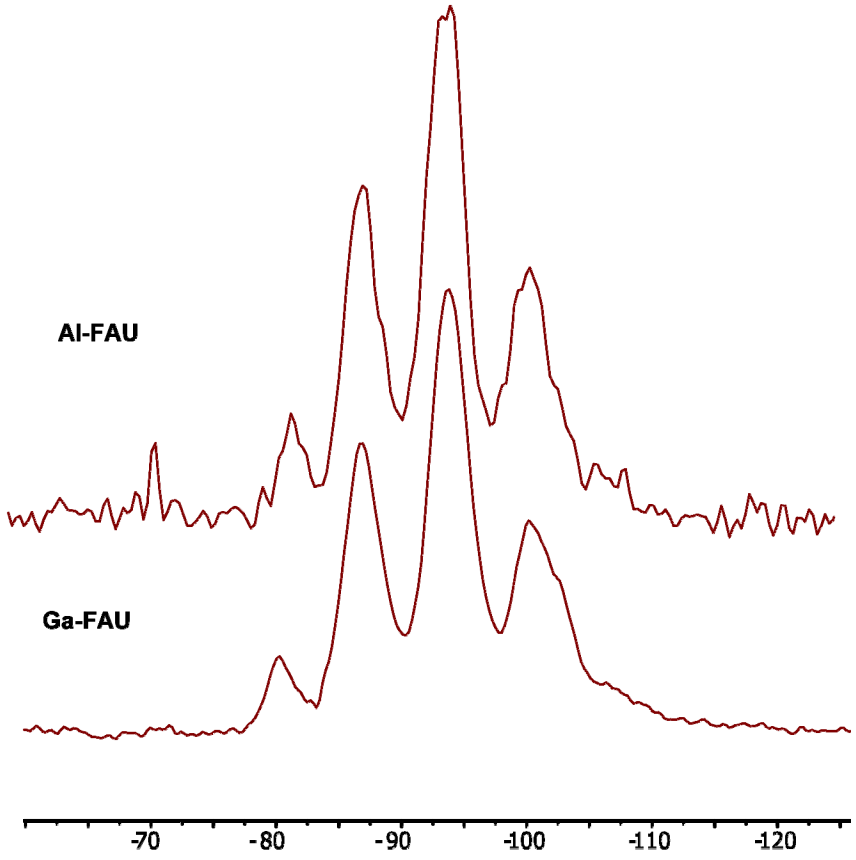

Figure 6.4. Solid MAS NMR of aluminum containing FAU and gallium containing FAU.

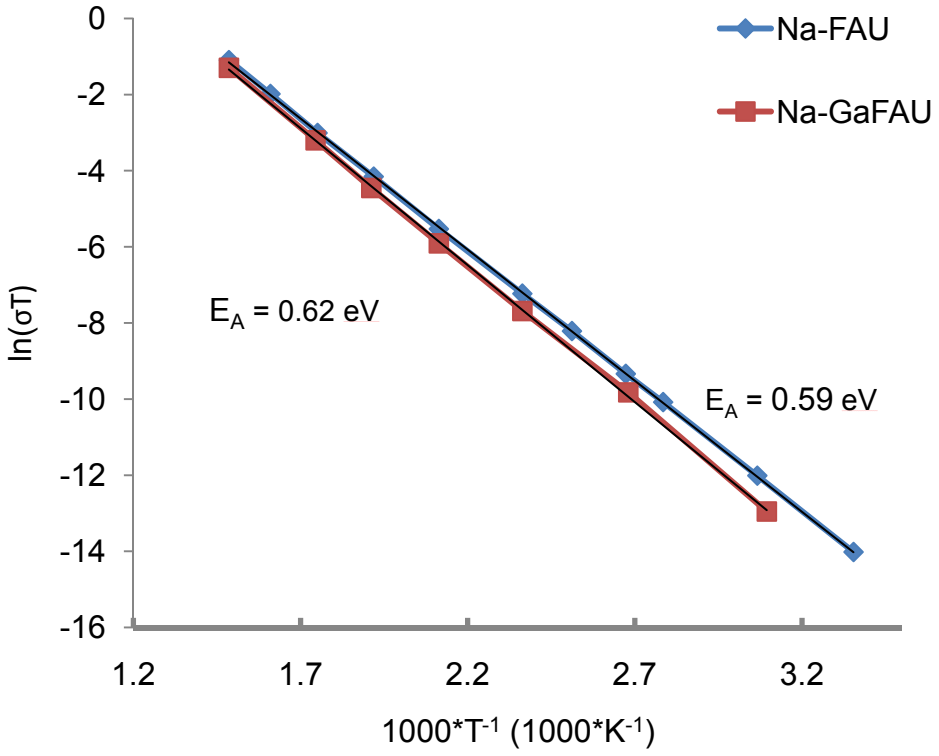

Figure 6.5. Conductivity of Na-AlFAU and Na-GaFAU.

6.5. Pure Silica Zeolite Beta from Fluoride Synthesis

Finally, as an early check to confirm that observed results on ion containing samples truly arose from the presence of the ion, pure silica zeolite beta was pelletized and investigated with impedance spectroscopy. The synthesis of this material was described in chapter 3. Dielectric constant as a function of frequency and temperature is shown in Figure 6.6. The imaginary part of the dielectric constant, ε", associated with dielectric loss and conductivity is less than 0.1 over wide frequency and temperature spans indicating almost purely capacitive behavior, as is expected from a material having no mobile charge carriers. Furthermore, the real part of the dielectric constant, ε', is 2.7 in good agreement with the value of 2.3 reported by Li on randomly oriented pure silica BEA films.[7] Only at temperatures of 400 °C do spectra begin to indicate loss, possibly arising from residual, tightly bound fluorine.

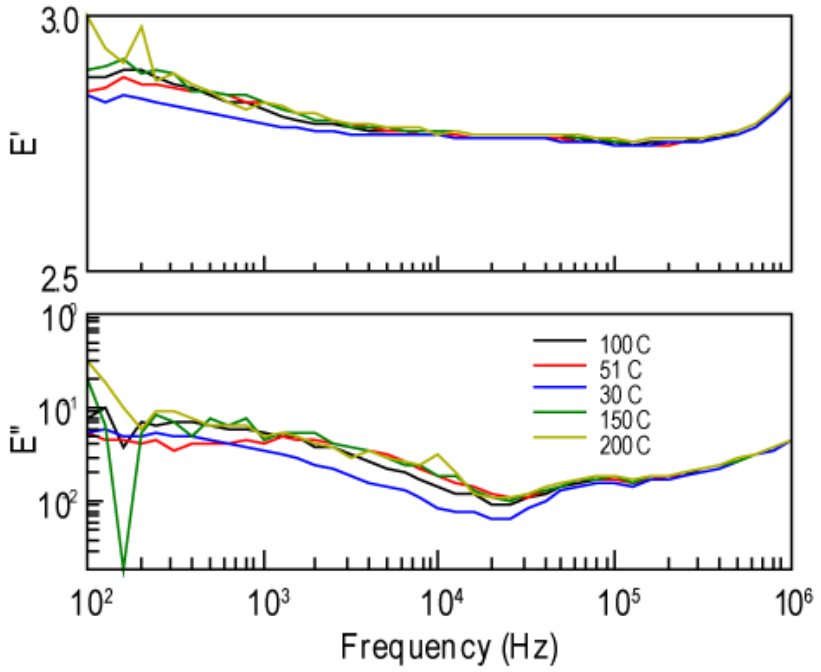

Figure 6.6 Real and imaginary parts of the dielectric constant as functions of frequency for pure silica zeolite beta over the temperature range 30-400 °C.

6.6. References

(1) Takewaki, T.; Beck, L. W.; Davis, M. E. *Top. Catal.* **1999**, *9*, 35.

(2) Takewaki, T.; Beck, L. W.; Davis, M. E. *J. Phys. Chem. B* **1999**, *103*, 2674.

(3) Annen, M., Virginia Polytechnic University.

(4) Camblor, M. A.; Lobo, R. F.; Koller, H.; Davis, M. E. *Chem. Mater.* **1994**, *6*, 2193.

(5) Burkett, S. L.; Davis, M. E. *Microporous materials* **1993**, *1*, 265.

(6) Occelli, M. L.; Schwering, G.; Fild, C.; Eckert, H.; Auroux, A.; Lyer, P. S. *Microporous Mesoporous Mater.* **2000**, *34*, 15.

(7) Li, Z. J.; Johnson, M. C.; Sun, M. W.; Ryan, E. T.; Earl, D. J.; Maichen, W.; Martin, J. I.; Li, S.; Lew, C. M.; Wang, J.; Deem, M. W.; Davis, M. E.; Yan, Y. S. *Angew. Chem., Int. Ed. Engl.* **2006**, *45*, 6329.

7. Conclusions and Suggestions for Future Works

7.1. Overall Conclusions

7.1.1. Protonic Conductivity

Proton conductivity in micro- and mesoporous materials arises from at least two types of acid sites. Bronsted acid sites arising from the substitution of tetrahedral aluminum for silicon in the framework can impart proton conductivity to the solid materials, particularly in the presence of a basic vehicle such as ammonia that abstracts the proton from the anionic framework site. Bronsted acid sites are also created by the attachment of organic acids onto the microporous or mesoporous pore walls. In this work, it has been shown that to achieve maximum conductivity, strong acids are necessary, such as sulfonic acids, and that pore size has minimal effect on proton conductivity when solids are prepared with the same acid loadings. The presence of a strong acid, however, while necessary, is not sufficient for achieving high proton conductivity, and surface silanols play a critical role by imparting hydrophilicity to the porous solids, leading to a percolated, hydrogen bonded water network that can support fast proton transport by the Grotthuss mechanism.

One initial goal of this work was to study potential cooperativety of these two types of Bronsted acids, as initial work by Holmberg[1] suggested this as a reason for observing the highest reported conductivity in solids that were crystallized from gels containing the greatest aluminum content. In this work, samples containing both types of Bronsted acids have not been successfully

synthesized. Extraction of the structure directing agent (TEA) by treatment with strong acid (sulfuric acid) and subsequent sulfonation of the phenethyl group by sulfuric acid or oleum extract framework aluminum leaving a pure silica framework. Sulfonic acid functionalized nanocrystalline zeolite beta samples produced throughout this investigation exhibit proton conductivity ~$5x10^{-3}$ S/cm, when functionalized to the same organic loading level, regardless of aluminum content in the synthesis gel, suggesting the variation in proton conductivity originally observed by Holmberg arose for some other reason.

7.1.2. Ionic Conductivity

Perhaps the most important conclusion to be drawn from the investigation of ionic conductivity of the zinc containing microporous zincosilicate VPI-9 is that the presence of tetrahedrally coordinated zinc and creation of two anionic framework sites greatly enhances the ionic conductivity of divalent cations when compared to aluminosilicate zeolite X, which shows low divalent ionic conductivity. The activation energy for divalent ion conductivity in VPI-9 is also significantly less than the activation energy for divalent ion conductivity in zeolite X. Clearly, the inclusion of zinc imparts unique properties to these materials that the incorporation of aluminum is incapable of creating.

Further, the conductivity of alkali cation exchanged microporous VPI-9 is greater than dense materials with similar compositions and cations, suggesting a useful direction for improving ionic conductivity in currently utilized materials.

7.2. Suggestions for Future Works

7.2.1. Protonic Conductivity

To truly assess the usefulness of micro- and mesoporous materials in fuel cells, mechanically stable membranes are necessary. While a number of groups have reported on the incorporation of small amounts of these materials into polymeric membranes, it is of interest to form a membrane of composed almost entirely of sulfonic acid functionalized nanocrystalline zeolite beta with high silanol content (as they possess the highest conductivity of the materials studied herein) with only a small amount of binder. Initial work in this direction has been undertaken by dispersing zeolite beta crystallites in a solution of ~10 wt% polyvinylidene fluoride (PVDF, Kynar) in N-methylpyrrolidone (NMP) such that ~90 wt% of the solids come from acid functionalized beta, and using a spray coating technique to form membranes ~100 μm thick. Such a membrane is shown in Figure 7.1. Ideally, these membranes could be formed on electrode assemblies for use in operating fuel cells, but much optimization is needed, and synthesis of large quantities of acid functionalized nanocrystalline zeolite beta is a major bottleneck.

Figure 7.1. Membrane formed by spray coating of zeolite beta onto aluminum foil. ~ 90 wt% solids are from zeolite and ~10 wt% solids are PVDF.

7.2.2. Ionic Conductivity

In continuation of this work, it is of interest to investigate the ion conducting properties of other zincosilicates such as VPI-7.[2] Unfortunately, VPI-7 is even more susceptible to framework collapse upon dehydration, and this is a significant barrier to characterization. VPI-8, however, may prove interesting, as the microporous solid can be synthesized over a range of zinc content.[3-6] Generally, however, VPI-8 is considered a high silica material and may possess low conductivity because of this. It may also be of interest to perform calculations toward understanding the results observed from VPI-9, as has been done in a number of aluminosilicate systems.

Comparison of the ion conducting properties of zinc, aluminum, gallium, boron, etc. containing material with the same framework topology and same cation or framework substitution density is of interest. Synthesis of these materials is a challenging problem itself, but could help separate mechanisms contributing to the cation conductivity.

Many studies on the dielectric properties of microporous materials can be envisioned. Further study of the EMT/FAU system and study of sodium and proton exchanged mordenite to better understand catalytic properties are two examples. But, it is suggested that these studies incorporate data from sources other than impedance spectroscopy, such as solid NMR, high resolution diffraction, time domain spectroscopy, etc., to fully understand cation positions and local motions. Assigning physical movements of cations to features in

dielectric spectroscopic data is not straightforward, but is a necessary ‘next step’ toward understanding cation motion in microporous materials.

7.3. References

(1) Holmberg, B. A.; Hwang, S.-J.; Davis, M. E.; Yan, Y. *Microporous Mesoporous Mater.* **2005**, *80*, 347.

(2) Annen, M. J.; Davis, M. E.; Higgins, J. B.; Schlenker, J. L. *J. Chem. Soc., Chem. Commun.* **1991**, 1175.

(3) Camblor, M. A.; Yoshikawa, M.; Zones, S. I.; Davis, M. E. *Chemical Industries* **1997**, *69*, 243.

(4) Freyhardt, C. C.; Lobo, R. F.; Khodabandeh, S.; Lewis, John E.; Tsapatsis, M.; Yoshikawa, M.; Camblor, M. A.; Pan, M.; Helmkamp, M. M.; Zones, S. I.; Davis, M. E. *J. Am. Chem. Soc.* **1996**, *118*, 7299.

(5) Yoshikawa, M.; Zones, S. I.; Davis, M. E. *Microporous Materials* **1997**, *11*, 137.

(6) Yoshikawa, M.; Zones, S. I.; Davis, M. E. *Microporous Materials* **1997**, *11*, 127.